

A STUDY OF BIS(AMIDO)PYRIDINE
COORDINATION CHEMISTRY TO RUTHENIUM
AND COBALT METALS

Faidh Hana

A thesis submitted to the faculty of graduate studies in partial
fulfillment of the requirements for the degree of Masters of Science.

*Graduate program in Chemistry
York University
Toronto, Ontario
December 2017*

© Faidh Hana, 2018

Abstract

This thesis presents the work performed at the Lavoie group to study and expand the coordination chemistry of a dianionic pincer ligand to ruthenium and cobalt. The coordination chemistry of the dianionic pincer ligand, bis(amido)pyridine ($[\text{NNN}]^{2-}$), is limited to early transition and f-block metals. Chapter 1 presents the properties, the coordination chemistry and the synthesis of the bis(amido)pyridine ligand. Chapter 2 focuses on experimental procedures to synthesize bis(amido)pyridine-supported ruthenium complexes. Three different methods to prepare the Ru complexes were explored. Computational methods were utilized to predict the stability of different conformers of ruthenium methyldene complexes, $[\text{NNN}]\text{Ru}(\text{CH}_2)$, and to map the energy diagram of the olefin metathesis intermediates. The results showed that the methyldene group in $[\text{NNN}]\text{Ru}(\text{CH}_2)$ is more energetically favorable in the cis compared to the trans conformation (cis with respect to the $[\text{NNN}]$ pyridine). Chapter 3 focuses on the coordination of the ligand to cobalt(III). A series of low-valent Co(III) square planar complexes supported by $[\text{NNN}]^{2-}$ is reported. Complexes $[[\text{NNN}]\text{Co}(\text{py})]\text{BF}_4$ (**2**), $[\text{NNN}]\text{Co}(\text{OPh})$ (**3a**) and $[\text{NNN}]\text{Co}(\text{OH})$ (**4**) were synthesized and structurally characterized. Complex **4** is the first isolated and structurally characterized square planar Co hydroxide complex. The magnetic properties of the Co(III) complexes were measured using the Evans method and found to be dependent on the charge of the complex and on the coordination environment of the metal. The diamagnetic cationic complex $[[\text{NNN}]\text{Co}(\text{py})]\text{BF}_4$ (**2**) was converted to neutral paramagnetic complexes $[\text{NNN}]\text{Co}(\text{OR})$ (R = Ph **3a**, H **4**) by simple substitution of the ancillary pyridine ligand in **2**. Analysis of the solid-state structures showed

double bond character between the metal and the anilido nitrogen, evident by short cobalt-nitrogen bond lengths, which is further supported by DFT computations. Electrochemical properties of the Co(III) complexes showed redox processes on both cobalt and ligands. DFT computations were also used to shed light onto the redox activity of the Co(III) complexes through molecular orbital composition analysis.

Acknowledgments

I would like to thank Professor Gino G. Lavoie for guidance and patience throughout my MSc. degree. I would like to thank Professors Pierre Potvin, Arturo Orellana, and Tom Kirchner for being part of my supervisory and/or examination committee. My grateful thanks are also extended to Dr. Alan Lough from University of Toronto for his help with X-ray analysis, to Dr. Howard Hunter for his help with many NMR experiments, including the characterization of paramagnetic complexes, and to Professor William Pietro for his help with CV experiments and analysis. I would also like to thank Professor A.B.P. Lever and Dr. Elaine Dodsworth for helpful discussions about collecting and analyzing DFT and AOMix data. I wish to thank the past students Richard Morris, Lauren Keyes, Nick Zinck and present students Juan Rodriguez, Mykhaylo Romanyuk, and Matthew Wiebe of the Lavoie Group for their help and support throughout my degree.

I wish to acknowledge the financial support provided by Enbridge and the Government of Ontario through the Enbridge Graduate Student Awards and the Ontario Graduate Scholarship.

Finally, I wish to thank my family, and especially my parents Majida and Saad, for their immense love and support throughout my degree.

Contents

Abstract	ii
Acknowledgments	iv
List of Tables	viii
List of Figures	xi
List of Schemes	xiii
List of Abbreviations	xiv
1 General Introduction	1
1.1 Bis(amino)pyridines	1
1.2 Synthesis and Coordination Chemistry of Bis(amido)pyridine	3
1.3 Summary of Research Objectives	8
2 Olefin Metathesis	10
2.1 Introduction	10
2.1.1 Ruthenium-based Catalysts	12
2.1.2 Ruthenium Alkylidenes Supported by Tridentate ligands	17
2.1.3 Research Plan for 2,6-bis(amido)pyridine Ruthenium Alkylidenes	18
2.2 Results and Discussion	21
2.2.1 Reactions $[\text{NNN}]^{2-}$ Dianion with RuX_2 Precursors	21
2.2.2 Amido and Organoruthenium Precursors	25
2.2.3 Coordination of $\text{H}_2[\text{NNN}]$ to Ruthenium	25
2.2.4 Computational Model	27
2.3 Conclusion and Future Remarks	34
2.4 Experimental	36
3 Cobalt-based Polymerization Catalysts	43
3.1 Introduction	44
3.2 Coordination Polymerization of Alkenes	45
3.2.1 Bis(imino)pyridine-supported Cobalt(II) Catalysts for Olefin Poly- merization	47
3.2.2 Bis(amido)pyridine Organocobalt Complexes	51
3.2.3 Beyond Olefin Polymerization	53
3.2.4 Research Plan for 2,6-bis(amido)pyridine Cobalt(III) Complexes .	57
3.3 Results and Discussion	60
3.3.1 Preparation and Reactivity of Cobalt(III) Complexes	60
3.3.2 X-ray Studies	64

3.3.3	Cyclic Voltammetry	67
3.3.4	Density Functional Theory Calculations	68
3.4	Conclusions and Future Remarks	73
3.5	Experimental	75
References	82
Appendix	90
	NMR spectra of 2	90
	X-ray crystallography data of 2	96
	NMR spectra of 3a	109
	NMR spectrum of 3b	124
	NMR spectrum of 4	125
	X-ray crystallography data of 4	126
	DFT calculations	138

List of Tables

3.1	Selected bond lengths (\AA) and bond angles (deg) for complexes 2 , 3a and 4 .	67
3.2	Crystal data and structure refinement for complex 2	96
3.3	Fractional Atomic Coordinates ($\times 10^4$) and Equivalent Isotropic Displacement Parameters ($\text{\AA}^2 \times 10^3$) for complex 2 . U_{eq} is defined as 1/3 of the trace of the orthogonalised U_{IJ} tensor.	98
3.4	Anisotropic Displacement Parameters ($\text{\AA}^2 \times 10^3$) for complex 2 . The Anisotropic displacement factor exponent takes the form: $-2\pi^2[h^2a *^2 U_{11} + 2hka * b * U_{12} +]$	101
3.5	Bond Lengths for complex 2	104
3.6	Bond Angles for complex 2	106
3.7	Crystal data and structure refinement for complex 3a	111
3.8	Fractional Atomic Coordinates ($\times 10^4$) and Equivalent Isotropic Displacement Parameters ($\text{\AA}^2 \times 10^3$) for complex 3a . U_{eq} is defined as 1/3 of the trace of the orthogonalised U_{IJ} tensor.	113

3.9	Anisotropic Displacement Parameters ($\text{\AA}^2 \times 10^3$) for complex 3a . The Anisotropic displacement factor exponent takes the form: $-2\pi^2[h^2a *^2 U_{11} + 2hka * b * U_{12} +]$	116
3.10	Bond Lengths for complex 3a	119
3.11	Bond Angles for complex 3a	121
3.12	Crystal data and structure refinement for complex 4	126
3.13	Fractional Atomic Coordinates ($\times 10^4$) and Equivalent Isotropic Displacement Parameters ($\text{\AA}^2 \times 10^3$) for complex 3a . U_{eq} is defined as 1/3 of the trace of the orthogonalised U_{IJ} tensor.	128
3.14	Anisotropic Displacement Parameters ($\text{\AA}^2 \times 10^3$) for complex 3a . The Anisotropic displacement factor exponent takes the form: $-2\pi^2[h^2a *^2 U_{11} + 2hka * b * U_{12} +]$	131
3.15	Bond Lengths for complex 3a	134
3.16	Bond Angles for complex 4	136
3.17	Energy and composition of frontier molecular orbitals in terms of Co^{3+} , $[\text{NNN}]^{2-}$, and second donor fragments. Matching singly occupied α -, β -orbitals of complexes 2 , 3a and 4 and resemblance factor q^a	138
3.18	Optimized coordination for complex 2	139
3.19	Optimized coordinates of complex 3a	145
3.20	Optimized coordinates of complex 4	153

List of Figures

1.1	General representation of complex with coordinated pincer ligand.	2
1.2	Bonding interactions of bis(amido)pyridine pincer when coordinated to metal center.	3
2.1	General mechanism of olefin metathesis reaction.	11
2.2	Several types of olefin metathesis reactions that can be performed by Schrock- and Grubbs- type catalysts.	11
2.3	Examples of Schrock- and Grubbs-type catalysts.	13
2.4	Ruthenium-catecholate catalysts along with the corresponding pKa values of the conjugate acid. Adopted from reference 54.	17
2.5	Structure of square pyramidal bis(amido)pyridine supported ruthenium complex where the alkylidene adopts the axial position.	18
2.6	Theoretical conformations of 14 VE [NNN]Ru(CH ₂) complexes. Designation of 'cis' and 'trans' is with respect to the pyridine nitrogen of [NNN] ligand.	28
2.7	Stable conformations of [NNN]Ru(CH ₂) and [NNN]Ru(CH ₂)PMe ₃ complexes based on DFT calculations.	30

2.8	Energy diagram of the intermediates in olefin metathesis cycle.	33
3.1	Polypropylene showing three different stereochemical configurations. . . .	47
3.2	Bis(imino)pyridine supported Fe and Co precatalysts.	49
3.3	Proposed reactivity of [NNN]Co(III)Me complex (top) with MAO closely mimics that of [N _{imino} NN _{imino}]Co(I)Me (bottom) with MAO.	52
3.4	UV-Vis spectra of 1 (long dashed; blue), 2 (dotted; red), 3a (short dashed; green), and 4 (solid line; yellow) in dichloromethane (0.05 M) at room temperature.	63
3.5	ORTEP representations of 2 (top), 3a (middle), 3c (bottom) (50% probability level). Most hydrogens atoms, the BF ₄ counteranion in 2 and solvent molecules in 3a and 3c were removed for clarity. Selected bond lengths and angles are presented in Table 3.1.	66
3.6	Cyclic voltammograms of 2 (dotted; red), 3a (dashed; green), 4 (solid line; yellow) in dichloromethane (0.1 M Bu ₄ N(PF ₆)) at room temperature (scan rate 100 mVs ⁻¹).	68
3.7	π -Character of the Co-N _{2,3} bonds in complex 2 (isovalue of 0.04 e ⁻ /Å ³).	70
3.8	HSOMO and HSOMO-1 of complex 3a (isoval 0.045 e ⁻ /Å ³).	71
3.9	¹ H NMR (400 MHz; CD ₂ Cl ₂) spectrum of Complex 2	90
3.10	¹³ C ¹ H NMR (400 MHz; CD ₂ Cl ₂) spectrum of 2	91
3.11	¹⁹ F NMR (400 MHz; CD ₂ Cl ₂) spectrum of 2	92
3.12	¹ H- ¹ H COSY (400 MHz; CD ₂ Cl ₂) spectrum of 2	93
3.13	¹ H- ¹³ C HMBC (400 MHz; CD ₂ Cl ₂) spectrum of 2	94

3.14	^1H - ^{13}C HSQC (400 MHz; CD_2Cl_2) spectrum of 2	95
3.15	^1H NMR (400 MHz; C_6D_6) spectrum of Complex 3a	109
3.16	^1H - ^1H COSY (400 MHz; C_6D_6) spectrum of 3a	110
3.17	^1H NMR (400 MHz; C_6D_6) spectrum of Complex 3b	124
3.18	^1H NMR (400 MHz; C_6D_6) spectrum of Complex 4	125
3.19	Selected MOs of complex 2	144
3.20	Selected MOs of complex 3a	152
3.21	Selected MOs of complex 4	158

List of Schemes

1.1	Coordination of bis(amido)pyridine ligand to a metal center via trimethylsilyl derivative of bis(amino)pyridine.	4
1.2	Synthesis procedure of bis(amino)pyridine ligands.	6
2.1	Decomposition pathway of ruthenium-methylidene complex.	15
2.2	Phosphaalkene and imine-functionalized NHC insertion in the alkylidene moiety of GI.	15
2.3	Proposed synthetic methods to produce [NNN]Ru(CHR)L.	20
2.4	Reaction of in situ prepared $\text{Li}_2[\text{NNN}]''$ and $\text{Li}_2[\text{NNN}]'$ with $\text{RuCl}_2(\text{PPh}_3)_3(\text{py})_2$ precursors.	23
2.5	Reaction of $[\text{NNN}]''\text{Mg}(\text{THF})_2$ with $\text{RuCl}_2(\text{COD})$ in the presence of pyridine.	24
2.6	Possible conformations of 16-VE $[\text{NNN}]\text{Ru}(\text{CH}_2)\text{PMe}_3$ complexes from the 14-VE conformers.	30
2.7	Conformational exchange of <i>cis</i> - $[\text{NNN}]''\text{Ru}(\text{CH}_2)$ and <i>trans</i> - $[\text{NNN}]''\text{Ru}(\text{CH}_2)$ after one olefin metathesis cycle.	31
3.1	General mechanism of cobalt-mediated radical polymerization.	44

3.2	General mechanism of metallocene polymerization catalysts.	46
3.3	Oligomerization of ethylene using the SHOP catalyst.	48
3.4	Activation reactions of the bis(imino)pyridine Co(II) dihalide precatalyst with excess MAO to form the Co(I) ethylene adduct.	50
3.5	Proposed initiation step of $[[N_{imino}NN_{imino}]Co(I)Me]^+$	51
3.6	Mechanism of Co(III)-based ethylene polymerization catalyst.	51
3.7	Inner-sphere asymmetric hydrogenation mechanism of functionalized ke- tones via a 4-membered transition state using (BINAP)Ru precatalyst. . .	54
3.8	Outer-sphere asymmetric hydrogenation mechanism of ketones via 6-membered transition state using (BINAP)Ru diamine precatalyst.	55
3.9	Asymmetric transfer hydrogenation using iron(II) pincer precatalyst. . .	56
3.10	Chemical transformations of bis(amido)pyridine cobalt(III) complexes aimed at olefin polymerization and hydrogenation chemistry.	59
3.11	Synthesis of 2	60
3.12	Synthesis of Co(III) complexes 3 and 4	61

List of Abbreviations

Ar	Aryl
Ar _F	Pentafluorophenyl
B.M	Bohr magneton
BINAP	2,2'-Bis(diarylphosphaneyl)-1,1'-dinaphthalene
br	Broad
CCDC	Cambridge crystallographic data center
CMRP	Cobalt mediated radical polymerization
COD	1,4-Cyclooctadiene
Cp'	Cyclopentadiene-based ligand
Cy	Cyclohexane
d	Doublet
DCM	Dichloromethane
DFT	Density Functional Theory
DME	Dimethoxyethane
E _{1/2}	Half-wave potential
E _{pa}	Anodic potential
E _{pc}	Cathodic potential
GI	First-generation Grubbs catalyst
GII	Second-generation Grubbs catalyst
H ₂ [NNN]	2,6-Bis(aminoalkyl)pyridine, or bis(amino)pyridine
H ₂ [NNN]'	2,6-Bis(anilinomethyl)pyridine

H ₂ [NNN]"	2,6-Bis(anilinoisopropyl)pyridine
HDPE	High-density polyethylene
HOMO	Highest occupied molecular orbital
HSOMO	Highest singly occupied molecular orbital
Hz	Hertz
IMes	1,3-Dimesityl-imidazol-2-ylidene
ⁱ Pr	Isopropyl
<i>J</i>	coupling constant
KHMDS	Potassium hexamethyldisilazide
L	Neutral donor
LDPE	Low-density polyethylene
LLDPE	Linear low-density polyethylene
LSUMO	Lowest singly occupied molecular orbital
LUMO	Lowest unoccupied molecular orbital
M	Any metal
m	Multiplet
<i>m</i>	Meta
MAO	Methylaluminoxane
MCB	Metallocyclobutane
Me	Methyl
MeCN / NCMes	Acetonitrile
Mes	Mesityl
MHz	Megahertz
MMAO	Modified MAO
N _{<i>imino</i>} NN _{<i>imino</i>}	Bis(imino)pyridine
NHC	N-Heterocyclic Carbene
NMR	Nuclear magnetic resonance

NNN _{<i>imino</i>}	Aminoiminopyridine
<i>o</i>	Ortho
<i>p</i>	Para
PE	Polyethylene
Ph	Phenyl
PP	Polypropylene
py	Pyridine
R	Alkyl
RCM	Ring-opening metathesis
ROMP	Ring-opening metathesis polymerization
RT	Room temperature
s	Singlet
SHOP	Shell higher olefin process
sol	Solvent
t	Triplet
^t Bu	Tertbutyl
THF	Tetrahydrofuran
TMEDA	Tetramethylethylenediamine
Tos	Tosylate
VE	Valence electrons
X	Halide
xyl	Xylyl

Chapter 1

General Introduction

1.1 Bis(amino)pyridines

Pincer ligands, also simply referred to as pincers, are a versatile class of tridentate ligands characterized by adopting a meridional geometric arrangement when coordinated to a metal center. The coordinating atoms of pincers can be a combination of C, N, P, O, or S functional groups. Pincer ligands are commonly abbreviated in the literature to 'EDE' where 'E' and 'D' represent the coordinating atoms (Figure 1.1). The flexibility in modifying the electronic and steric properties of pincers allow for precise control of the reactivity in pincer-supported complexes. Monometallic complexes supported by

pincer ligands are limited to octahedral, trigonal bipyramidal, square planar or T-shaped geometries.¹ Complexes supported by PCP and NCN pincer ligands were first reported in the mid- to late-70s by Shaw,² van Koten and Noltes.³ Since then, many systems have been developed to catalyze reactions such as the Kharasch addition, the Heck and the Suzuki-Miyaura coupling, and hydrogen transfer reactions.⁴

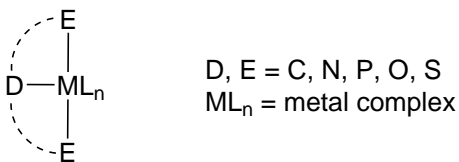


Figure 1.1: General representation of complex with coordinated pincer ligand.

This thesis focuses on one type of dianionic pincer ligand prepared from the protio-bis(amino)pyridine ($\text{H}_2[\text{NNN}]$), which is a pyridine backbone linked to two amino groups at the 2,6-positions by a carbon linker. The amines, generally anilines, can be deprotonated to generate dianionic bis(amido)pyridine ($[\text{NNN}]^{2-}$) pincer ligands. When coordinated to a metal center, bis(amido)pyridines are formally 6-electron donors via three σ -interactions, with additional π -electron density available from two filled p-orbitals on the anilide nitrogen atoms (Figure 1.2). These electron-rich ligands can stabilize coordinatively unsaturated and low valence-electron-count complexes. Furthermore, the pincer nature of the bis(amido)pyridines forces the amido groups to adopt a normally disfavored trans configuration when coordinated to a metal center. This coordination mode forces

the two filled amido p -orbitals to interact with one metal d -orbital. As presented in this thesis, metal-amide double bond character with a bond order of 1.5 can develop which was observed and confirmed through solid-state structures and DFT computations (Chapter 3).

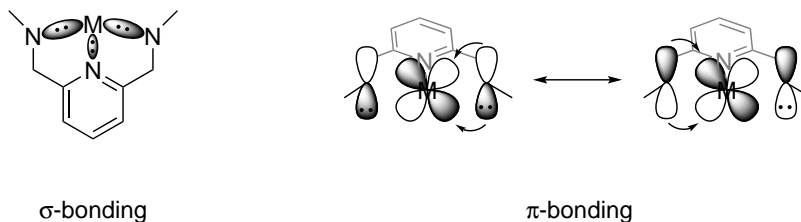


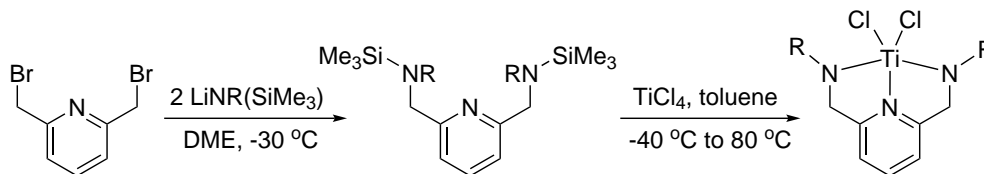
Figure 1.2: Bonding interactions of bis(amido)pyridine pincer when coordinated to metal center.

1.2 Synthesis and Coordination Chemistry of

Bis(amido)pyridine

Coordination of bis(amido)pyridine $[\text{NNN}]^{2-}$ to a metal center can be accomplished in three main ways. The first method is via preparation of the bis(amido)pyridine dianion followed by salt metathesis with a metal dihalide. The $[\text{NNN}]$ dianion is known to be unstable at room temperature and must be prepared in situ and used at low temperatures.^{5,6} The second method eliminates the separate base addition step by using metal-alkyl/amido precursors. The alkyl/amido groups act as bases and deprotonate

the amine functionality opening two sites on the metal for bis(amido)pyridine coordination.^{7,8} The third method is based on producing trimethylsilylhalide as a side-product from trimethylsilyl derivative of bis(amino)pyridine and metal halide (Scheme 1.1).⁹



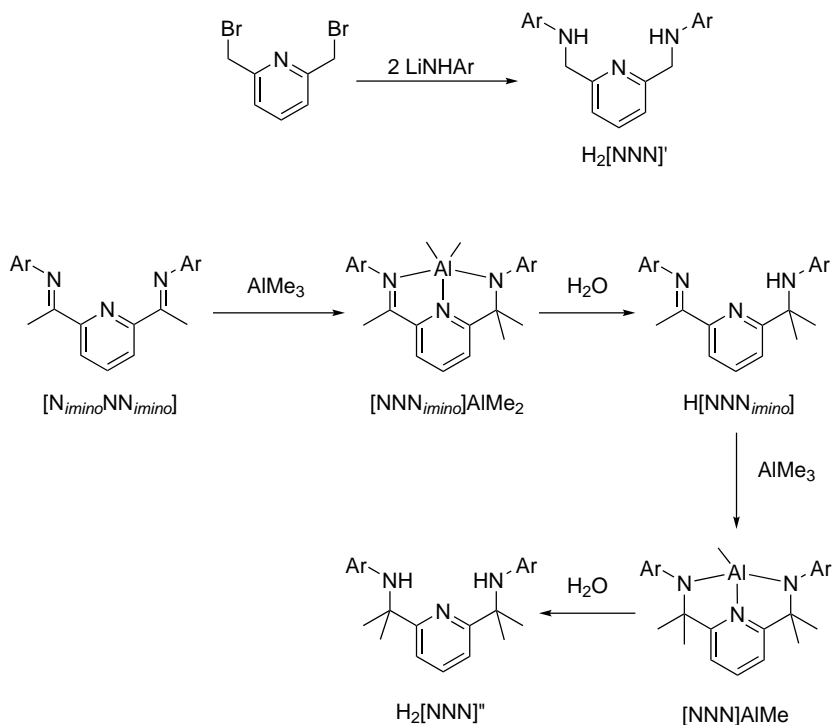
Scheme 1.1: Coordination of bis(amido)pyridine ligand to a metal center via trimethylsilyl derivative of bis(amino)pyridine.

The coordination chemistry of bis(amido)pyridine is limited to early transition metals and a few lanthanides. McConville reported the synthesis of bis(amido)pyridine and its coordination to Ta,¹⁰ Ti^{9,11} and Zr^{8,12} in search for a non-metallocene ethylene polymerization catalyst. Anwender utilized bis(amido)pyridines to synthesize coordinatively unsaturated organo-rare-earth complexes (Sc, Y, and Lu), and showed the Sc complexes were capable of methyl methacrylate polymerization.¹³ Interestingly, the stability of Sc, Y, and Lu complexes decreased with increasing size of the metal center. Emslie reported five-coordinate dialkyl thorium complexes supported with bis(amido)pyridines that are stable at 90 °C for several days.^{5,14} Diaconescu showed that the two amido groups and the geometry imposed by the rigid bis(amido)pyridine on Lu and Y alkyl complexes were important features in predicting their reactivity with aromatic N-heterocycles.¹⁵ More

recently, Ison reported several bis(amido)pyridine-supported oxorhenium complexes, and showed oxygen atom transfer catalysis and the ambiphilic nature of the terminal oxo ligand.^{16,17} The first study to involve coordination of $[\text{NNN}]^{2-}$ to late transition metals was reported in 2015.⁶ Square planar Fe, Co, and Ni complexes were synthesized in which Fe and Co complexes were isolated and characterized successfully. However, the Ni complex decomposed via oxidative dehydrogenation to form bis(imino)pyridine Ni complex.

Most of the coordination chemistry of bis(amino)pyridines has focused on derivatives of the McConville-type ligand, 2,6-bis(anilinomethyl)pyridine $\text{H}_2[\text{NNN}]'$ (Scheme 1.2). It can be prepared via various methods, one of which is through a simple $\text{S}_{\text{N}}2$ reaction between lithium anilide and 2,6-bis(bromomethyl)pyridine in moderate yields.^{9,13} A second type of bis(amino)pyridine, 2,6-bis(anilinoisopropyl)pyridine ($\text{H}_2[\text{NNN}]''$) was discovered serendipitously from unexpected methyl insertions from trimethylaluminum into the *imino* groups of bis(imino)pyridine ($[\text{N}_{\text{imino}}\text{NN}_{\text{imino}}]$) precursors (Scheme 1.2).⁷ Methyl insertion to various positions on the pyridine backbone of $[\text{N}_{\text{imino}}\text{NN}_{\text{imino}}]$ have been observed previously as this ligand is used extensively in ethylene polymerization catalysts.¹⁸⁻²⁰ Ethylene polymerization catalysts use a large excess of methylaluminoxane (MAO) as co-catalyst that provides the source of anionic methyl groups. Preferential methyl insertion to the imine carbon had not been observed until 1998 when

Gibson reported the synthesis of the dimethylaluminum 2,6-iminoamidopyridine complex, $[\text{NNN}_{\text{imino}}]\text{AlMe}_2$ (Scheme 1.2).²¹ The aluminum complex was synthesized from a reaction of AlMe_3 with $[\text{N}_{\text{imino}}\text{NN}_{\text{imino}}]$ in which one of the imino groups was reduced to an amido group upon methyl insertion. The ligand can be isolated via hydrolysis to form the neutral $\text{H}[\text{NNN}_{\text{imino}}]$. The Anwander group observed similar chemistry with tetramethylaluminate lanthanide (Me_4AlLn , $\text{Ln} = \text{La}, \text{Nd}, \text{Y}$) complexes and imino-aminopyridine, $\text{H}[\text{NNN}_{\text{imino}}]$.²² The reaction between Me_4AlLn and $\text{H}[\text{NNN}_{\text{imino}}]$ produced a $[\text{NNN}_{\text{imino}}]\text{Ln}(\text{Me}_4\text{Al})_2$ complex as the main product, along with $[\text{NNN}_{\text{imino}}]\text{AlMe}_2$ and $[\text{NNN}]\text{MeAl}$ as side-products.



Scheme 1.2: Synthesis procedure of bis(amino)pyridine ligands.

The full synthetic procedure of bis(amino)pyridine was optimized by Wang in 2011 to make the bis(amino)pyridine ligand, $\text{H}_2[\text{NNN}]'$.⁷ The synthetic procedure involved two sequential methyl insertion steps using AlMe_3 as the methyl group source. The first equivalent of AlMe_3 inserts a methyl group into one of the imino functionalities of $[\text{N}_{\text{imino}}\text{NN}_{\text{imino}}]$ to produce $[\text{NNN}_{\text{imino}}]\text{AlMe}_2$, in which the ligand can be freed via hydrolysis. The second AlMe_3 equivalent reacts similarly to produce bis(amido)pyridine aluminum complex $[\text{NNN}]\text{AlMe}$, in which $\text{H}_2[\text{NNN}]'$ can also be freed by hydrolysis (Scheme 1.2).

As will be seen, most of the research presented focuses on $\text{H}_2[\text{NNN}]''$ for two main advantages over $\text{H}_2[\text{NNN}]'$. Firstly, $\text{H}_2[\text{NNN}]''$ does not have β -hydrogens that are prone to abstraction as was observed by Gordon and Summerscales in cobalt(II) and Nickel(II) complexes of $[\text{NNN}]'$.⁶ Secondly, the synthetic procedure of $\text{H}_2[\text{NNN}]''$ allows the introduction of chirality into the ligand for use in enantioselective transformations. Bis(imino)pyridine precursor have two prochiral centers that can be used to synthesize a chiral bis(amino)pyridine ligand by using two different organoaluminum reagents.

1.3 Summary of Research Objectives

The main objective of this research is to explore and expand the coordination chemistry of bis(amido)pyridine ($[\text{NNN}]^{2-}$) ligands to late-transition metals. These complexes could be used to mediate catalytic transformations such as polymerization of alkenes and lactones, olefin metathesis, and hydrogenation of alkenes and carbonyls. This thesis will focus on how complexes supported by bis(amido)pyridine ligands can address issues faced in olefin metathesis and olefin polymerization catalysts.

The alkylidene functionality in Ru catalysts, which is critical for olefin metathesis, is electrophilic and prone to decomposition in the presence of weak nucleophiles. Chapter 2 describes the research aimed at using bis(amido)pyridine ligand $[\text{NNN}]^{2-}$ in Ru complexes, replacing both chloride ligands, to make the bis(amido)pyridine Ru alkylidene $[\text{NNN}]\text{Ru}(\text{CHR})\text{L}$ (L is neutral donor). This complex is predicted to have a more robust alkylidene moiety and to resist alkylidene-based decomposition.

Chapter 3 presents work aimed at understanding the coordination chemistry of $[\text{NNN}]^{2-}$ to first-row late transition metals. Research focused on cobalt to explore the reactivity of organocobalt(III) complexes supported by bis(amido)pyridines. Catalytic transformations of cobalt(III) are discussed with a focus on olefin polymerization. Current

bis(imino)pyridine Co(II) catalysts ($[N_{imino}NN_{imino}]CoCl_2$) are discussed and similarities to the target $[NNN]CoR$ complex are highlighted. Also in this chapter is a brief look at the hydrogenation chemistry of carbonyl and the viability of $[NNN]CoL$ complexes as hydrogenation catalysts.

Chapter 2

Olefin Metathesis

2.1 Introduction

Olefin metathesis is an organic transformation based on breaking and forming carbon-carbon double bonds and catalyzed by a metal-carbene/alkylidene fragment ($M=CR_2$).

Olefin metathesis was observed as early as 1930 by Calderon and the first “targeted” catalysis appeared in 1950.²³ Several mechanisms were proposed, with the one by Chauvin and Hérisson in 1970 being widely accepted today.²⁴ Their mechanism involves the coordination of an olefin to a metal alkylidene complex, followed by the formation of a metallacyclobutane intermediate through a [2+2] cycloaddition (Figure 2.1). The met-

allacyclobutane can collapse to produce a new carbon-carbon double bond or regenerate the starting material.

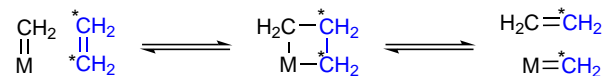


Figure 2.1: General mechanism of olefin metathesis reaction.

Several types of olefin metathesis reactions can be carried out by the well-defined homogeneous Schrock- and Grubbs-type catalysts. These catalysts have shown to be useful in a wide range of applications.²⁵⁻²⁷ Some of the most prominent reactions include cross metathesis (CM), ring-closing metathesis (RCM), ring-opening metathesis polymerization (ROMP), ring-opening cross metathesis (ROCM), and acyclic diene metathesis polymerization (ADMET), all shown in Figure 2.2.

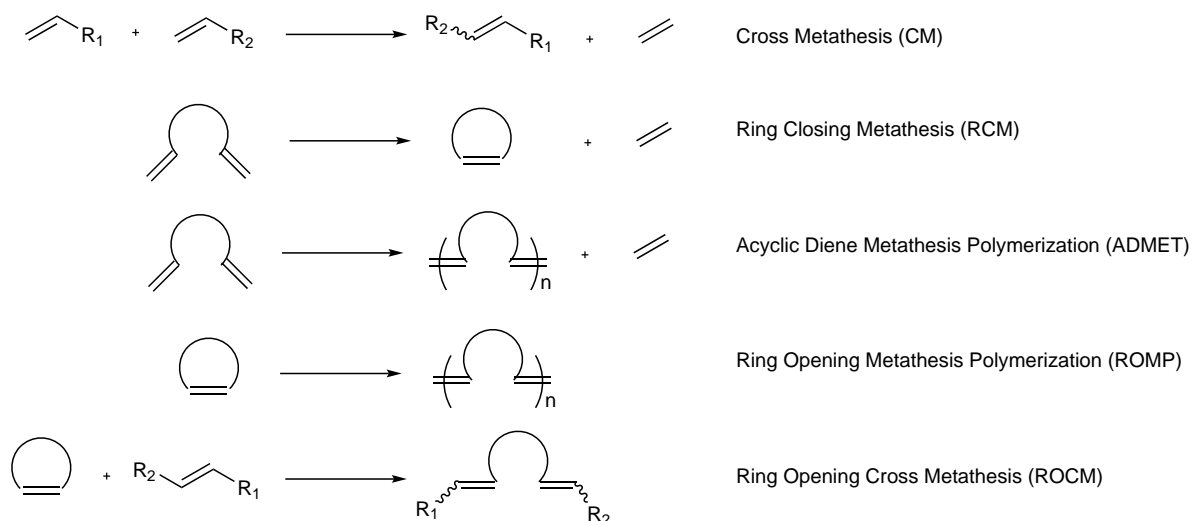


Figure 2.2: Several types of olefin metathesis reactions that can be performed by Schrock- and Grubbs- type catalysts.

The Schrock group reported the earliest proof of the Chauvin mechanism in 1980 where the metathesis of two cis-2-pentene molecules was catalyzed by the tantalum alkylidene complex $\text{Ta}(=\text{CH}^t\text{Bu})\text{Cl}(\text{PMe}_3)(\text{O}^t\text{Bu})_2$.²⁸ A family of Mo(VI) and W(VI) alkylidenes was soon developed based on the chemical formula $\text{M}(=\text{CHCMe}_2\text{R})(=\text{NAr})(\text{OR}')_2$ ($\text{R} = \text{Me}, \text{Ph}; \text{R}' = \text{O}^t\text{Bu}$) (Figure 2.3).^{29,30} However, one of the drawbacks of these catalysts was the nucleophilicity of the alkylidene moiety toward protic substrates and solvents, which limited their applications to aprotic substrates in oxygen-free and moisture-free environment. A less reactive ruthenium-based catalyst was shortly reported by Grubbs (see below).

2.1.1 Ruthenium-based Catalysts

Grubbs and coworkers reported an interesting finding in 1988 where metathesis activity was observed in protic solvents using a $\text{RuCl}_3(\text{H}_2\text{O})_3$ and a $\text{Ru}(\text{H}_2\text{O})_6(\text{tos})_2$, hinting to an in situ formation of a Ru-carbene moiety.³¹ Several years later, this hypothesis was confirmed with the isolation of an active and well-defined catalyst, $\text{RuCl}_2(=\text{CHPh})(\text{PCy}_3)_2$, often referred to as the first-generation Grubbs catalyst (GI).^{32,33} While less active than Schrock's group 6 catalysts, these ruthenium-based catalysts exhibited remarkable stability toward functional groups and tolerance to oxygen and moisture.³⁴

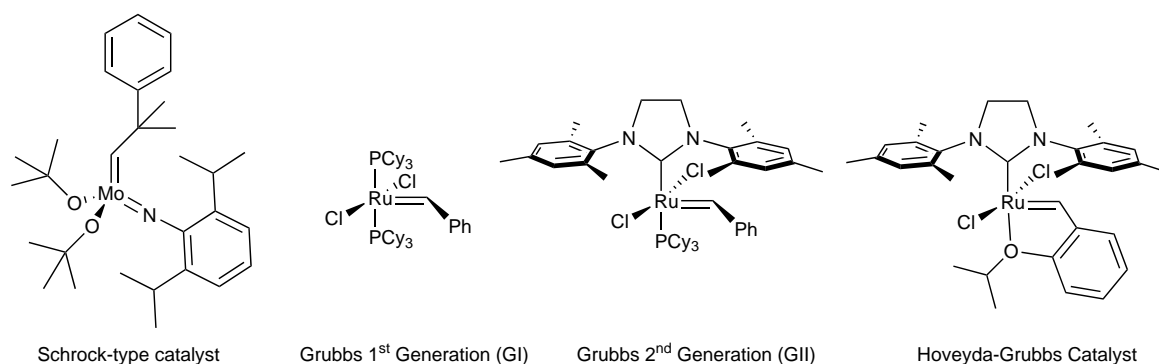


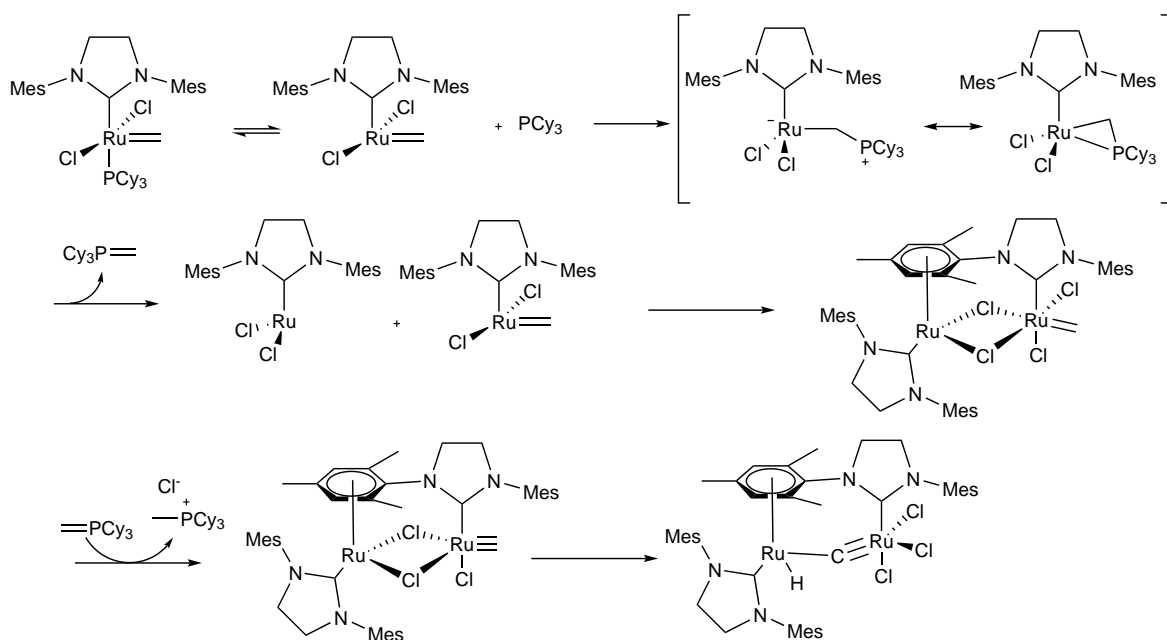
Figure 2.3: Examples of Schrock- and Grubbs-type catalysts.

During the late 1990s, the recently discovered class of ligands called N-heterocyclic carbenes (NHCs) were shown to be stronger σ -donors compared to phosphines.³⁵ Studies aimed at using NHCs to substitute one of the phosphine ligand in GI led to a more active second-generation (GII) catalyst, $\text{RuCl}_2(=\text{CHPh})(\text{PCy}_3)(\text{NHC})$.^{35,36} These systems have become the basis for further studies in developing and enhancing ruthenium-based olefin metathesis catalysis. As such, the Hoveyda-Grubbs catalyst is a close derivative of GII and contains a chelating styrenyl ether ligand that serves as the alkylidene fragment and a phosphine substitute (Figure 2.3). This chelating configuration not only allowed for enhanced air and water stability, but also recyclability with high recovery yields using simple silica-gel chromatography.³⁷

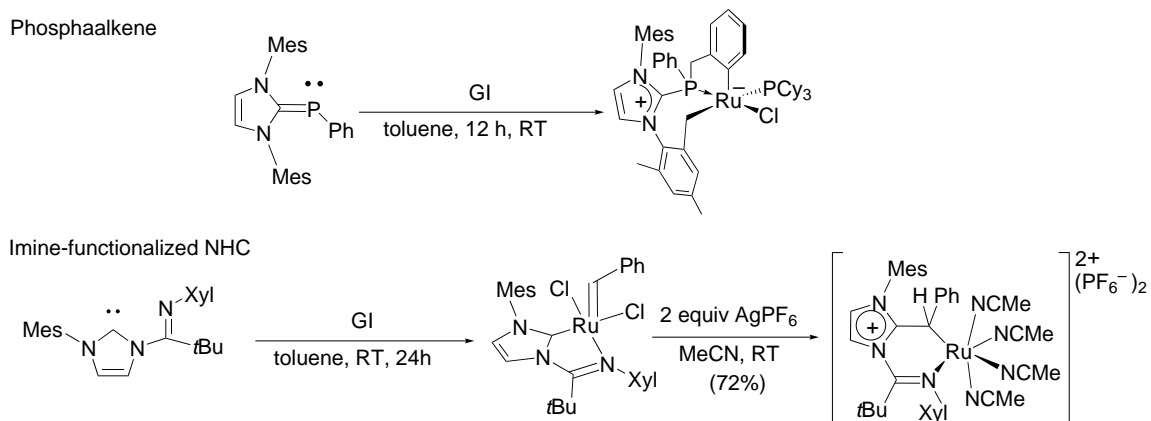
Studies to improve the activity and stability of Grubbs-type catalysts have usually focused on neutral donors. The halides however have received less attention and reports that focused on halide substitution in Grubbs-type catalysts are limited. “Pseudohalide”

derivatives of Grubbs-type catalysts have been studied by the Fogg³⁸⁻⁴¹ and Buchmeiser groups^{42,43} using alkoxide/phenoxide and carboxylate ligands. A motivation for such studies was to mitigate catalyst deactivation pathways that resulted from the formation of Cl-bridged dimers. The decomposition mechanism of ruthenium-methylidene complex under metathesis conditions was proposed by Grubbs among others.^{44,45} The pathway starts by phosphine dissociation, which subsequently attacks the methylidene moiety to generate methylphosphine ylide and $\text{RuCl}_2(\text{NHC})$ (Scheme 2.1). The Cl-bridged dimer is produced when the highly unstable 3-coordinate $\text{RuCl}_2(\text{NHC})$ reacts with another $\text{RuCl}_2(\text{CH}_2)(\text{NHC})$.^{44,46} The Cl-dimer continues reacting intramolecularly to produce a carbon-bridged bimetallic ruthenium complex. The inherent electrophilicity of the alkylidene indicates that it is prone to similar reactivity with weak nucleophiles (for example amines).⁴⁷ The Lavoie group has observed similar reactivity upon substitution of phosphine with phosphalkene and imine-functionalized NHC. (Scheme 2.2).^{48,49}

The electrophilicity of the alkylidene becomes more problematic when Grubbs-type catalysts undergo rapid intermolecular halide exchange reactions. Slugovc studied chloride-to-iodide exchange reactions in Hoveyda-Grubbs system under different solvents and reported two important results.⁵⁰ The first showed that upon isomerization of chlorides from the trans- to the cis-conformation, the chloride ligand trans to the NHC was more



Scheme 2.1: Decomposition pathway of ruthenium-methylidene complex.



Scheme 2.2: Phosphaalkene and imine-functionalized NHC insertion in the alkyldene moiety of GI.

susceptible to dissociation. The second result highlighted that chloride-to-iodide exchange reactions occurred through a dissociative mechanism in the presence of trace donor solvents such as methanol. Computational work by Cavallo group even suggested that halide dissociation can be competitive with neutral ligand dissociation in relatively

polar solvents.⁵¹ Chloride dissociation under metathesis conditions produces a cationic ruthenium alkylidene that amplifies the electrophilicity of the alkylidene moiety and accelerates decomposition reactions.

Dimerization of the 3-coordinate ruthenium complex with the catalytically active $\text{RuCl}_2(\text{CH}_2)(\text{NHC})$ can be minimized by substituting the halides with more rigid ligands. Fogg and coworkers have demonstrated the possibility of chloride substitution with retention of activity in the GII. Using highly toxic thallium pentahalophenoxide as a transmetallating agent, mono- and di-phenoxide Ru complexes were isolated. Their catalytic activity was comparable to those observed using the second-generation catalyst.^{40,41} Grubbs⁵² and Mol⁵³ also studied halide and carboxylate derivatives, respectively. However, activity trends based on the electronic properties of the anionic ligands were also influenced by the ligand size. To deconvolute the effect of sterics and electronics on catalytic activity, Fogg and coworkers developed a series of catecholate catalysts based on GII, where the degree of π -electron donating ability of the oxygen atom of the catecholate was estimated by the pKa of its conjugate acid.⁵⁴ A decrease in the basicity of the catecholates decreases the metathesis activity of catalysts in RCM and ROMP (Figure 2.4). Ligands that are more basic than catecholates could thus possibly lead to an increase in catalytic activity. Moreover, basic ligands can possibly enhance the stability of the alkyl-

dene moiety in substrates containing weak nucleophiles. Increasing the basicity of the ligand could potentially increase π -donation into the ruthenium atom thereby increasing π -backdonation into the alkylidene moiety, decreasing its electrophilicity.

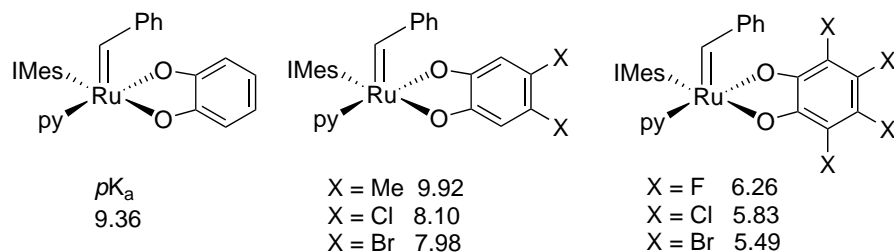


Figure 2.4: Ruthenium-catecholate catalysts along with the corresponding pK_a values of the conjugate acid. Adopted from reference 54.

2.1.2 Ruthenium Alkylidenes Supported by Tridentate ligands

The decomposition pathways of the $RuX_2(=CHR)L$ framework are centered around the electrophilicity of alkylidene and lability of the chlorides. Therefore, modifications to the metal coordination sphere must produce a nucleophile-resilient alkylidene with strongly-bonded anionic ligands. The effect of replacing the halides with mono- and bidentate anionic ligands has been explored.⁵⁵ However, the use of dianionic tridentate ligands as halide substitutes in ruthenium alkylidenes complexes has not been widely explored. The Stephan group published a few reports in this area using ligands such as dithiolate ether⁵⁶ and bis(ethoxide)ether.⁵⁷ The dianionic dithiolate and bis(ethoxide) ethers adopted facial conformation in the corresponding ruthenium alkylidenes and showed metathesis activity

upon activation with Lewis acid, BCl_3 . The first equivalent of BCl_3 is split to form a Ru-Cl moiety and a cationic BCl_2 fragment that associates with the dithiolate ligand. The second equivalent BCl_3 abstracts the chloride ligand to generate catalytically active and cationic Ru complex and BCl_4 counter anion. The Erker group investigated ruthenium benzylidenes containing more a rigid 2,6-bis(carboxamido)pyridine ligand and reported metathesis activities comparable to those for the GI and GI alkylidene analogs.⁵⁸

2.1.3 Research Plan for 2,6-bis(amido)pyridine Ruthenium

Alkylidenes

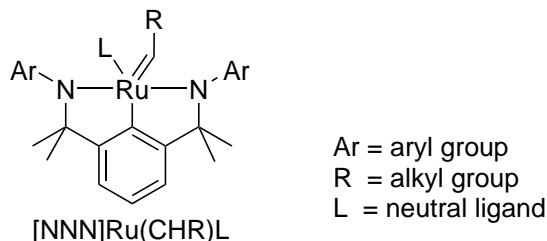


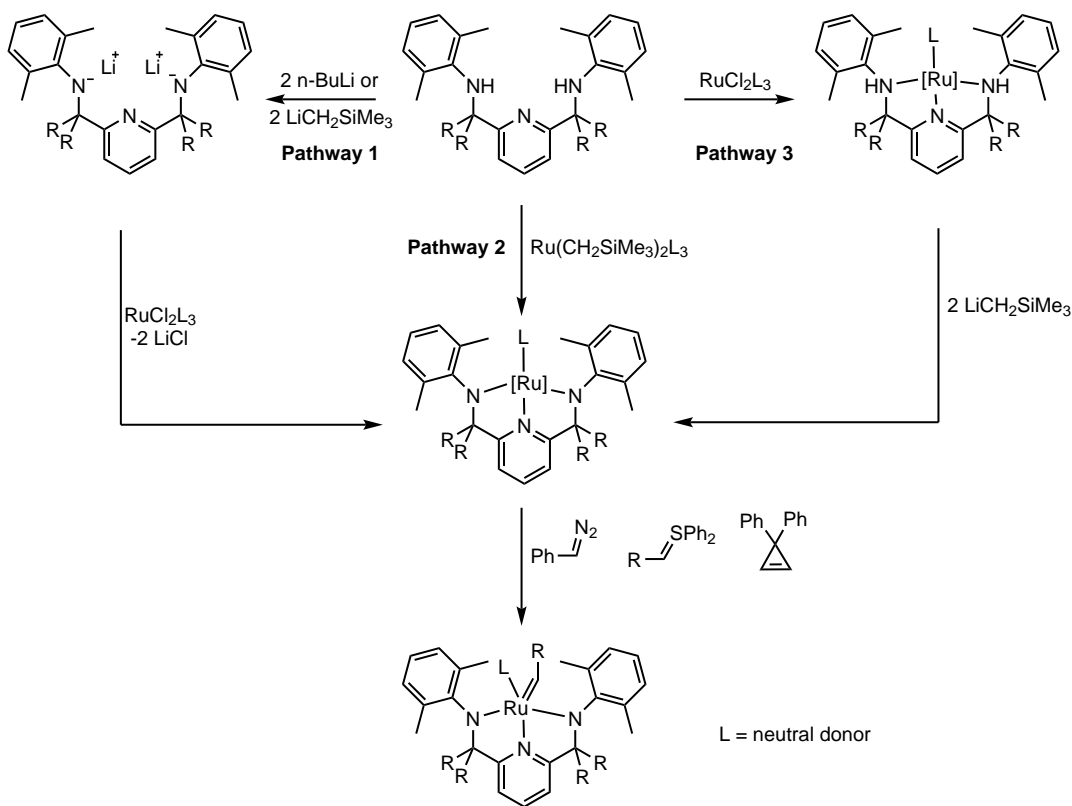
Figure 2.5: Structure of square pyramidal bis(amido)pyridine supported ruthenium complex where the alkylidene adopts the axial position.

Following Erker's results, we became interested in using pincer bis(amido)pyridine ($[\text{NNN}]^{2-}$) as a spectator ligand to produce $[\text{NNN}]\text{Ru}(\text{CHR})\text{L}$ (Figure 2.5). The pincer ligand adopts a meridional conformation, thus mimicking the arrangement of phosphine and chloride ligands in Grubbs-type catalysts. The pincer ligand is a strong σ - and

π -donor, thus increasing the electron density at the ruthenium atom and reducing the electrophilicity of the alkylidene fragment. This results in a more stable alkylidene, and broadens the substrate scope of [NNN]Ru(CHR)L complexes to olefins containing nucleophilic functional groups. Furthermore, substitution of the chloride ligands with strongly-bonded [NNN] ligands will add rigidity and inhibit ligand dissociation from the ruthenium center due to the chelating effect.

The proposed method to produce [NNN]Ru(CHR)L complex starts by installing the dianionic ligand followed by addition of alkylidene fragment (pathways 1, 2 and 3 of Scheme 2.3). The coordination of [NNN]²⁻ ligand to Ru can be accomplished based on methods discussed earlier (see 1.1). These methods include transmetallation from alkali/alkaline-earth-metal complexes (pathway 1), reactions with basic organoruthenium precursors (pathway 2), or two-step synthesis involving coordination of neutral H₂[NNN] followed by deprotonation of the ligand (pathway 3). The methylene linker group in 2,6-bis(anilinomethyl)pyridine (H₂[NNN]') and isopropylene linker in 2,6-(anilinoisopropyl)pyridine (H₂[NNN]'') provide diagnostic chemical shifts to monitor the progress of the reaction by ¹H NMR spectroscopy. Introduction of the alkylidene moiety to access [NNN]Ru(CHR)L could possibly be achieved using carbene transfer agents (Scheme 2.3) such as phenyldiazomethane,³³ sulfonium ylide,⁵⁹ phosphonium ylide,⁶⁰ or diphenylcy-

clopropene.³² Successful coordination of the alkylidene moiety can be observed by ¹H NMR spectroscopy, as the alkylidene proton in ruthenium complexes usually resonates well above 15 ppm.³²



Scheme 2.3: Proposed synthetic methods to produce [NNN]Ru(CHR)L.

Density Functional Theory (DFT) calculations can accurately predict the most stable conformations and provide insight into the catalytic cycle intermediates. The Cavallo group⁶¹ compared the results of several computational methods to the experimental data for RCM reactions. While most models performed reasonably well, energy calculations using the M06 functional were in best agreement with the experimental data.

Interestingly, the type of functional and basis set used for geometry optimization had marginal differences. Computationally-inexpensive functionals such as B3LYP can thus be used for geometry optimization, with more expensive functional, such as M06, reserved for more accurate energy calculations done on the geometry-optimized structures. The Goddard group⁶² followed this strategy using B3LYP/LACVP** (shorthand for B3LYP functional with LACVP** basis set) for single point geometry calculations and M06/LACVP++**(2f) (shorthand for M06 functional with the LACVP++**(2f)) for energy calculations to accurately model conformational isomers of GII. The same computational method used by Goddard group was used herein to determine the relative energy differences between all stable conformers.

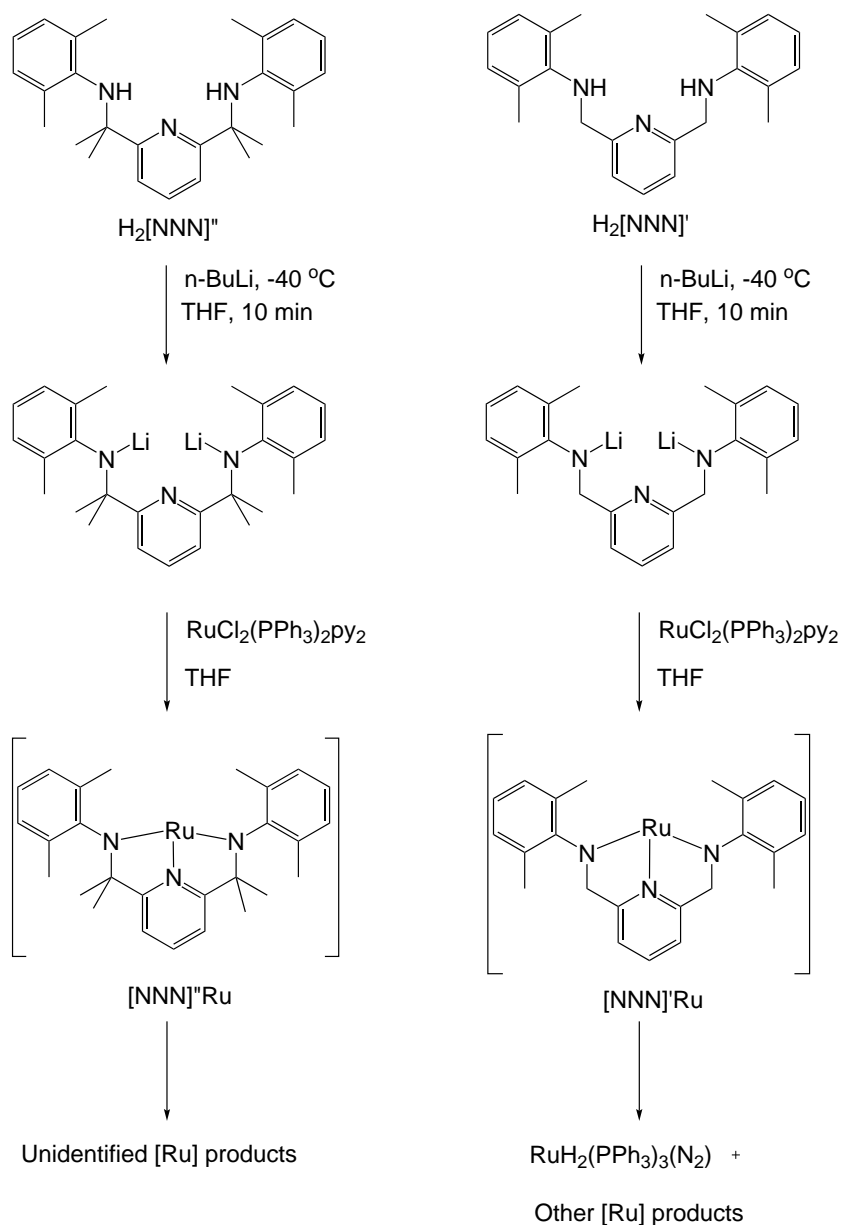
2.2 Results and Discussion

2.2.1 Reactions $[\text{NNN}]^{2-}$ Dianion with RuX_2 Precursors

The approach to synthesize $[\text{NNN}]\text{Ru}(\text{CHR})\text{L}$ complexes was to first coordinate the dianionic $[\text{NNN}]^{2-}$ ligand to a ruthenium(II) precursor, followed by installation of the alkylidene fragment (pathway 1 of Scheme 2.3). $\text{Li}_2[\text{NNN}]$ can be prepared at low temperature (-78 °C), but decomposes to unidentified products at room temperature. In situ

preparation of $\text{Li}_2[\text{NNN}]'$ and $\text{Li}_2[\text{NNN}]''$ followed by addition to either $\text{RuCl}_2(\text{PPh}_3)_2(\text{py})_2$ or $[\text{RuCl}_2(p\text{-cymene})]_2$ was explored. Unfortunately, spectroscopic data of the reaction mixtures did not show evidence of ligand coordination (Scheme 2.4). In a similar reaction using $\text{H}_2[\text{NNN}]'$ ligand and $\text{RuCl}_2(\text{PPh}_3)_2(\text{py})_2$ precursor, a minor side-product identified as a ruthenium hydride species was observed by ^1H and ^{31}P NMR spectroscopy. Chemical shifts of the species observed at δ -8 ppm (doublet of a triplet) in the ^1H NMR spectrum, and at δ 56.7 ppm (doublet) and 44.0 ppm (triplet) in the ^{31}P NMR spectrum are in agreement with the chemical shifts of $\text{Ru}(\text{H})_2(\text{PPh}_3)_3(\text{N}_2)$.⁶³ The ruthenium dihydride species could have formed via β -hydride elimination of the methylene linker (Scheme 2.4). The dihydride complex was one of several species formed during the reaction. These reactions produced highly unstable $[\text{NNN}]\text{Ru}$ species and decomposed rapidly to various ruthenium products that could not be identified.

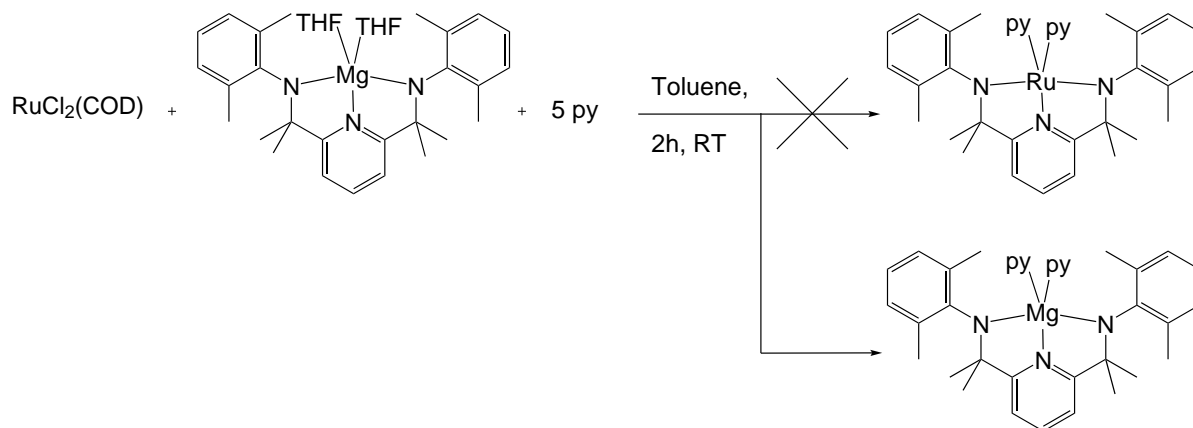
Alkali-earth metals were explored based on a procedure by Wang⁷ to try and slow down the $[\text{NNN}]^{2-}$ transmetallation reaction. $\text{Mg}[\text{NNN}]''$ can be prepared in THF in good yields. However, the reactions of $\text{Mg}[\text{NNN}]''$ and RuX_2 precursors ($\text{RuCl}_2(\text{PPh}_3)_3$, $[\text{RuCl}_2(\text{COD})]_n$, $[\text{RuCl}_2(p\text{-cymene})]_2$) were also not well behaved and often yielded multiple products as determined by ^1H and/or ^{31}P NMR spectroscopy. The electron-deficient $[\text{NNN}]''\text{Ru}$ decomposed very rapidly to various products possibly due to the absence of



Scheme 2.4: Reaction of in situ prepared $Li_2[NNN]''$ and $Li_2[NNN]'$ with $RuCl_2(PPh_3)_3(py)_2$ precursors.

stabilizing donor ligands. Excess steric bulk between the free PPh_3 and the $[NNN]''Ru$ species could prevent the coordination of the PPh_3 to the $[NNN]''Ru$ species. Thus pyridine was investigated as a substitute to the PPh_3 ligand to stabilize the $[NNN]''Ru$

species. Pyridine (py), being planar and relatively small, has minimal steric bulk and could possibly coordinate to form a 16-VE [NNN]Ru(py)₂ or an 18-VE [NNN]Ru(py)₃.



Scheme 2.5: Reaction of [NNN]Mg(THF)₂ with RuCl₂(COD) in the presence of pyridine.

Freshly prepared [NNN]Mg reacted with a toluene solution of RuCl₂(PPh₃)₂(py)₂ producing a new set of alkyl peaks in the ¹H NMR spectrum that was initially predicted to belong to [NNN]Ru(py)₂ complex. Due to difficulties experienced with product isolation, a different Ru precursor was investigated. Reactions of [RuCl₂(COD)]_n with [NNN]Mg adduct in the presence of pyridine produced similar results and several attempts to grow crystals for structural characterization were not successful. During procedure optimizations, the product was identified as [NNN]Mg(py)₂ instead of [NNN]Ru(py)₂ (Scheme 2.5). Addition of pyridine to a [NNN]Mg solution immediately produced [NNN]Mg(py)₂ as yellow solution, which was confirmed by ¹H NMR spectroscopy. Reactions of [NNN]Mg with Ru precursors to produce MgX₂ salt and

[NNN]”Ru(py)₂ complex were not favored due to the formation of a stable 5-coordinate [NNN]”Mg(py)₂.

2.2.2 Amido and Organoruthenium Precursors

Amido and organoruthenium complexes were prepared in situ by reaction of KHMDS or LiCH₂SiMe₃ with ruthenium precursors (RuCl₂(PPh₃)₃, RuCl₂(PPh₃)₂(py)₂, RuCl₂(py)₄, or [RuCl₂(*p*-cymene)]₂). The amido or alkyl groups coordinated to Ru can act as strong bases to deprotonate H₂[NNN]. However, addition of the protio ligand H₂[NNN] to the amido or the organoruthenium complexes did not form a stable [NNN]RuL₂ complex. The amido or organoruthenium species either decomposed before reacting with the protio-ligand, as was the case with LiCH₂SiMe₃ and RuCl₂(PPh₃)₃, or produced various unidentified species.

2.2.3 Coordination of H₂[NNN] to Ruthenium

Difficulties experienced with coordination of bis(amido)pyridine to Ru metal prompted an investigation of the coordination chemistry of the neutral bis(*amino*)pyridine ligand. Coordination of the pincer H₂[NNN]” followed by deprotonation with strong base has been reported for first-row transition metals.⁶ A refluxing mixture of RuCl₂(PPh₃)₃

and $\text{H}_2[\text{NNN}]''$ in THF or acetonitrile did not lead to the coordination of the protio-ligand. In refluxing toluene, the reaction mixture produced a green precipitate while the supernatant contained the $\text{H}_2[\text{NNN}]''$ ligand. Attempts to identify the green product were not pursued as the protio-ligand was recovered quantitatively from the supernatant, indicating that the ligand did not coordinate to Ru. In refluxing methanol, the $\text{RuCl}_2(\text{PPh}_3)_3$ and $\text{H}_2[\text{NNN}]''$ mixture produced a purple precipitate, tentatively identified as a ruthenium hydride complex. The isolated species had a distinct quartet at δ -17 ppm in ^1H NMR spectrum, which is characteristic of a ruthenium hydride complex $\text{RuHCl}(\text{PPh}_3)_3$.⁶⁴ A control reaction of $\text{RuCl}_2(\text{PPh}_3)_3$ refluxed in methanol overnight produced the same ruthenium hydride complex. No reaction was observed between $\text{H}_2[\text{NNN}]''$ and $[\text{RuCl}_2(p\text{-cymene})]_2$ after 3 days in refluxing methanol. The protio-ligand can potentially coordinate to Ru metal in several modes to produce several products. For example, the $\text{H}_2[\text{NNN}]$ ligand could bridge two Ru atoms producing a bimetallic complex. Reasons for the difficulty experienced in forming a ruthenium complex containing a bis(amino)pyridine ligand are not clear.

2.2.4 Computational Model

[NNN]Ru(CHR)L are novel complexes with no experimental or theoretical data reported in the literature. Thus, conformational analysis using DFT calculations can provide valuable insight into the most stable conformers and their ability to undergo a metathesis transformation. Conformational changes during the metathesis cycle can also be explored. As presented in this section, computational data was useful in probing the relative energy of different conformers during metathesis cycle. The data was also useful in providing hints about the effects of steric bulk of PMe_3 on the 16-VE [NNN]Ru(CHR) PMe_3 complex.

The model complexes presented herein were chosen to minimize the computational resources, while still providing insights into the [NNN]Ru(CHR)L complex. The model complex [NNN]Ru(CH_2) PMe_3 is predicted to have two configurations as shown in Figure 2.6, where $=\text{CH}_2$ is either *cis* (*cis*-[NNN]Ru(CH_2)) or *trans* (*trans*-[NNN]Ru(CH_2)) with respect to the pyridine nitrogen (the designation of "cis" and "trans" throughout this chapter are with respect the pyridine nitrogen in bis(amido)pyridine ligand). Each configuration has two conformers depending on the orientation of the $=\text{CH}_2$ fragment with respect to the [NNN] $^{2-}$ ligand. In the interest of clarity, the orientation of $=\text{CH}_2$

group is labeled either **A** or **B**, where **A** refers to the =CH₂ group oriented with the plane of the paper, and **B** refers to the =CH₂ group oriented perpendicular to the plane of the paper. Also, the word ‘stable’ in this section refers to the successful convergence of the structures into an optimized geometry using Gaussian.

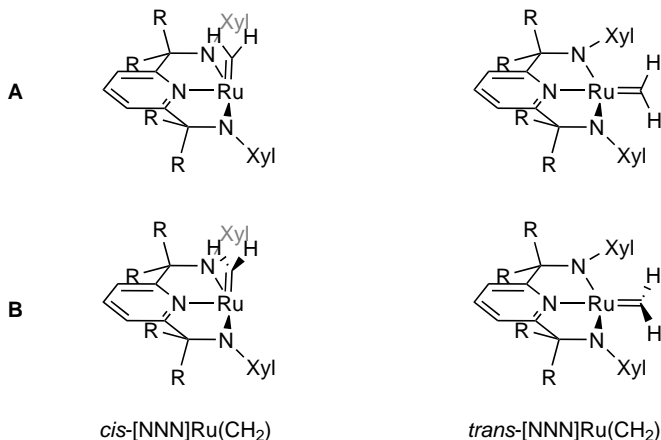


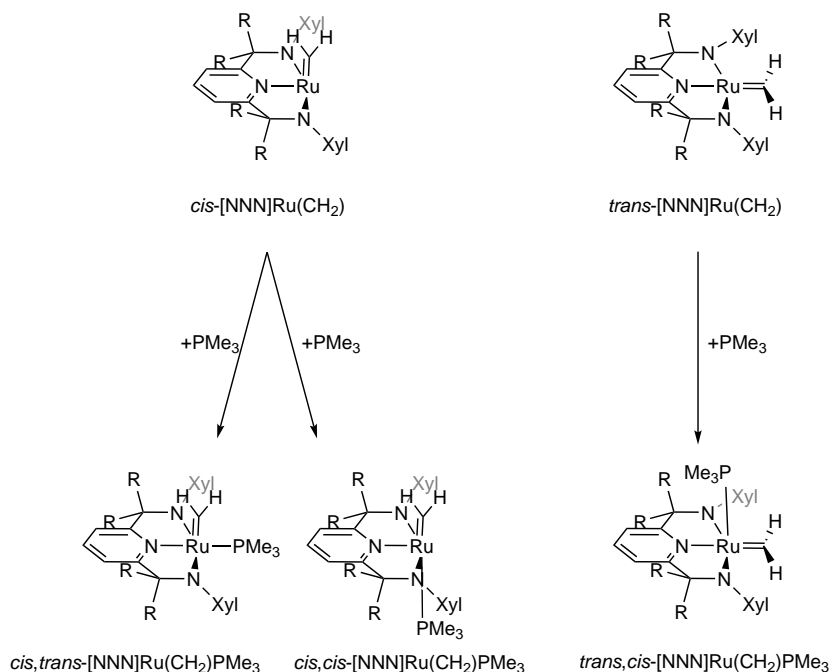
Figure 2.6: Theoretical conformations of 14 VE [NNN]Ru(CH₂) complexes. Designation of ‘cis’ and ‘trans’ is with respect to the pyridine nitrogen of [NNN] ligand.

Density functional theory calculations at B3LYP/LACVP** for geometry optimization and M06/LACVP++**(2f) for energy calculations were performed to probe the relative energies of [NNN]Ru(CH₂) and [NNN]Ru(CH₂)PMe₃ isomers using both [NNN]’ and [NNN]” ligands. Starting from orientation **A** of the *cis*-[NNN]Ru(CH₂) conformer, geometry optimization did not lead to a change of =CH₂ orientation. Thus, *cis*-[NNN]Ru(CH₂) in orientation **A** was assumed to be the most stable *cis* conformer and no further calculations were performed. In contrast, geometry optimization of the *trans*-[NNN]Ru(CH₂) conformer in orientation **A** led to a conformational change to orientation **B**. In a com-

parison between the cis and the trans conformers with either [NNN]' or [NNN]" ligand, both *cis*-[NNN]'Ru(CH₂) and *cis*-[NNN]"Ru(CH₂) were more energetically favorable by 7.5 and 9.0 kcal/mol than their corresponding trans-conformers (Figure 2.7).

The 16-VE [NNN]Ru(CH₂)PMe₃ complexes were studied based on the results of the most energetically favorable 14-VE complexes (*cis*-[NNN]Ru(CH₂) in orientation **A**, and *trans*-[NNN]Ru(CH₂) in orientation **B** (Scheme 2.6). Of the two possible 16-VE conformers of *cis*-[NNN]Ru(CH₂), the *cis,trans*-[NNN]"Ru(CH₂)PMe₃ conformer (phosphine trans to the [NNN] pyridine) is stable. This stable conformation was observed with both [NNN]' and [NNN]" ligands. The 14-VE *trans*-[NNN]Ru(CH₂) conformer leads to one 16-VE complex, *trans,cis*-[NNN]Ru(CH₂)PMe₃. However, only [NNN]' ligand produced a stable *trans,cis*-[NNN]'Ru(CH₂)PMe₃ conformation. The *cis,trans*-[NNN]'Ru(CH₂)PMe₃ conformer is also more energetically favorable than the *trans,cis*-[NNN]"Ru(CH₂)PMe₃ by 20.5 kcal/mol (Figure 2.7).

The results indicate that the position of the methyldene has a strong influence on the energy of the conformer. Both the 14-VE *cis*-[NNN]Ru(CH₂) and 16-VE *cis,trans*-[NNN]Ru(CH₂)PMe₃ complexes favor the methyldene in the cis-orientation with respect to the pyridine nitrogen of the [NNN] ligand. The type of [NNN] ligand also plays a role in the stability of [NNN]Ru(CH₂)PMe₃ complex. Complex [NNN]"Ru(CH₂)PMe₃



Scheme 2.6: Possible conformations of 16-VE $[NNN]Ru(CH_2)PMe_3$ complexes from the 14-VE conformers.

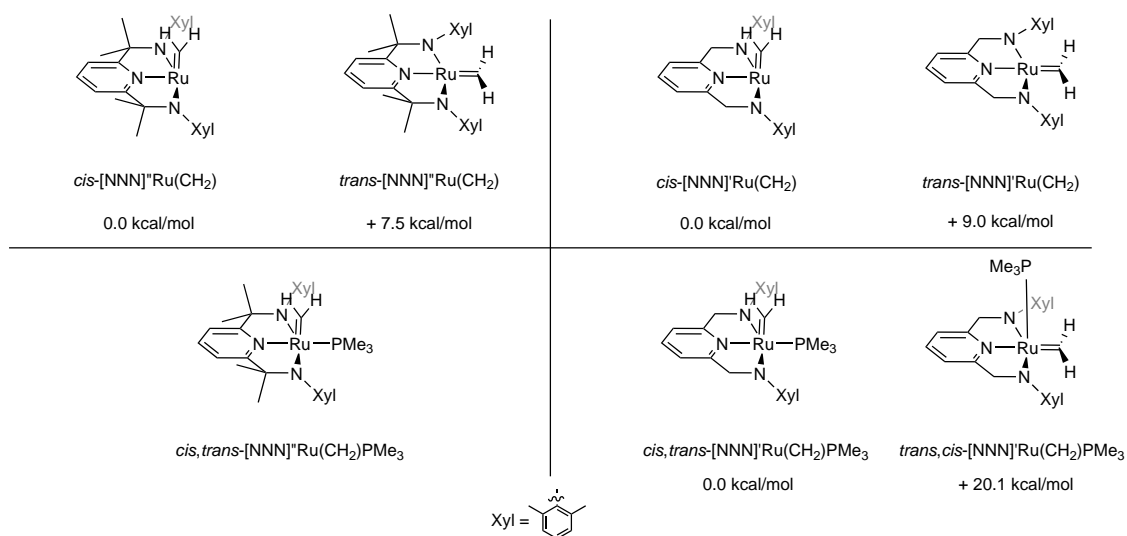


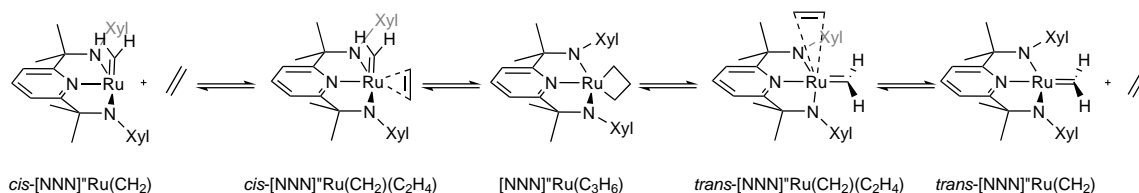
Figure 2.7: Stable conformations of $[NNN]Ru(CH_2)$ and $[NNN]Ru(CH_2)PMe_3$ complexes based on DFT calculations.

does not form a stable $trans,cis-[NNN]Ru(CH_2)PMe_3$ conformation as observed in the

$[NNN]Ru(CH_2)PMe_3$ complex. The isopropyl linkage groups of $[NNN]$ ligand increased

the steric bulk of the complex and impeded coordination of the PMe_3 ligand in the trans orientation.

Coordination of ethylene to $[\text{NNN}]\text{Ru}(\text{CH}_2)$ complex was investigated to map the energy diagram of the olefin metathesis cycle. The starting conformation $[\text{NNN}]\text{Ru}(\text{CH}_2)$ has little impact on the conclusions of this analysis because the $[\text{NNN}]\text{Ru}(\text{CH}_2)$ conformation exchanges between cis- and trans-conformers with each olefin metathesis cycle (Scheme 2.7). It is important to mention that geometry optimization calculations were computed on the cis and trans conformers with a molecule of ethylene. This allows for a direct energy comparison between the two conformers and the olefin metathesis intermediates. The energy difference between the cis and trans conformers in this computation is 11.2 kcal/mol, larger than the previous computation by 3.7 kcal/mol. The discrepancy is presumably due to presence of ethylene molecule during the calculation.



Scheme 2.7: Conformational exchange of $\text{cis-}[\text{NNN}]\text{Ru}(\text{CH}_2)$ and $\text{trans-}[\text{NNN}]\text{Ru}(\text{CH}_2)$ after one olefin metathesis cycle.

Ethylene coordination to $\text{cis-}[\text{NNN}]\text{Ru}(\text{CH}_2)$ to form $\text{cis-}[\text{NNN}]\text{Ru}(\text{CH}_2)(\text{C}_2\text{H}_4)$ was highly favored by -18.4 kcal/mol (Figure 2.8). The metallacyclobutane intermediate

([NNN]Ru(C₃H₆)) was slightly more stable than the *cis*-[NNN]Ru(CH₂) at by 4.9 kcal/mol. It is important to mention that in the ethylene adduct, the orientation of the Ru=CH₂ π-bond is orthogonal to the C₂H₄ π-bond forming a 96° H-C-Ru-N_{amido} dihedral angle (the =CH₂ adopts orientation **A**). Formation of the metallacyclobutane [NNN]Ru(C₃H₆) requires π – π stacking interaction between Ru=CH and C₂H₄. Thus, Ru=CH₂ must rotate by approximately 90° to allow for π – π stacking interaction and initiate the formation of [NNN]Ru(C₃H₆). Geometry optimization of [NNN]Ru(CH₂)(C₂H₄), in which Ru=CH₂ was rotated by approximately 90° (H-C-Ru-N_{amido} = 0°), led to the metallacyclobutane [NNN]Ru(C₃H₆) intermediate. The [NNN]Ru(C₃H₆) intermediate can collapse to form a more energetic *trans*-[NNN]Ru(CH₂) conformer (ΔE = 16.1 kcal/mol) releasing an ethylene molecule (Figure 2.8).

In the *trans*-[NNN]Ru(CH₂) conformer, the =CH₂ group adopted orientation **B**, and thus π-interactions between the Ru=CH₂ moiety and the incoming olefin can develop immediately. Addition of an ethylene molecule to the *trans* conformer forms a *trans*-[NNN]Ru(CH₂)(C₂H₄) adduct that immediately reacts to produce the [NNN]Ru(C₃H₆) intermediate. Formation of [NNN]Ru(C₃H₆) intermediate from the *cis* conformer was an exothermic process by 4.9 kcal/mol, while the same reaction from *trans* the conformer was an exothermic process by 16.1 kcal/mol.

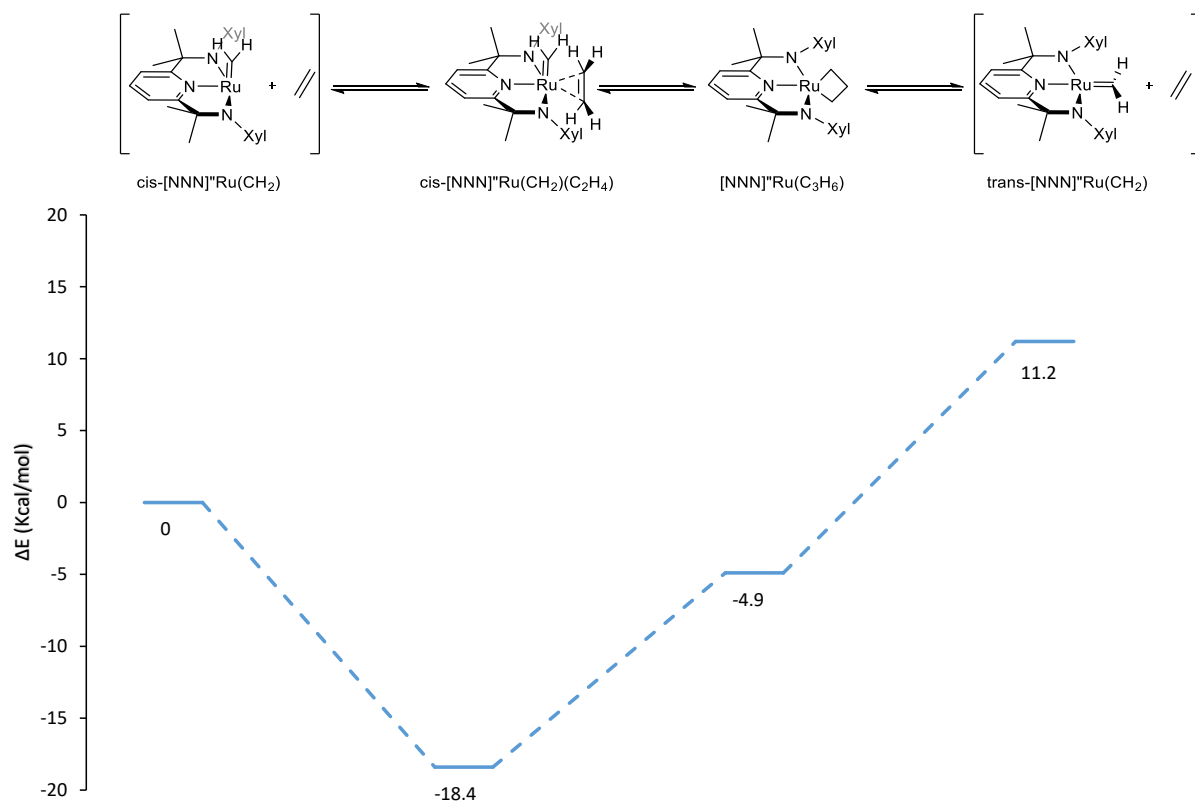


Figure 2.8: Energy diagram of the intermediates in olefin metathesis cycle.

While no energy barriers were in fact calculated, DFT computations suggest that bis(amido)pyridine ruthenium alkylidenes are viable candidates to catalyze olefin metathesis. Conformational analysis of $[\text{NNN}]\text{Ru}(\text{CH}_2)$ complex with either $[\text{NNN}]'$ or $[\text{NNN}]''$ ligand demonstrated that there are two stable conformers, *cis*- $[\text{NNN}]\text{Ru}(\text{CH}_2)$ and *trans*- $[\text{NNN}]\text{Ru}(\text{CH}_2)$, which is the more stable conformer by an average of 8 kcal/mol. Furthermore, both *cis*- and *trans*- $[\text{NNN}]''\text{Ru}(\text{CH}_2)$ conformers energetically favor the formation of the metallacyclobutane intermediate in the presence of an ethylene molecule given the required π -bond symmetry.

2.3 Conclusion and Future Remarks

DFT calculations showed that bis(amido)pyridine ruthenium methylenes in the presence of ethylene energetically favor the formation of the metallacyclobutane, a critical intermediate in the olefin metathesis cycle. Both *cis*-[NNN]Ru(CH₂) and *trans*-[NNN]Ru(CH₂) formed the metallacyclobutane intermediate upon ethylene coordination and alignment of Ru=CH₂ and C₂H₄ π -bonds. Experimentally, coordination of [NNN]²⁻ or H₂[NNN] to Ru(II) could not be achieved. Transmetalation of alkali/alkaline-earth metal of [NNN]²⁻ to ruthenium(II) complexes produced several, mostly unidentified products. Efforts to produce [NNN]RuL complex from reactions between the protio-ligand and amido or organoruthenium(II) precursors were also not successful. While there are many examples in the literature of complexes containing Ru(II)-amido moieties,⁶⁵⁻⁶⁷ there are only two reports of diamido-Ru(II) complexes and the amido groups in these complexes are *cis* with respect to each other.^{68,69} Investigations of the Ru-N bond stability and reactivity is critical to continue working on [NNN]Ru-type complexes. Future work can focus on the coordination chemistry of monodentate amide ligands such as diphenyl amide and bis(*t*-butyl)amide to Ru(II) precursors. Research can also be aimed at investigating the role of metal size (Fe, Os) and *d*-configuration (Re, Rh, Pd, Pt) on the

coordination chemistry of bis(amido)pyridines and the reactivity of corresponding complexes. These complexes can find applications in areas such as small molecule activation, hydrogenation, and hydrosilylation.^{70,71} The next chapter starts this work by looking into the coordination chemistry of [NNN]²⁻ to cobalt(III).

2.4 Experimental

General Considerations

The experiment procedures presented herein include those that resulted in the isolation of pure materials and those that did not from reactions discussed earlier. Reaction products were fully characterized by NMR spectroscopy whenever possible.

All manipulations were performed under argon using standard Schlenk line techniques or in a nitrogen-filled atmosphere MBraun glovebox. All glassware and cannula were dried at 160 °C for at least 12 h prior to use. All solvents used were dried using an MBraun solvent purification system fitted with alumina columns and stored over molecular sieves under argon. Deuterated NMR solvents were purchased from Sigma-Aldrich, degassed using three freeze-pump-thaw cycles, vacuum distilled from sodium (C_6D_6) and CaH_2 ($CDCl_3$ and CD_2Cl_2), and stored under argon. NMR spectra were recorded on a Bruker AV 400 or Bruker AV 300 spectrometer and at room temperature. $H_2[NNN]'$,⁸ $H_2[NNN]''$,⁷ $Mg(CH_3)_2$,⁷² $Mg(CH_3)_2$ TMEDA,⁷³ $RuCl_2(PPh_3)_3$,⁷⁴ $RuCl_2(PPh_3)_2(py)_2$,⁷⁵ $[RuCl_2(COD)]_n$ ⁷⁶ were synthesized using literature procedures. n -BuLi and $LiCH_2SiMe_3$ were titrated using methanol as titrant and phenanthroline as indicator.⁷⁷ KHMDS and $[RuCl_2(p\text{-cymene})]_2$ were purchased from Sigma-Aldrich and used as received.

Synthesis of [NNN]”Mg(THF)₂

A 5 ml THF solution of (CH₃)₂MgTMEDA (43 mg, 0.25 mmol) was added to a 5 ml THF solution of H₂[NNN]” (50 mg, 0.13 mmol) at room temperature resulting in a color change from yellow to red with effervescence. After allowing the mixture to stir for 20 minutes, THF was evaporated under vacuum and the product was extracted with pentane. The pentane solution was dried under vacuum to yield an orange solid. Yield: 68 mg (97% at 98% purity). ¹H NMR (C₆D₆, 400 MHz, 298 K) δ 7.42 (m, 3H, CH_{pyridine}), 6.99-6.90 (m, 6H, CH_{xylyl}), 3.21 (broad t, 8H, THF α-CH₂), 2.42 (s, 12H, CH_{3xylyl}), 1.53 (s, 12H, C(CH₃)₂), 1.02 (broad t, 8H, THF β-CH₂). [NNN]”MgTMEDA can be prepared in toluene using the same procedure.

Reaction of RuCl₂(PPh₃)₃ with [NNN]”Mg(THF)₂

A 3 ml toluene solution of [NNN]”Mg(THF)₂ (10 mg, 0.020 mmol) was added to a 5 ml toluene suspension of RuCl₂(PPh₃)₃ (17 mg, 0.020 mmol) and stirred at room temperature for 1.5 h. Toluene was evaporated, and the residue was washed with pentane and ether

and dried under vacuum. ^1H NMR (C_6D_6 , 300 MHz, 298 K) δ 7.90 (broad, 1.1H), 7.75 (broad, 1.8H), 7.64 (broad s, 2.6, *o*-CH of $\text{RuCl}_2(\text{PPh}_3)_3$), 7.41 (s, 2.2H, *o*-CH of PPh_3), 6.88-6.83 (m, 13H), 2.77 (broad s, 0.9H), 2.30 (s, 0.4H), 2.12 (s, 0.9H), 2.07 (s, 1.1H), 1.81 (s, 1H), 1.50 (s, 1.81H), 1.38 (broad, 2.8). ^{31}P NMR (C_6D_6 , 298 K) δ 53.6, 47.8, 45.6, 45.1, -5.04 (PPh_3).

Synthesis of $[\text{NNN}]\text{Mg}(\text{py})_2$

A 5 ml toluene mixture of $\text{H}_2[\text{NNN}]$ (100 mg, 0.251 mmol) and pyridine (101 μL , 1.25 mmol) was added dropwise to a 3 ml toluene suspension of $\text{Mg}(\text{CH}_3)_2$ (25 mg, 0.46 mmol) producing a clear red solution within 10 minutes. The solvent was evaporated and the product was extracted using pentane. The solvent was evaporated in vacuo to give an orange solid. Yield: 91 mg (62%). ^1H NMR (C_6D_6 , 300 MHz, 298 K) δ 8.04 (broad s, 4H, *o*- CH_{py}), 7.28 (t, $^3J = 7.6$ Hz, 1H, CH), 7.13 (d, $^3J = 7.6$ Hz, 4H, *m*- CH_{xylyl}), 7.08 (d, $^3J = 7.5$ Hz, 2H, CH), 6.88 (t, $^3J = 7.5$ Hz, 2H, *p*-xylyl), 6.73 (t, 2 H, *p*- CH_{py}), 6.37 (t, 4H, $^3J = 7.3$ Hz, *m*- CH_{py}), 2.34 (s, 12H, $\text{CH}_{3\text{xylyl}}$), 1.56 (s, 12H, $\text{C}(\text{CH}_3)_2$).

Reaction of $\text{Li}_2[\text{NNN}]''$ with $\text{RuCl}_2(\text{PPh}_3)_2(\text{py})_2$

To a 3 ml THF solution of $\text{H}_2[\text{NNN}]''$ (50.0 mg, 0.125 mmol) chilled to $-80\text{ }^\circ\text{C}$ was added n-BuLi (2.5 M in hexanes, $100\mu\text{L}$, 0.250 mmol), causing an immediate color change from yellow to orange. The mixture was stirred for 5 minutes. A pre-chilled THF solution of $\text{RuCl}_2(\text{PPh}_3)_2\text{py}_2$ (107 mg, 0.125 mmol) and pyridine ($50.0\ \mu\text{L}$, 0.625 mmol) was added to the $\text{Li}_2[\text{NNN}]'$ solution and stirred cold for 45 minutes. While warming up the reaction mixture to room temperature, the color changed from murky orange to black. The mixture was dried under vacuum. ^1H NMR (C_6D_6 , 300 MHz, 298 K) δ 9.21 (broad d, 1.0H, py of $\text{RuCl}_2(\text{PPh}_3)_2\text{py}_2$), 7.83 (broad s, 3.3H, PPh_3 of $\text{RuCl}_2(\text{PPh}_3)_2\text{py}_2$), 7.40 (m, 0.4H, PPh_3), 7.24 (m, 0.4H), 7.02-6.84 (m, 7.7H, PPh_3 and $\text{H}_2[\text{NNN}]''$), 6.68 (broad t, 0.4H, py of $\text{RuCl}_2(\text{PPh}_3)_2\text{py}_2$), 6.12 (broad t, 1H, py of $\text{RuCl}_2(\text{PPh}_3)_2\text{py}_2$), 4.02 (s, 0.2H, $\text{H}_2[\text{NNN}]''$), 2.08 (s, 1.6H, $\text{H}_2[\text{NNN}]''$), 1.47 (s, 1.7H, $\text{H}_2[\text{NNN}]''$).

Reaction of $[\text{Ru}(\text{HMDS})]_2$ with $\text{H}_2[\text{NNN}]''$

A 3 ml toluene solution of KHMDS (50 mg, 0.25 mmol) at $-78\text{ }^\circ\text{C}$ was added to a 7 ml THF solution of $\text{RuCl}_2(\text{PPh}_3)_3$ (119 mg, 0.125 mmol) at $-78\text{ }^\circ\text{C}$ and stirred for 40 minutes. A 5 ml toluene solution of $\text{H}_2[\text{NNN}]''$ (50 mg, 0.13 mmol) chilled to $-78\text{ }^\circ\text{C}$ was then added and the reaction mixture was allowed to slowly warm up to room temperature. An aliquot

of the reaction mixture was dried under vacuum and analyzed by NMR spectroscopy.

^1H NMR (C_6D_6 , 300 MHz, 298 K) δ 7.87 (broad, 2.4H), 7.54 (broad s, 2.1H, *o*-PPh₃ of RuCl₂(PPh₃)₃), 7.40 (broad s, 4.1H, PPh₃), 7.24 (s, 1.7H), 7.03-6.81 (m, 15.3H, PPh₃ and H₂[NNN]”), 4.02 (s, 1H, H₂[NNN]”), 2.07 (s, 6.7H, H₂[NNN]”), 1.37 (s, 6.1H, H₂[NNN]”).

^{31}P NMR (C_6D_6 , 298 K) δ 27.1, 26.5, -5.11 (s, PPh₃).

Reaction of [Ru(CH₃SiMe₃)]₂ with H₂[NNN]”

To a cold (-78 °C) 7 ml toluene suspension of RuCl₂(PPh₃)₃ (119 mg, 0.125 mmol) was added LiCH₂SiMe₃ (2 M in pentane, 130 μL , 0.260 mmol) and mixture was stirred cold for 40-60 minutes. A 5 ml toluene solution of H₂[NNN]” (50.0 mg, 0.125 mmol) chilled to -78 °C was then added and the reaction mixture was allowed to warm up slowly to room temperature. The reaction mixture was filtered, solvent evaporated and an NMR spectrum acquired. ^1H NMR (C_6D_6 , 300 MHz, 298 K) δ 7.65 (broad t, 16.2H, *o*-PPh₃ of RuCl₂(PPh₃)₃), 7.40 (broad t, 7.4H, PPh₃), 7.25(broad, 4.25H, H₂[NNN]”) 7.04-6.84 (m, 50H, PPh₃, and H₂[NNN]”), 4.02 (s, 2H, H₂[NNN]”), 2.3(s, 1H), 2.13 (s, 2.5H), 2.08 (s, 12.6H, H₂[NNN]”), 1.82 (s, 3.0H), 1.51 (s, 3.8H), 1.47 (s, 13.7H₂[NNN]”).

Reaction of $\text{RuCl}_2(\text{PPh}_3)_3$ with $\text{H}_2[\text{NNN}]''$

A mixture of $\text{H}_2[\text{NNN}]''$ (79 mg, 0.20 mmol) and $\text{RuCl}_2(\text{PPh}_3)_3$ (178 mg, 0.188 mmol) in 15-20 ml methanol was refluxed overnight. The reaction mixture was cooled to room temperature, the supernatant was decanted from the pink solids. The supernatant was then dried in vacuo to yield a residue that was analyzed by NMR spectroscopy. Yield 92 mg. ^1H NMR (C_6D_6 , 300 MHz, 298 K) δ 7.65 (broad s, 1H, *o*- PPh_3 of $\text{RuCl}_2(\text{PPh}_3)_3$), 7.40 (broad s, 2.8H *o*- PPh_3), 7.25 (m, 2.7), 7.00-6.84 (m, 16.4H), 4.12 (broad, 2.4), 2.17 (s, 5.6H), 2.09 (s), 2.08 (s, $\text{H}_2[\text{NNN}]''$), 1.64 (s, 5.53H), 1.60 (s, 5.1H) 1.47 (s, 7.5H, $\text{H}_2[\text{NNN}]''$).

Computational Details

DFT Calculations in the gas phase were carried out using Gaussian 09 on the Shared Hierarchical Academic Research Computing Network (SHARCNET: www.sharcnet.ca). Geometry optimizations were performed at the B3LYP hybrid level of theory with the split basis set (LACVP**) where Ru atom was described with LANL2DZ and other atoms with 6-31G(d,p). Solvent corrections were modeled using the Polarizable Continuum Model (PCM) for DCM. Energy calculations were performed using the M06 functional using the split basis set (LACVP++**(2f)) where Ru atom is described with LANL2DZ,

and other atoms with 6-311++G(2df,p) at M06 functional.

Chapter 3

Cobalt-based Polymerization

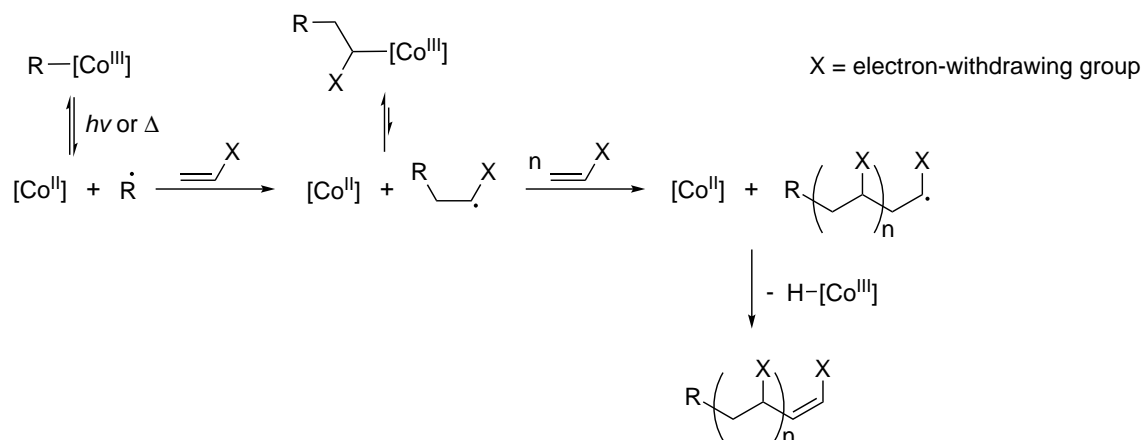
Catalysts

Part of the work presented herein is published in *Dalton Transactions*

(*Dalton Trans.*, 2017, **46**, 16228-16235. DOI: 10.1039/c7dt03674d; manuscript accepted on November 2, 2017)

3.1 Introduction

Cobalt has been instrumental to the development of modern coordination chemistry. Concepts of oxidation state and coordination number were first described by Alfred Werner using hexaamine Co(III) complexes.⁷⁸ Ligand substitution mechanisms were explained by Henry Taube using known coordination chemistry of various metals including Co(III) complexes.⁷⁸ Catalysts with cobalt metal centers are used industrially in hydroformylation of olefins to yield aldehydes or alcohols,⁷⁹ and in the Fischer-Tropsch process to produce hydrocarbons from CO and H₂.⁸⁰



Scheme 3.1: General mechanism of cobalt-mediated radical polymerization.

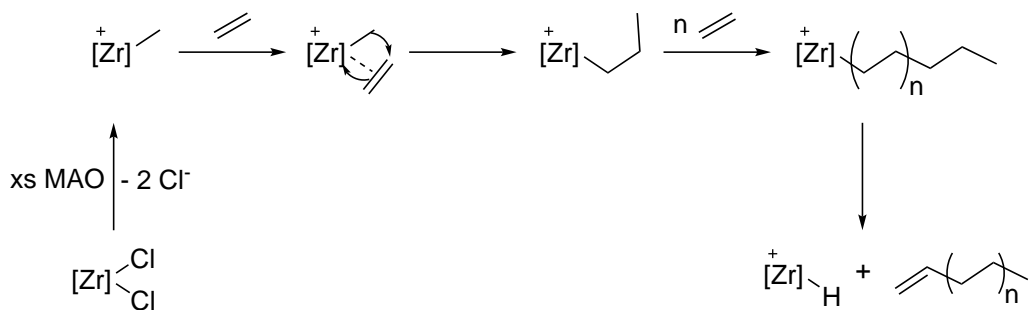
In polymerization chemistry, cobalt-based catalysts are involved in two areas: cobalt-mediated radical polymerization (CMRP) and coordination polymerization of alkenes. CMRP relies on the persistent radical effect of Co(II) from homolysis of the Co(III)–C

bond to control the radical polymerization. Co(III)–C bonds are weak and can homolytically cleave to Co(II) and alkyl radicals thermally or photochemically (Scheme 3.1). Standard radical-based polymerization then proceeds in which the radical monomer reacts with another monomer. Radical concentrations during the polymerization remains low due to rapid recombination with Co(II), which also minimizes termination of the growing polymer chain by radical coupling. The preferred chain termination occurs by β -hydrogen elimination to form Co(III)–H with release of the alkene-terminated polymer. CMRP has been applied to control the radical polymerization of four monomer groups: acrylic esters, acrylic acid, vinyl esters, and acrylonitriles.⁸¹ The next sections will discuss the role of cobalt in *coordination* polymerization of alkenes.

3.2 Coordination Polymerization of Alkenes

Polyethylene is the material of choice for many applications such as medical implants, devices, infrastructure materials, and food packaging. The commercial synthesis of polyethylene (PE) and its different grades (including linear low-density polyethylene, LLDPE) is principally based on heterogeneous Ti-based Ziegler-Natta catalyst or homogeneous metallocene catalysts of early transition metals.⁸² The polymerization mechanism, in the presence of methylaluminoxane (MAO) co-catalyst, starts by coordination

of ethylene into an open coordination site of the catalyst followed by migratory insertion of the alkyl group into the ethylene. The polymer chain grows by two carbons units and opens a coordination site for another ethylene molecule (Scheme 3.2). The growing polymer chain is susceptible to several chain transfer reactions. For example, β -hydrogen transfer to coordinated ethylene or the metal center terminates polymer growth.



Scheme 3.2: General mechanism of metallocene polymerization catalysts.

The physical properties of polyethylenes are dependent on the composition and the microstructure of the polymer chain. Linear low-density polyethylene is produced from copolymerization of ethylene and 1-alkene, while high-density polyethylene is produced from homo-polymerization of ethylene itself under condition that prevents the formation of radicals. With prochiral monomers such as propylene, polymerization can produce polymers with different stereochemical configurations. The two main classes of stereoregular configurations of these polymers are syndiotactic and isotactic (Figure 3.1). Syndiotactic PP has an alternating orientation of the methyl groups, while isotactic PP

has the same orientation for all methyl groups. In contrast, atactic polypropylene (PP) has a random orientation of the methyl groups. Atactic PP polymer is an amorphous material, while syndiotactic and isotactic PP polymers are semi-crystalline with melting points of 30 °C and 165 °C respectively.⁸³

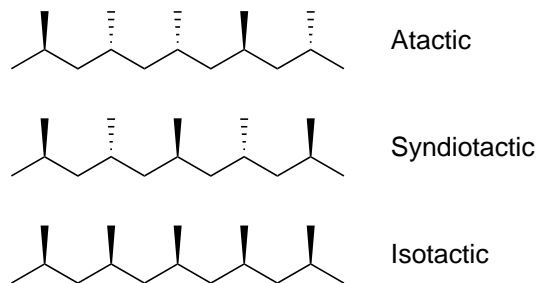
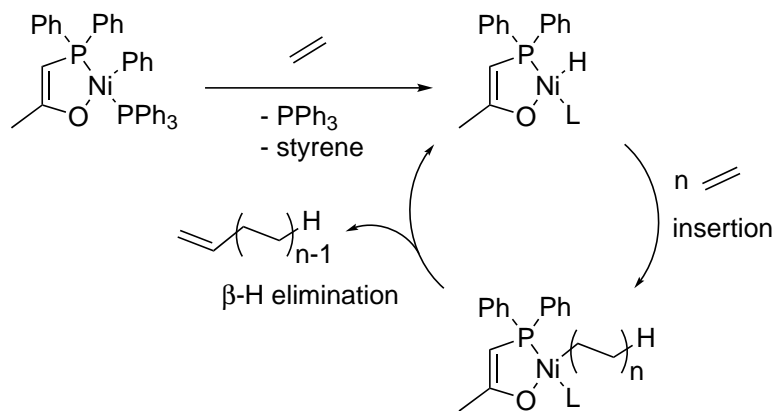


Figure 3.1: Polypropylene showing three different stereochemical configurations.

3.2.1 Bis(imino)pyridine-supported Cobalt(II) Catalysts for Olefin Polymerization

A major shortcoming of polymerization catalysts based on early transition metals is that the metal centers are oxophilic and thus are highly sensitive to polar functional groups. The polymerization scope of these catalysts is limited to non-polar monomers in non-polar solvents under water-free conditions. Research for late transition metal catalysts was essential to expand the scope of homogeneous olefin polymerization. One of the first late-transition metal polymerization catalysts was reported by Keim in 1978.⁸⁴ The

catalyst was based on a square planar phenyl Ni(II) complex supported by a phosphine-based bidentate ligand and PPh₃. The catalyst could only oligomerize ethylene to linear α -olefins due to rapid β -hydrogen elimination (Scheme 3.3). The process was commercialized under the name Shell Higher Olefin Process (SHOP) with an annual global production of low molecular weight oligomers of over one million tonnes.⁸⁴



Scheme 3.3: Oligomerization of ethylene using the SHOP catalyst.

In 1995, Brookhart reported Ni and Pd complexes supported by an α -diimine ligand that were highly active in ethylene and olefin polymerization. Since then, several other systems based on Co, Fe, Ni and Pd have been reported.⁸⁵ Related Co(II) and Fe(II) dihalide catalysts with bis(imino)pyridine as the spectator ligand ($[N_{imino}NN_{imino}]M(II)Cl_2$, $M = Fe, Co$) were particularly interesting (Figure 3.2). These systems achieved very high activity upon activation by methylaluminoxane (MAO) ($> 10^5$ g mmol⁻¹ h⁻¹ bar⁻¹ for Fe systems). The sterics on the aryl groups of $[N_{imino}NN_{imino}]$ in these systems influenced

the catalytic activity and the molecular weight of the polymer. Catalysts with bulky aryl groups produced HDPE, while catalysts with smaller substituents formed highly linear α -olefins.⁸⁶

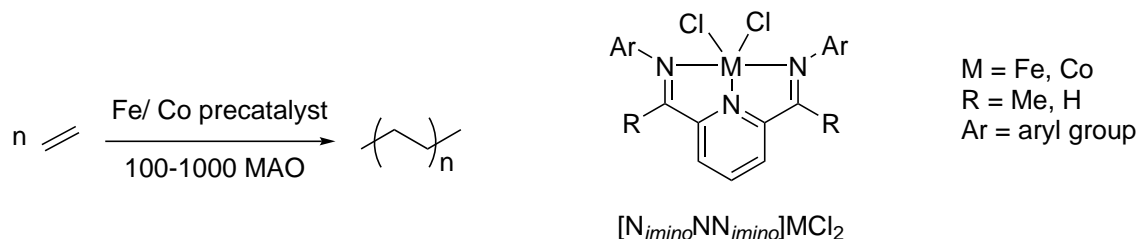
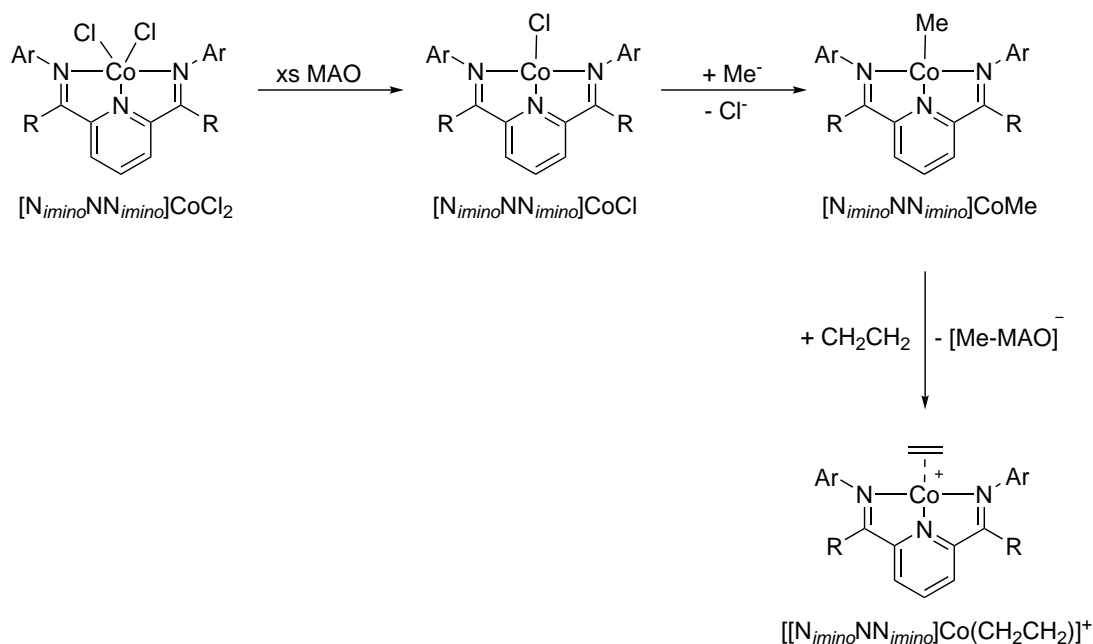


Figure 3.2: Bis(imino)pyridine supported Fe and Co precatalysts.

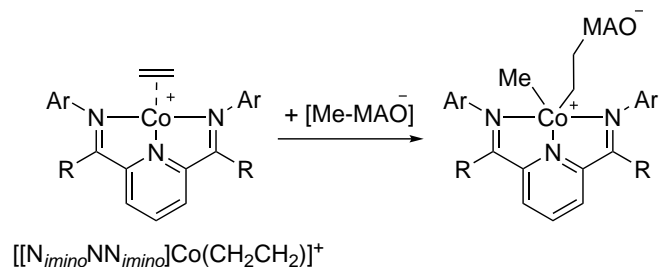
The polymerization mechanism of $[N_{imino}NN_{imino}]Co(II)Cl_2$ differ from metallocene catalysts. In the latter system, a mixture of zirconocene dihalide and MAO (MAO:Zr ratio $\geq 1000:1$) produce a catalytically active cationic methyl zirconocene complex.^{87,88} In $[N_{imino}NN_{imino}]Co(II)Cl_2$ precatalyst, Co(II) dihalide is reduced by MAO (MAO:Co ratio 100-1000:1) to $[N_{imino}NN_{imino}]Co(I)Cl$ and then converted to $[N_{imino}NN_{imino}]Co(I)Me$ complex (Scheme 3.4). Interestingly, the cobalt(I) methyl complex is not catalytically active in the absence of MAO. The methyl group is abstracted by MAO to form a non-coordinating $[Me-MAO]^-$ anion and $[N_{imino}NN_{imino}]Co(I)$ cation (Scheme 3.4). Ethylene coordination to the cationic $[N_{imino}N_{imino}]Co(I)$, forming the $[N_{imino}NN_{imino}]Co(I)$ ethylene adduct, is considered to be the immediate precursor to the catalytically active species.^{89,90} Due to the high MAO/precatalyst ratio required to activate the cata-

lyst,^{90,91} the identity of the catalytically active species and the polymerization mechanism are not understood. Polymerization is postulated to proceed through a Co(I) or a Co(III) species. Gibson reported a study in support of the Co(III) species through deuterium labeling studies of the cobalt precatalyst and the activator. The initiation step of $[[N_{imino}NN_{imino}]Co(I)(CH_2CH_2)]^+$ was postulated to produce Co(III) dialkyl zwitterionic complex (Scheme 3.5).⁹²



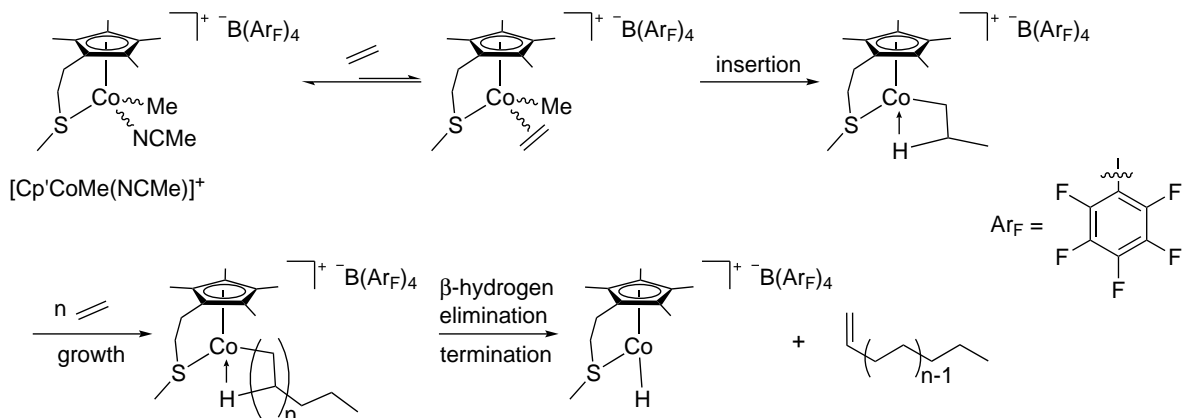
Scheme 3.4: Activation reactions of the bis(imino)pyridine Co(II) dihalide precatalyst with excess MAO to form the Co(I) ethylene adduct.

Organocobalt(III) has also been shown to be an active polymerization catalyst without addition of MAO co-catalyst.⁹³ Brookhart has shown that $[Cp'Co(III)Me(NCMe)]^+$ produced PE with similar molecular weight, and branching level as MMAO (modified



Scheme 3.5: Proposed initiation step of $[[N_{imino}NN_{imino}]Co(I)Me]^+$.

MAO) activated catalysts. The polymerization mechanism is proposed to proceed via alkyl insertion into the coordinated ethylene to produce a β -agostic complex as the resting state. Polymer chain can either grow in the presence of ethylene and terminate via β -hydrogen elimination (Scheme 3.6).



Scheme 3.6: Mechanism of Co(III)-based ethylene polymerization catalyst.

3.2.2 Bis(amido)pyridine Organocobalt Complexes

The motivation to pursue the synthesis of 2,6-bis(*amido*)pyridine organocobalt(III) complex $[NNN]CoR$ stems from its similarities to the catalytically active $[Cp'CoMe(NCMe)]^+$

complex and the $[N_{imino}NN_{imino}]Co(II)$ system. The $[NNN]CoR$ complex is based on a Co(III) center and contains an alkyl group similar to $[Cp'CoMe(NCMe)]^+$ complex. The Cp'^- ligand is limited in its electron-donation capacity of six-electrons and the possibility to tune its electronics and sterics. In contrast, $[NNN]^{2-}$ formally donates up to six-electrons with additional π -electron density available through two filled p -orbital of the amido groups. The synthetic procedure of the protio ligand $H_2[NNN]$ also allows for tuning of electronic and steric properties by varying the nature of the aniline fragment.

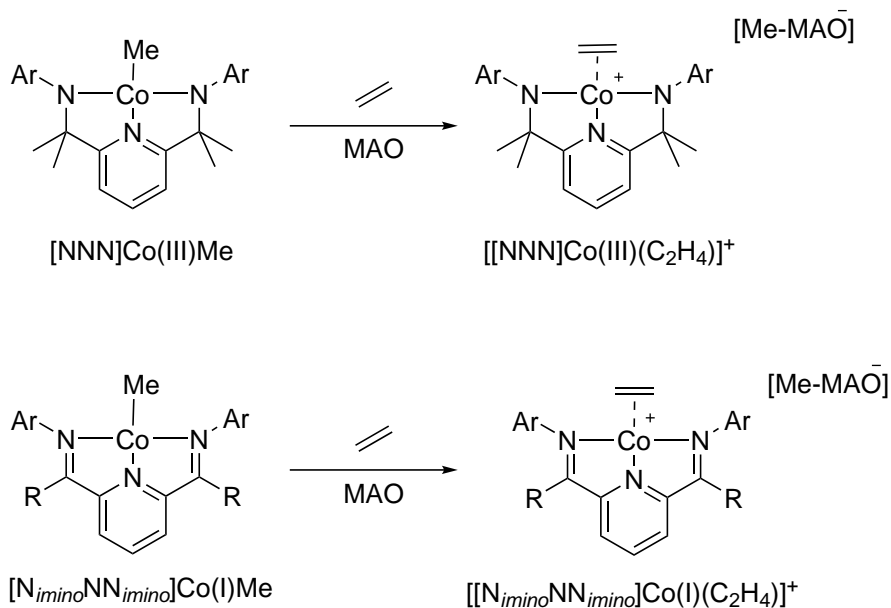


Figure 3.3: Proposed reactivity of $[NNN]Co(III)Me$ complex (top) with MAO closely mimics that of $[N_{imino}NN_{imino}]Co(I)Me$ (bottom) with MAO.

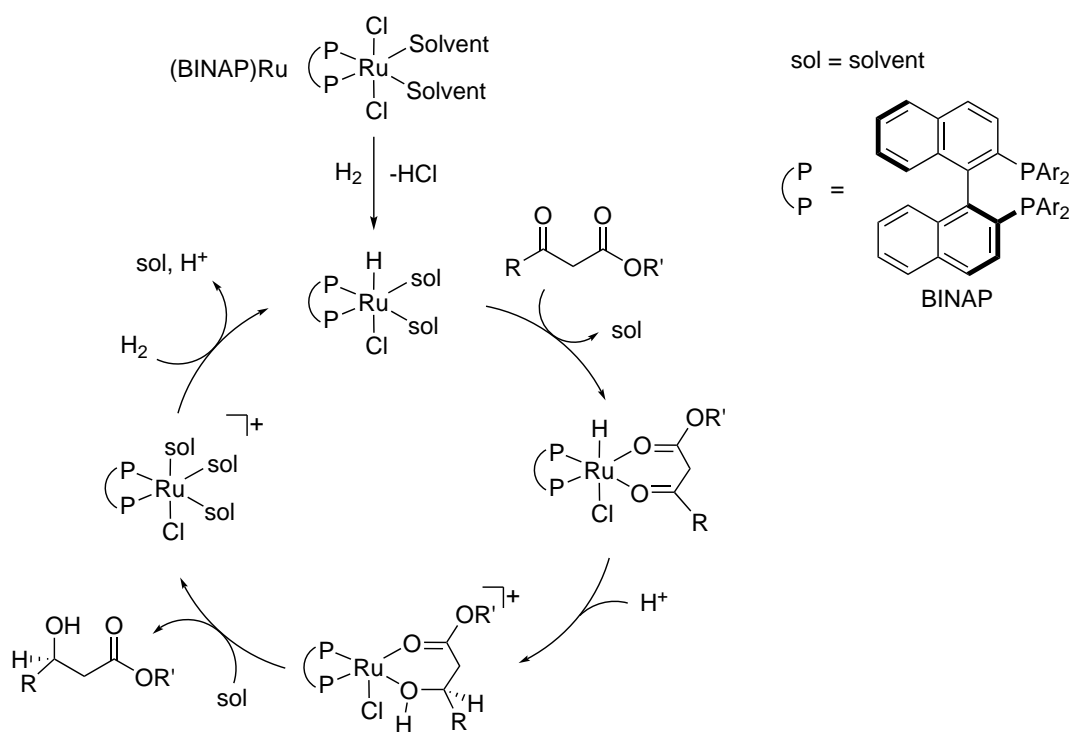
The $[NNN]CoR$ of interest mimics the $[N_{imino}NN_{imino}]CoCl_2$ system in several ways. In terms of the ligands, $[NNN]^{2-}$ is structurally similar to $[N_{imino}NN_{imino}]$ in that $[NNN]^{2-}$ coordinates to a metal in a meridional configuration where the amido nitrogen atoms

adopt an sp^2 hybridization. Similar to the reactivity of $[N_{imino}NN_{imino}]Co(I)Me$ with MAO, $[NNN]Co(III)Me$ can potentially react with MAO in the presence of ethylene to produce cationic $[[NNN]Co(III)(C_2H_4)]^+$ adduct, which mimics the geometry and charge of the cationic $[N_{imino}NN_{imino}]Co(I)(C_2H_4)$ adduct (Figure 3.3). The main difference between $[N_{imino}NN_{imino}]Co(I)Me$ and $[NNN]Co(III)Me$ is the location of two electrons. $[N_{imino}NN_{imino}]Co(I)Me$ complex has a d^8 -metal center that can π -backdonate electron density into the pyridine group and one of the two p -orbitals of the imino groups. In contrast, the $[NNN]Co(III)Me$ has a d^6 -metal center that can accept π -electron density from one of the two filled p -orbitals of the nitrogen atoms.

3.2.3 Beyond Olefin Polymerization

The $[NNN]Co(III)L^+$ complex is also a viable candidate as a hydrogenation catalyst of carbonyls and imines. Hydrogenation catalysts contain a M-H moiety that attacks the electrophilic carbon, reducing the substrate to the corresponding alcohol or amine. The Noyori group was the first to report asymmetric hydrogenation using (BINAP)Ru(II) dihalide catalysts.⁹⁴ The mechanisms of these catalysts are classified based on the transition state; either as an inner-sphere mechanism through a 4-membered transition state or as an outer-sphere mechanism through a 6-membered transition state. The (BINAP)Ru(II)

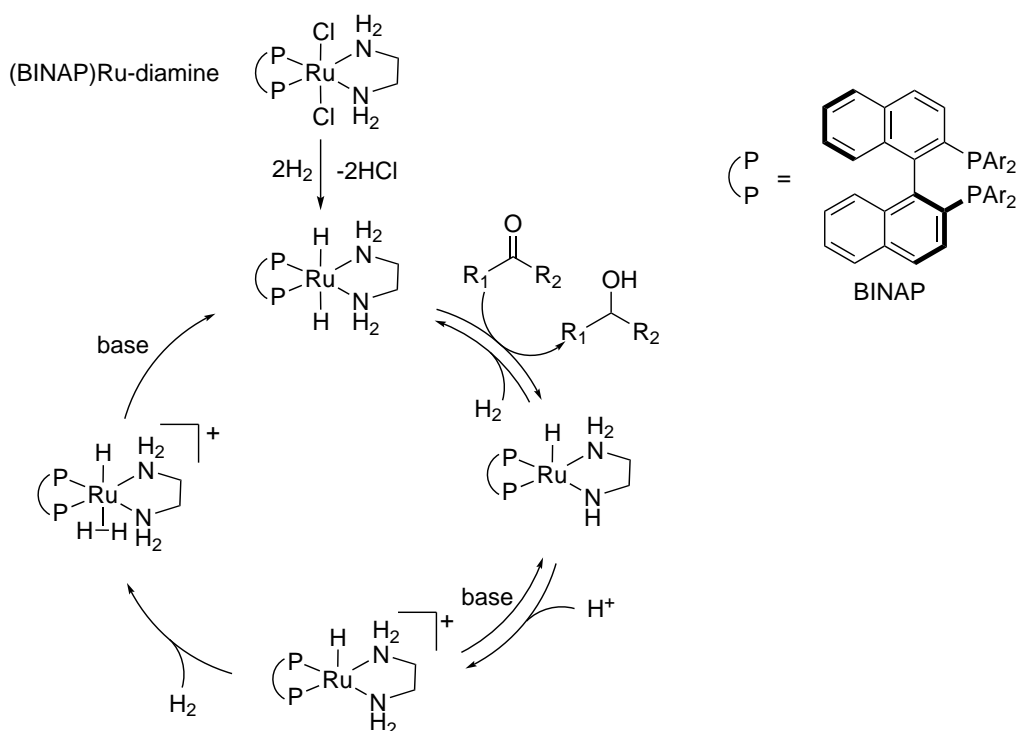
dihalide precatalyst hydrogenates functionalized carbonyls through an inner-sphere mechanism (Scheme 3.7). The Ru dihalide complex is activated with H₂ to produce the corresponding Ru hydride complex and HCl. The substrate coordinates to the Ru center and the carbonyl functionality is reduced under acidic conditions to the corresponding alcohol producing a cationic Ru complex. The Ru monohydride complex is regenerated from the cationic Ru complex by H₂ (Scheme 3.7).



Scheme 3.7: Inner-sphere asymmetric hydrogenation mechanism of functionalized ketones via a 4-membered transition state using (BINAP)Ru precatalyst.

The (BINAP)Ru diamine catalyst hydrogenates carbonyls through an outer-sphere mechanism in which the Ru-H acts as the hydride source and the amine supplies the proton (Scheme 3.8). The (BINAP)Ru diamine precatalyst is activated by H₂ to form a

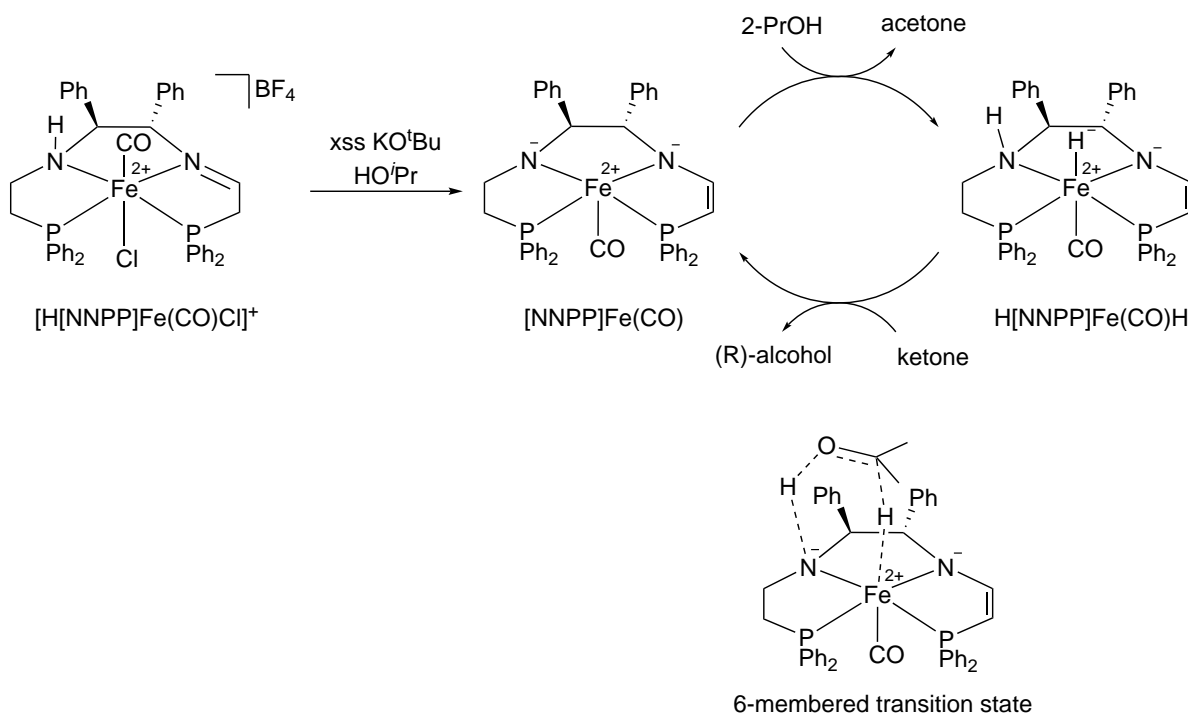
Ru-dihydride complex. The carbonyl substrate forms a 6-membered transition state in which the carbonyl carbon is associated with the Ru-H moiety and the carbonyl oxygen is associated with the N-H moiety. After product formation, the Ru-monohydride complex is converted back to the catalytically active Ru-dihydride complex using H_2 and a base (Scheme 3.8).



Scheme 3.8: Outer-sphere asymmetric hydrogenation mechanism of ketones via 6-membered transition state using (BINAP)Ru diamine precatalyst.

There is a need to develop hydrogenation catalysts based on first-row transition metals because they are more abundant, cheaper, and less toxic compared to the Ru-based systems. The Morris group has been successful in this area using an Fe(II) metal center supported by a tetradentate ligand which is an effective catalyst in asymmetric transfer

hydrogenation (Scheme 3.9).⁹⁵ This system used sacrificial alcohol to substitute H₂ for the source of the hydride and the proton. The mechanism of this system starts by activation of the [H[NNPP]Fe(CO)Cl]⁺ precatalyst in the presence of HOⁱPr with excess base. The base deprotonates [H[NNPP]Fe(CO)Cl]⁺ at two locations, the amine group and the β-carbon of the imine group, to form a neutral [NNPP]Fe(CO) complex containing two amido groups. The neutral [NNPP]Fe(CO) complex abstracts a hydride and a proton from the HOⁱPr to produce acetone and a catalytically-active H[NNPP]Fe(CO)H complex. This complex can stereoselectively convert a ketone substrate to an R-alcohol via the 6-membered transition state.



Scheme 3.9: Asymmetric transfer hydrogenation using iron(II) pincer precatalyst.

The $[[\text{NNN}]\text{CoL}]^+$ complex shares some similarities to the $[\text{NNPP}]\text{Fe}(\text{CO})$ complex. The $[[\text{NNN}]\text{CoL}]^+$ complex has a cobalt(III) metal center, which is isoelectronic with Fe(II), coordinated by two chelating amido functional groups, both attached to a central pyridine ring. It also mimics the geometrical features of $[\text{NNPP}]\text{Fe}(\text{CO})$ in that the metal-amido group lie in the meridional plane of the complex with two empty axial coordination sites.

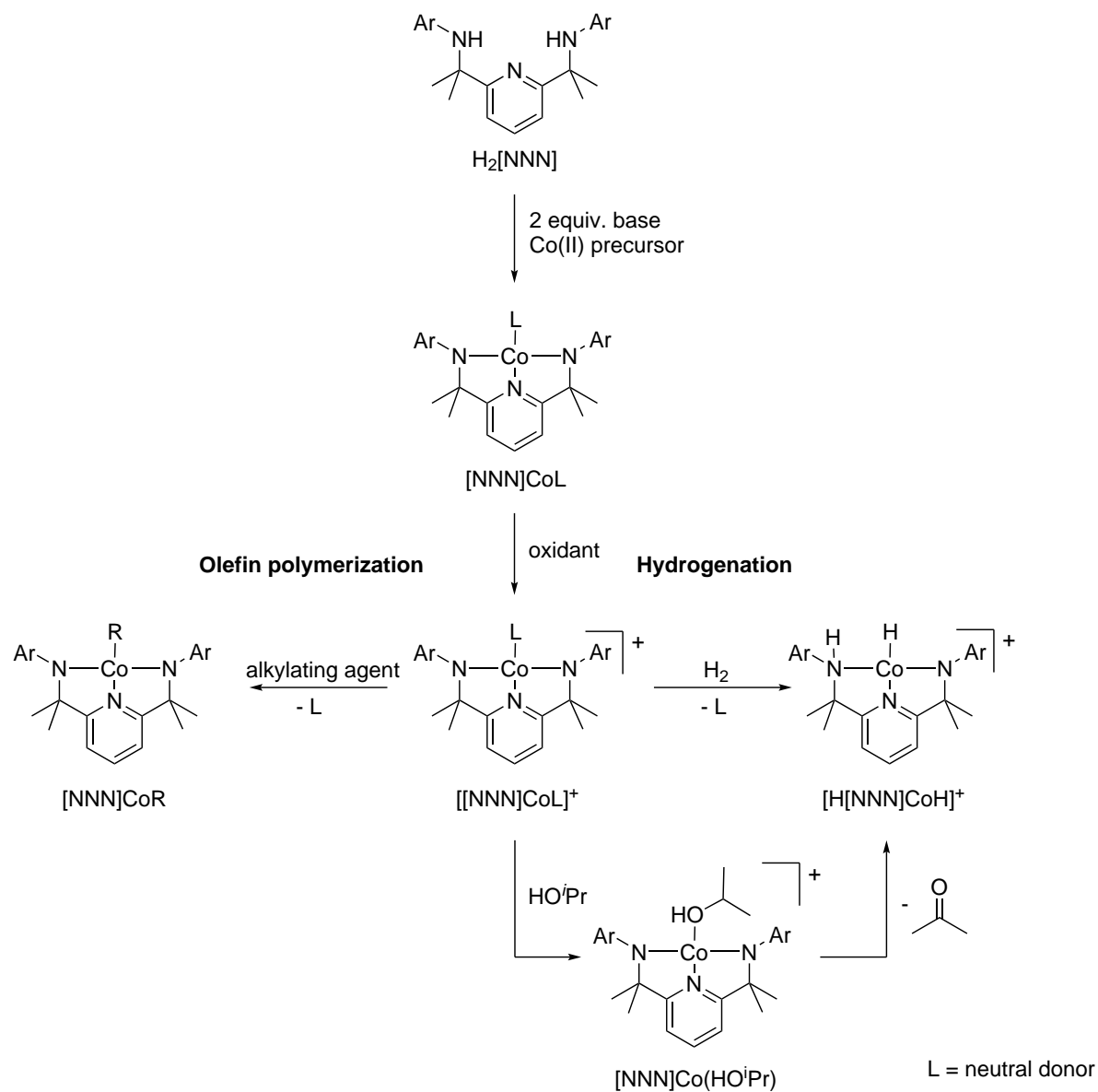
3.2.4 Research Plan for 2,6-bis(amido)pyridine Cobalt(III)

Complexes

The plan to synthesize bis(amido)pyridine supported cobalt(III) complexes $[[\text{NNN}]\text{CoL}]^+$ starts by coordination of the diamide ligand to a Co(II) precursor. The resultant neutral $[\text{NNN}]\text{Co}(\text{II})\text{L}$ complex can be oxidized by one electron to form a $[[\text{NNN}]\text{Co}(\text{III})\text{L}]^+$ complex. Similar reactions have been reported by Gordon⁶ and Lee⁹⁶ using analogous systems. These reactions were used as starting point to successfully develop the synthetic procedure of $[\text{NNN}]\text{Co}(\text{III})\text{py}$ complex (py = pyridine, see experimental section 3.5 below). For $[\text{NNN}]\text{CoR}$ (R = alkyl group) complexes aimed at olefin polymerization chemistry, introduction of an alkyl group to $[[\text{NNN}]\text{CoL}]^+$ complex was explored using a variety of alkylating reagents (Scheme 3.10). Although carbon-cobalt bonds are generally

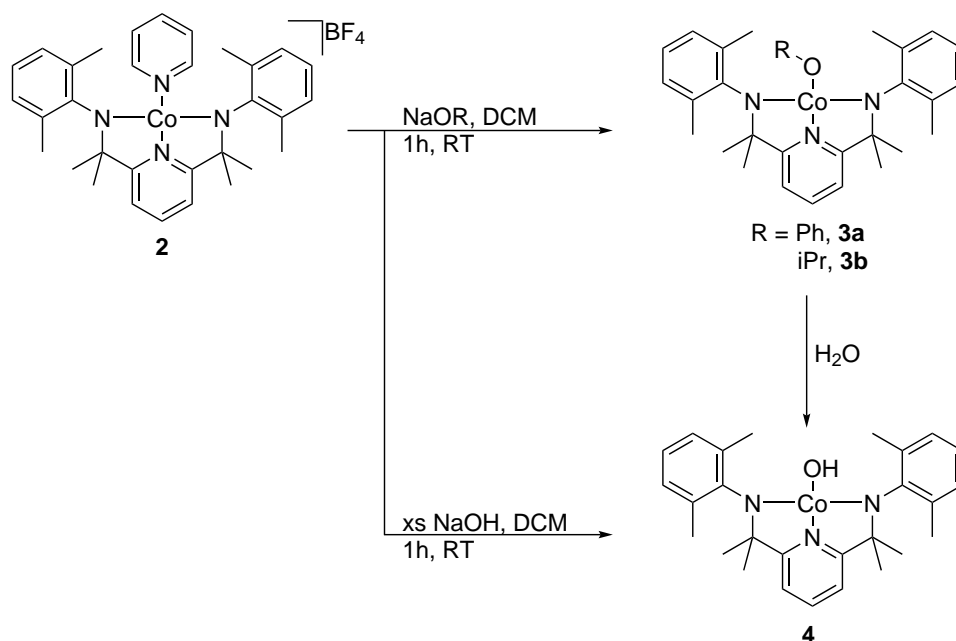
weak and prone to homolytic cleavage under UV-light,^{97,98} the stability of these bonds in complexes supported by amido groups have not been reported.

We predict that the strong π -donating ability of the bis(amido)pyridine can stabilize the Co-C single bond by increasing the electron density at Co(III) atom and the nucleophilicity of the carbon atom. The effect enhances Co-C ionic character and reduces its ability to undergo homolysis. For complexes aimed at hydrogenation chemistry, the reactivity of the $[[\text{NNN}]\text{CoL}]^+$ complex towards hydrogen and its propensity to undergo β -hydrogen elimination was investigated. Hydrogen can theoretically coordinate to the $[[\text{NNN}]\text{CoL}]^+$ complex and potentially react to produce $[\text{H}[\text{NNN}]\text{CoH}]^+$, which contains all the functional groups required for hydrogenation chemistry (Scheme 3.10). Furthermore, the ability of $[[\text{NNN}]\text{CoL}]^+$ to undergo β -hydrogen elimination can be explored by reactions with alcohols. For instance, reaction of $[[\text{NNN}]\text{CoL}]^+$ with HO^iPr can potentially produce $[\text{H}[\text{NNN}]\text{CoH}]^+$ complex.



Scheme 3.10: Chemical transformations of bis(amido)pyridine cobalt(III) complexes aimed at olefin polymerization and hydrogenation chemistry.

The synthesis of the corresponding neutral alkyl and hydride complexes was explored by reactions of **2** with metal alkyl and hydride reagents, such as AlMe_3 , $(\text{CH}_2\text{CHCH}_2)\text{MgCl}$, CH_3MgBr , $\text{LiCH}_2\text{Si}(\text{CH}_3)_3$, and $\text{LiHB}(\text{CH}_2\text{CH}_3)_3$. These reactions gave a reduced product, presumably through homolytic cleavage of the metal–hydrogen or metal–carbon bond in the new transiently-formed complex, resulting in a red paramagnetic complex, consistent with **1**-based spectroscopic data.^{99–102} This was further supported by the independent synthesis of complex **1** by the chemical reduction of **2** with KC_8 .



Scheme 3.12: Synthesis of Co(III) complexes **3** and **4**.

Reactions of **2** with sodium phenoxide and isopropoxide to produce coordination complexes $[\text{NNN}]\text{Co}(\text{III})\text{OR}$ ($\text{R} = \text{Ph}$ **3a**, iPr **3b**) were explored (Scheme 3.12). Complexes **3a** and **3b** displayed a paramagnetically-shifted ^1H NMR spectrum with relatively sharp

resonances (average $\nu_{1/2}$ for all methyl resonances: 6.7 Hz (**3a**), 31 Hz (**3b**)), and chemical shifts ranging from 26 to -10 ppm for **3a**, and from 47 to -11 ppm for **3b**. Single crystals of **3a** suitable for X-ray diffraction analysis were obtained by liquid diffusion of pentane into a dichloromethane solution of **3a** at low temperatures. Crystals of complex **3b** could not be isolated due to the reactivity towards adventitious water. While analysis of the reaction mixture by ^1H NMR spectroscopy supported the formation of **3b**, attempts to isolate the product through standard washings and extractions led to the formation of the paramagnetic hydroxo complex **4**, which was independently prepared by reaction of **2** with either sodium or cesium hydroxide (See Figure 3.5 for solid state structures).

Complex **4** could also be generated by protonolysis of **3a** with water. The UV-visible spectrum of **4** resembled that of the Co(III) complexes **2** and **3a** (Figure 3.4). All three cobalt(III) complexes (**2**, **3a**, and **4**) have intense absorption in the 550-600 nm range ($\epsilon > 5000 \text{ M}^{-1} \text{ cm}^{-1}$), while **1** has a low absorption in the same range. The strong absorption bands are consistent with and attributed to ligand-to-metal charge transfer from the $[\text{NNN}]^{2-}$ ligand to cobalt(III), which was further corroborated by DFT calculations.

The resonances observed in the relatively sharp (average $\nu_{1/2}$ for all methyl resonances: 13 Hz) paramagnetically-shifted (δ 48 to -11 ppm) ^1H NMR spectrum of **4** are consistent with the expected structure. The hydroxy resonance was however not ob-

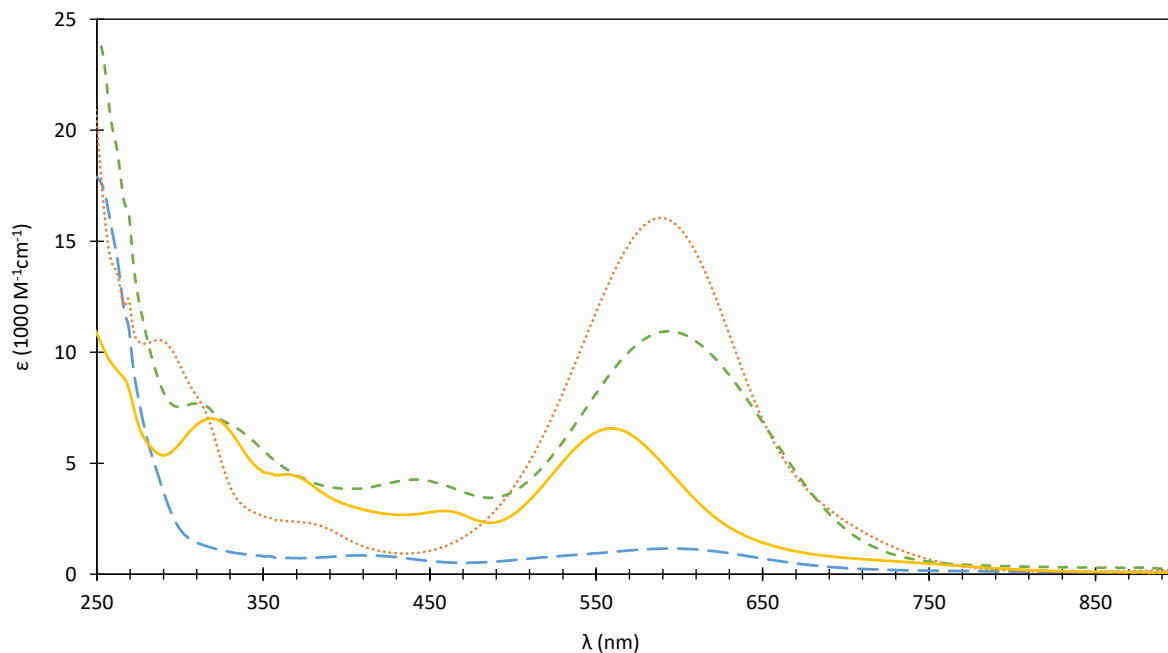


Figure 3.4: UV-Vis spectra of **1** (long dashed; blue), **2** (dotted; red), **3a** (short dashed; green), and **4** (solid line; yellow) in dichloromethane (0.05 M) at room temperature.

served. The X-ray diffraction analysis of complex **4** corroborated the structure and the coordination of the hydroxy ligand to the metal. The hydrogen atom was successfully located on the differential electron density map, eliminating the need to use the calculated position in a riding model to confirm the molecular structure. A search of the Cambridge Crystallographic Data Center (CCDC) database revealed that complex **4** represents the first structurally-characterized cobalt(III) hydroxide complex and the first square planar first-row transition metal in the +3 oxidation state with a terminal hydroxide.

The spin-only magnetic moment for **3a** and **4**, respectively, was determined in THF- d_8 at room temperature by the Evans method and found to be of 2.4 and 2.7 μ_B , consistent

with two unpaired electrons. Complex **3b** could not be isolated in a pure enough form for magnetic moment measurements. The paramagnetism of **3** based on a Co(II) oxyl radical species is ruled out based on crystallographic and spectroscopic data. Crystallographic data of Co(II) oxyl radical species show a lengthening of Co–O bond and a shortening of O–C_{*ipso*},^{103–105} while spectroscopic data show strong absorptions in 400 nm region.^{106–108} The Co–O and O–C_{*ipso*} bond lengths of complex **3a** are within the literature values for a phenolato bonding mode. Complexes **3a** and **4** (and most likely **3b**) thus adopt a triplet ground state (S = 1, as predicted by DFT calculations) at room temperature, commonly observed in square planar Co(III) complexes.^{109–111}

3.3.2 X-ray Studies

X-ray diffraction analysis on single crystals were used to determine the solid-state structure for complexes **2**, **3a** and **4**. All complexes adopt a slightly-distorted square planar geometry in the solid state, with four-coordinate geometry index (τ_4) values of 0.09, 0.10, and 0.11, respectively.¹¹² The cobalt atom is positioned within 0.03 (**2**, **4**) to 0.09 Å (**3a**) from the mean plane formed by the three nitrogen atoms of the [NNN]²⁻ ligand (Figure 3.5). The sum of the angles about the amido nitrogen atoms ranges from 359.0 to 360.0°, highlighting the trigonal planar geometry and the sp² hybridization of N2,3,

which enhances the stability of these otherwise electronically-unsaturated metal centers through donation of π -electron density into empty d -orbitals on the metal. The cobalt-amides bond lengths in **2** are unusually short, with an average of 1.792 Å. These bond lengths are in fact the shortest cobalt(III)-amide bonds reported in the CCDC database. Co–NR₂ single bond lengths normally range from 1.87 to 1.92 Å,^{113–118} while Co=NR double bond lengths range from 1.66 to 1.69 Å.^{119–121}

The coordinating amido groups enforce a much shorter Co–N1 bond length **2** (1.829(3) Å), compared to Co–N4 (1.938(3) Å) (Table 3.1). The corresponding Co–N1 bond in **3a** remains unchanged at 1.829(3) Å but elongates to 1.8573(16) Å in **4**. Likewise, the Co–NR₂ bonds in **2** and **3a** are statistically equivalent, but they are elongated in **4**. The Co–O1 and O1–C28 bond lengths in **3a** are 1.8984(7) Å and 1.329(3) Å, respectively, well within the literature values of Co-bonded anionic phenoxide ligands.^{105,107,108,122,123} The phenoxide is almost perpendicular (85°) to the mean plane formed by N1, N2 and N3, with a C28–O1–Co–N2 torsional angle of 81°. The Co–O1 bond length (1.7945(15) Å) in complex **4** is shorter than that reported in other 3d transition metal complexes containing a terminal hydroxide ligand.¹²⁴ The planes formed by xylyl groups in **2**, **3a**, and **4** are 80–86° to the plane formed by [NNN]²⁻ ligand.

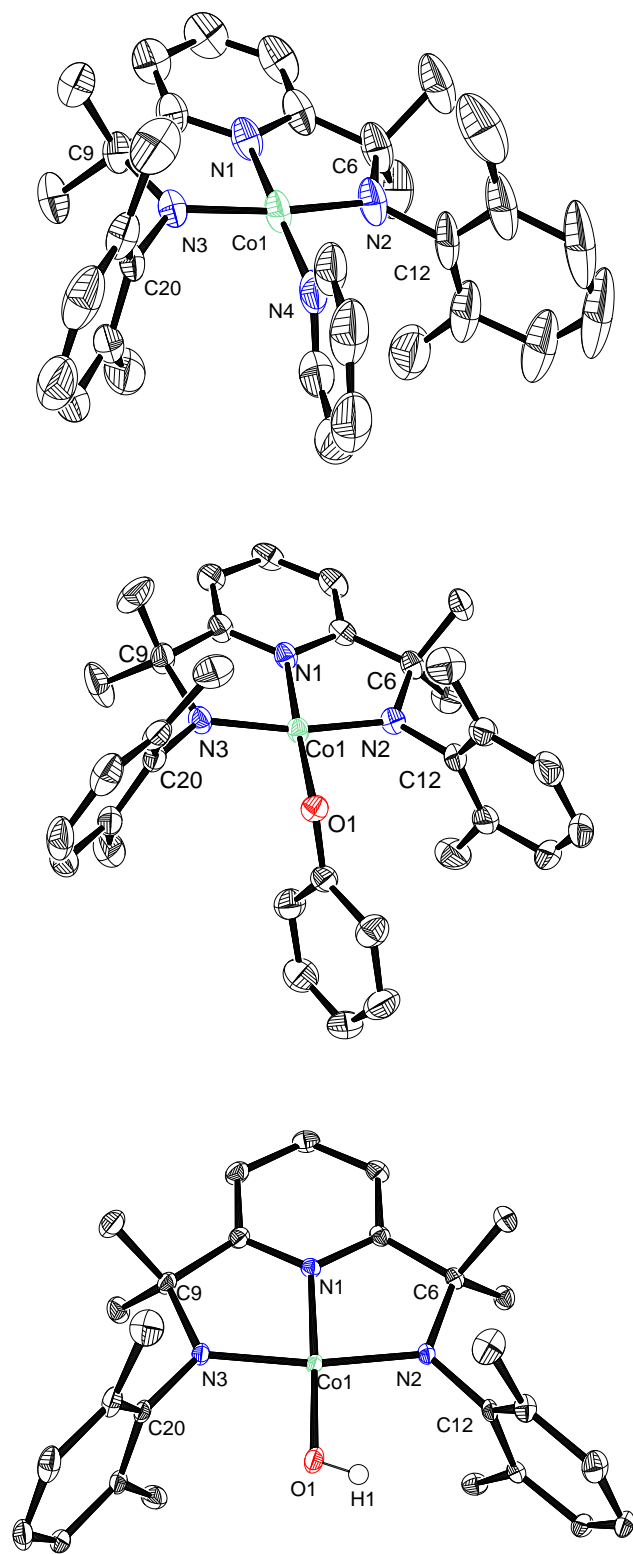


Figure 3.5: ORTEP representations of **2** (top), **3a** (middle), **3c** (bottom) (50% probability level). Most hydrogens atoms, the BF_4 counteranion in **2** and solvent molecules in **3a** and **3c** were removed for clarity. Selected bond lengths and angles are presented in Table 3.1.

Table 3.1: Selected bond lengths (Å) and bond angles (deg) for complexes **2**, **3a** and **4**.

Complexes	2	3a	4
Co–N1	1.829(3)	1.829(2)	1.8573(16)
Co–N2	1.788(3)	1.790(2)	1.8363(16)
Co–N3	1.796(2)	1.796(2)	1.8392(16)
Co–N4	1.938(3)		
Co–O1		1.8984(17)	1.7945(15)
N1–Co–N2	84.86(13)	84.93(10)	83.64(7)
N2–Co–N3	169.42(13)	168.52(10)	167.71(7)
N1–Co–N4	178.33(13)		
N1–Co–O1		177.03(9)	177.17(7)
Co1–O1–C28		120.86(16)	

3.3.3 Cyclic Voltammetry

Cyclic voltammetry of the cationic complex **2** in dichloromethane shows a reversible one-electron $\text{Co}^{\text{II/III}}$ couple at -0.93 V, and a ligand-based ($[\text{NNN}]^{2-}/[\text{NNN}]^{1-}$) quasi-reversible one-electron couple at 0.70 V (Figure 3.6). The metal-based redox couple in the neutral complex **3a** occurs at a higher negative potential (-1.47 V), with two oxidation peaks (E_{pa}) at -0.02 V and 0.89 V, centered on the organic fragments. Complex **4** shows an irreversible reduction of $\text{Co}(\text{III})$ at -1.82 V and a ligand-based reversible one-electron redox process at 0.00 V. DFT calculations predict that the redox events at $E_{pa} +0.80$ (**2**) and 0.05 V (**4**) occur on the $[\text{NNN}]^{2-}$ ligand itself, while the irreversible anodic peaks for **3a** involve both the phenoxide ($E_{pa} -0.02$ V) and $[\text{NNN}]^{2-}$ ($E_{pa} 0.89$ V) ligands. Thus, the anodic potentials for oxidation of the $[\text{NNN}]^{2-}$ ligand in **2** ($[\text{NNN}]\text{Co}(\text{py})^{1+}$) and **3a** ($[\text{NNN}]\text{Co}(\text{OPh})^{1+}$) are within 0.09 V of each other and, as expected based on the greater

charge of the complexes, approximately 0.80 V higher than that for **4** ([NNN]Co(OH)).

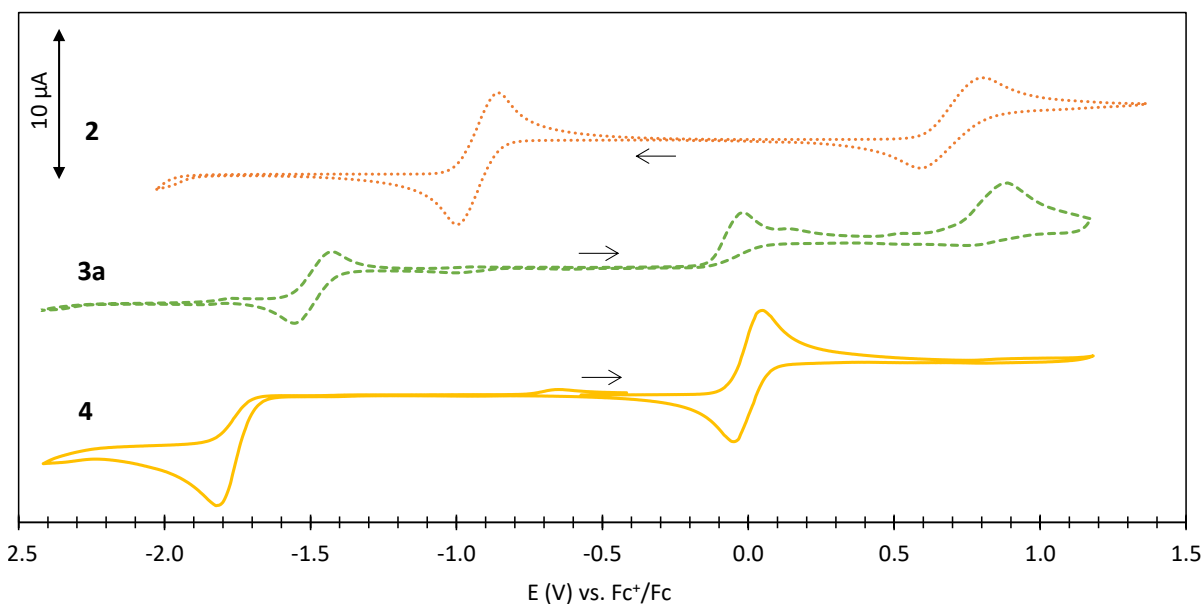


Figure 3.6: Cyclic voltammograms of **2** (dotted; red), **3a** (dashed; green), **4** (solid line; yellow) in dichloromethane (0.1 M $Bu_4N(PF_6)$) at room temperature (scan rate 100 mVs^{-1}).

3.3.4 Density Functional Theory Calculations

DFT calculations were performed on complexes **2**, **3a**, and **4**. The geometry of these complexes were optimized at the B3LYP level of theory using the LANL2DZ basis set, and calculations were performed in the singlet state and in the unrestricted triplet state. Energies were calculated on the optimized structure with the triple-zeta valence polarized basis set (def-TZVP). Similar methods have been used to study Co systems.^{105,125} These calculations indicate that the triplet state is more energetically favored than the singlet

state by approximately 7 kcal/mol (**3a**) and 16 kcal/mol (**3b**, **4**). In contrast, both spin states for the cationic complex **2** have approximately the same energy (within 0.1 kcal/mol). These calculations thus support the observed diamagnetism of complex **2** and paramagnetism of complexes **3** and **4**. The composition of the frontier orbitals in molecular orbital diagram of complexes **2**, **3a** and **4** were analyzed by the AOMix software^{126,127} where the complexes were split into three fragments: Co^{3+} , $[\text{NNN}]^{2-}$, and the second donor (py in **2**, ^-OPh in **3a**, or ^-OH in **4**). AOMix was also used to match the α -orbitals with the β -orbitals of the paramagnetic complexes and quantify the match (q) on a scale from 0 (poor) to 1 (excellent). Summary table and visualizations of all molecular orbitals presented herein are available the appendix.

The lowest unoccupied molecular orbital (LUMO) of complex **2** consists of a π^* -antibonding interaction between the d_{xz} orbital on cobalt and p_z orbitals on the amide nitrogen atoms. The corresponding $\pi(d_{xz},p_z)$ -bonding interaction was located (HOMO-10), indicating that Co–N bond order is 1.5, consistent with the short Co–N_{2,3} bond length in the solid-state structure of **2** (Figure 3.7). The $[\text{NNN}]^{2-}$ contribute at least 85% of the electron density for the highest occupied molecular orbitals HOMO to HOMO-4, with the electron density in HOMO to HOMO-2 solely localized on the xylyl groups, indicating easy oxidation of the ligand as observed in the cyclic voltammetry.

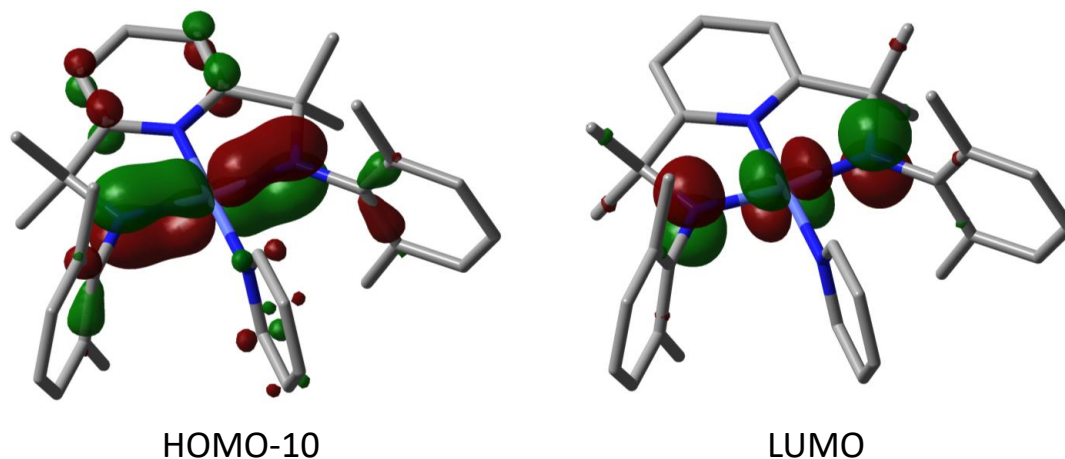


Figure 3.7: π -Character of the Co-N_{2,3} bonds in complex **2** (isovalue of $0.04 \text{ e}^-/\text{\AA}^3$).

The composition of the two lowest singly unoccupied molecular orbitals (LSUMO, and LSUMO+1) in complex **3a** are split approximately equally between the cobalt atom (55%) and the $[\text{NNN}]^{2-}$ ligand (45%). LSUMO+1 is a π^* -orbital arising from d_{xz} , p_z -interactions between cobalt (d_{xz}) and nitrogen (p_z), with the corresponding (also antibonding) singly occupied molecular orbital HSOMO-3 ($q = 0.81$). The short Co-N bond lengths observed in the solid state structure of **3a** are further supported by other π -bonding interactions (HSOMO-15 and HSOMO-53). The two highest singly occupied molecular orbitals (HSOMO and HSOMO-1) are related to each other ($q = 1.0$) and principally localized (96%) on the phenoxide ligand (Figure 3.8). The next four lower energy α -orbitals matched with their β -orbital with $q > 0.90$. Orbital sets HSOMO-5/HSOMO-4 and HSOMO-9/HSOMO-8 mainly composed of $[\text{NNN}]^{2-}$ fragment (>94%), while HSOMO-6/HSOMO-7 and HSOMO-11/HSOMO-10 are composed of both $[\text{NNN}]^{2-}$

and $^-$ OPh fragments in ratios of approximately 30:70 and 75:25, respectively. These data support the ability of both $[\text{NNN}]^{2-}$ and $^-$ OPh to easily get oxidized, as observed in the cyclic voltammetry.

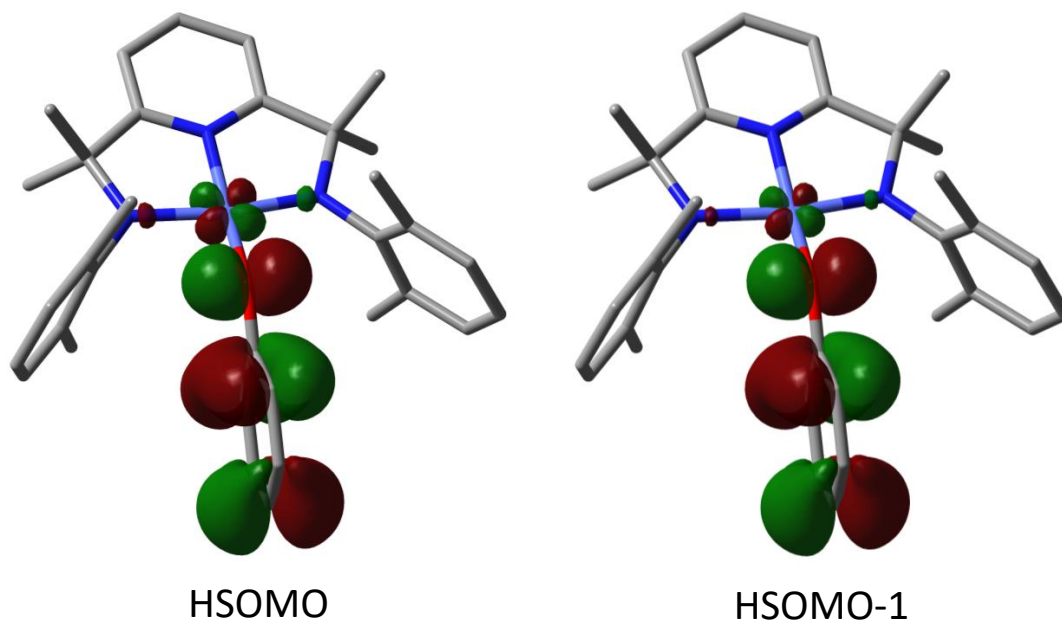


Figure 3.8: HSOMO and HSOMO-1 of complex **3a** (isoval $0.045 e^-/\text{\AA}^3$).

As for complex **4**, the lowest unoccupied orbitals LSUMO+1 and LSUMO ($q = 0.67$) are respectively 98% and 58% composed of the pyridine π -system from the $[\text{NNN}]^{2-}$ ligand. As observed in complex **3a**, HSOMO and LSUMO+2 ($q = 0.81$) of complex **4** are also π^* -interactions of d_{xz}, p_z -atomic orbitals. As noted for **2** and **3a**, additional π -bonding molecular orbitals (HSOMO-11 and HSOMO-38) result in short Co-N bond lengths. Orbital sets HSOMO-3/HSOMO-2, HSOMO-4/HSOMO-5, HSOMO-8/HSOMO-7, and HSOMO-10/HSOMO-9 are composed of more than 95% of the $[\text{NNN}]^{2-}$ frag-

ment with most of the electron density again localized on the xylyl rings. In contrast, the electron density in orbital set HSOMO-6/HSOMO-1 contains significant amido N p_z -character.

The DFT calculations thus proved helpful in interpreting the observed electrochemistry for complexes **2**, **3a** and **4**. All complexes show a large Co contribution (>50% for **2** and **3a**, 35% for **4**) to the lowest unoccupied molecular orbitals indicating that cathodic peaks at -0.93 (**2**), -1.47 (**3a**) and -1.82 V (**4**) correspond to the reduction of Co(III) to Co(II). In contrast, the highest occupied molecular orbitals are generally localized on either the $[\text{NNN}]^{2-}$ or $^-\text{OPh}/^-\text{OH}$ ligands with small (<15%) Co contribution. Orbitals with >15% Co contribution are at least 18 kcal/mol lower in energy than the highest occupied molecular orbitals (HOMO in **2** or HSOMO in **3a** and **4**), indicating that the redox couples at 0.70 (**2**), 0.00 V (**4**) and anodic peaks at -0.19, and 0.89 V (**3a**) are all principally ligand-based. Specifically, these ligand-based activities are localized on the xylyl ring for complex **2**, and on either the xylyl ring or the amido groups for complex **4**. The HSOMO and HSOMO-1 orbitals for complex **3a** are localized on the aromatic phenoxide ring, with the xylyl groups heavily contributing to HSOMO-2 to HSOMO-5. This suggests that the anodic peaks at -0.19 and 0.89 V correspond to the oxidation of the phenoxide phenyl ring and of the xylyl group of the $[\text{NNN}]^{2-}$ ligand, respectively.

3.4 Conclusions and Future Remarks

A series of low valent Co(III) square planar complexes supported by a dianionic pincer bis(amido)pyridine ligand was synthesized and characterized, including an unprecedented and first ever structurally-characterized square planar Co(III) hydroxide complex. The magnetic properties of these complexes were found to be highly dependent on the charge and nature of coordination sphere imparted by the second ligand, chosen from either pyridine, phenoxide or hydroxide. While the cationic pyridine complex **2** is diamagnetic, complexes **3** and **4** exhibit paramagnetism with two unpaired electrons. Double bond character between the metal and the anilido nitrogen was evident from X-ray diffraction analysis and further supported by DFT calculations for complex **2**. Complex **2** shows well-behaved redox chemistry. In contrast, both complexes **3a** and **4** showed some irreversible redox processes on either cobalt or ligands. The corresponding hydride and alkyl complexes could not be isolated, presumably due to their high reactivity and homolysis of the new bond formed.

Future work on complexes **2**, **3a**, and **4** can focus on few areas. Work toward the synthesis and isolation of organocobalt(III) complexes from **3a** and **4** can be explored. The anionic oxyl ligands in complexes **3a**, **3b**, and **4** can be potentially substituted by alkyl

groups to form organocobalt(III) complexes. For instance, reactions between alkylating agent ($\text{LiCH}_2\text{SiMe}_3$, $\text{CH}_2\text{CHCH}_2\text{MgCl}$, and LiMe) and **3a** or **4** can be studied. Also, the high reactivity of organocobalt(III) complexes can be utilized in controlled radical polymerization. Future research can explore the viability of complex **2** as a CMRP catalyst for monomers such as acrylic esters and vinyl esters. Preliminary results between **2** and hydrogen or ethylene at approximately 1.2 atm showed no reactivity. Reactions conducted in stainless steel autoclave under higher pressures (10-30 atm) can be explored.^{19,68} Also, reactions of **2** with MAO under an atmosphere of ethylene can be investigated. These reactions will provide experimental data on the viability of complex **2** to catalyze hydrogenation and olefin polymerization. Finally, work can be directed towards isolation and full characterization of the bis(amido)pyridine cobalt(III) isopropoxide (**3b**) complex. This complex is predicted to be stable at room temperature under anhydrous condition evidenced by the ^1H NMR spectrum. Stability and propensity of complex **3b** to undergo β -hydrogen elimination can be explored at higher temperatures to probe its viability in transfer hydrogenation chemistry.

3.5 Experimental

General Considerations

Unless otherwise noted, all manipulations were carried out using oven-dried glassware and performed under argon using standard Schlenk line techniques or in a nitrogen-filled mBraun glovebox. Solvents were dried using an mBraun solvent purification system (MB-SPS) fitted with alumina columns and stored over molecular sieves under argon. Deuterated NMR solvents were purchased from Sigma-Aldrich, degassed using three freeze-pump-thaw cycles, vacuum distilled from Na/benzophenone (C_6D_6) and CaH_2 (CD_2Cl_2), and stored under argon or nitrogen. NMR spectra were recorded on Bruker DRX 600, Bruker AV 400 or Bruker AV 300 spectrometer at room temperature. $[NNN]H_2$,⁷ $CoCl_2py_4$ ¹²⁸ were synthesized according to literature procedures. Sodium isopropoxide and sodium phenoxide were prepared from the corresponding alcohol and sodium metal. Bu_4NPF_6 , $CoCl_2$ and $AgBF_4$, $LiCH_2SiMe_3$ (1.0 M in pentane) were purchased from Sigma-Aldrich and used as received.

[NNN]Co(py) (1)

Complex **1** was prepared following an experimental procedure reported by Summerscales and Gordon for a related complex.⁶ To 50 mL toluene mixture of H₂[NNN] (2.23 g, 5.00 mmol) and CoCl₂py₄ (2.01 g, 5.00 mmol) cooled to -40 °C was added a solution of LiCH₂SiMe₃ (1.0 M in pentane; 10.5 mL, 10.5 mmol), resulting in a colour change from cyan to red. After stirring overnight at room temperature, the mixture was filtered with a cannula filter, and the volatiles were evaporated under vacuum. The crude red solids were washed with cold pentane and dried under vacuum. Yield: 1.84 g, 3.45 mmol, 69%.

[[NNN]Co(py)]BF₄ (2)

A 20 mL toluene solution of **1** (1.84 g, 3.43 mmol) was added to a 20 mL toluene suspension of AgBF₄ (0.667 g, 3.43 mmol) at room temperature and the mixture was stirred for 2 h. The supernatant was removed, and the residual solids were washed with toluene. The product was extracted with dichloromethane, and the volatiles from the solution removed in vacuo to yield a dark blue solid (1.90 g, 3.1 mmol, 90%). Crystals for X-ray crystallography were grown by pentane diffusion into dichloromethane solution.

¹H NMR (400 MHz; CD₂Cl₂): δ 9.60 (d, ³J = 5.2 Hz, 2H, *o*-CH_{py}), 8.54 (t, ³J = 8.0 Hz, 1H, *p*-CH) 7.79 (d, ³J = 7.9 Hz, 2H, *m*-CH), 7.72 (t, ³J = 7.5 Hz, 1H, *p*-CH_{py}),

7.15 (dd, 2H, *m*-CH_{py}), 6.77 (t, ³J = 7.6 Hz, 2H, *p*-CH_{xylyl}), 6.45 (d, ³J = 7.4 Hz, 4H, *m*-CH_{xylyl}), 1.90 (s, 12H, CH_{3(xylyl)}), 1.29 (s, 12H, C(CH₃)₂). ¹³C¹H NMR (100 MHz, CD₂Cl₂): δ 172.4 (*o*-C), 155.4 (*o*-C_{py}), 152.2 (*o*-C_{xylyl}), 140.8 (*p*-C), 139.1 (*p*-C_{py}), 128.3 (*m*-C_{xylyl}), 127.1 (*ipso*-C_{xylyl}), 125.5 (*p*-C_{xylyl}, and *m*-C_{py}), 119.7 (*m*-C), 91.8 (C(CH₃)₂), 23.0 (C(CH₃)₂), 21.5 (C_{xylyl}H₃). ¹⁹F NMR (376 MHz; CD₂Cl₂): -152.5 (s, BF₄). Anal. Calcd for C₃₂H₃₈N₄CoBF₄: C, 61.55; H, 6.13; N, 8.97. Found: C, 61.29; H, 5.87; N, 8.58.

[NNN]Co(OPh) (3a)

A 5 mL dichloromethane solution of **2** (106 mg, 0.170 mmol) was added to a 5 mL dichloromethane suspension of sodium phenoxide (22.6 mg, 0.185 mmol) resulting in a slight colour change to a lighter blue. The mixture was stirred at room temperature for 1 h, filtered and dried in vacuo. The product was isolated by extraction with toluene. The volatiles were removed in vacuo and the blue solid further washed with pentane (5 × 25 mL). Yield 64 mg, 0.12 mmol, 68 %. Crystals for X-ray crystallography were grown from pentane diffusion into dichloromethane solution stored at -40 °C. ¹H NMR (400 MHz; C₆D₆): δ 26.49 (d, ³J = 7.1 Hz, 4H, *m*-CH_{xylyl}), 13.31 (dd, 2H, *m*-CH_{Ph}), 10.73 (t, ³J = 7.1 Hz, 2H, *p*-CH_{xylyl}), 3.59 (t, ³J = 6.8 Hz, 1H, *p*-CH_{Ph}), 2.94 (d, ³J = 7.2 Hz, 2H, *m*-CH), 2.60 (t, ³J = 7.0 Hz, 1 H, *p*-CH) 2.21 (s, 12H), -3.91 (s, 12H), -9.74 (d, ³J =

7.0 Hz, 2H, *o*-CH_{Ph}). ¹³C-¹H NMR (100 MHz; C₆D₆): δ 246.2, 200.5, 172.5, 137.1 126.8, 108.8, -22.1. Anal. Calcd for C₃₃H₃₈CoN₃O: C, 71.85; H, 6.94; N, 7.62. Found: C, 71.59; H, 7.17; N, 7.38. Magnetic moment (THF, 0.05 M): 2.4 B.M.

[NNN]Co(O^{*i*}Pr) (**3b**)

Complex **3b** was prepared using the procedures described for **3a** on a 0.0167-mmol scale.

The formation of **3b** is consistent with ¹H NMR spectroscopic data but could not be cleanly isolated due to observed decomposition. ¹H NMR (400 MHz; C₆D₆): δ 47.29 (br, 4H, *m*-CH^{*xylyl*}), 35.06 (br, 1H, OCH(CH₃)₂), 15.72 (br, 2H, *p*-CH^{*xylyl*}), 6.44 (br, 6H, OCH(CH₃)₂), 0.42 (br, 2H, *m*-CH), 0.04 (12H), -3.90 (br, 1H, *p*-CH), -10.90 (12H).

[NNN]Co(OH) (**4**)

To a 5-mL dichloromethane solution of **2** (79 mg, 0.13 mmol) was added excess NaOH pellets (or CsOH•H₂O), with no attempt to exclude moisture or air from the reaction mixture. The reaction mixture was stirred vigorously for 1 h at room temperature. The mixture was filtered, and the solvent from the filtrate evaporated. The product was extracted using toluene. The solvent was evaporated and the product was washed with warm hexanes to give **4** as a purple solid (47 mg, 0.10 mmol, 77%). Crystals for X-ray

crystallography were grown from dichloromethane/pentane mixture stored at 0 °C. ^1H NMR (400 MHz; C_6D_6): δ 48.58 (d, $^3J = 7.3$ Hz, 4H, $m\text{-CH}_{xylyl}$), 14.90 (t, $^3J = 7.2$ Hz, 2H, $p\text{-CH}_{xylyl}$), 2.71 (s, 12H), 0.21 (d, $^3J = 7.0$, 2H, $m\text{-CH}$), -9.98 (s, 12H), -11.04 (t, $^3J = 6.9$ Hz, 1H, $p\text{-CH}$). Anal. Calcd for $\text{C}_{27}\text{H}_{34}\text{CoN}_3\text{O}$: C, 68.05; H, 7.40; N, 8.82. ^{13}C NMR (151 MHz; C_6D_6): δ 322.8, 297.2, 244.1, 128.9, 91.5, -63.5, -110.0. Anal. Calcd for $\text{C}_{27}\text{H}_{34}\text{CoN}_3\text{O}$: C, 68.05; H, 7.40; N, 8.82. Found: C, 68.31; H, 7.28; N, 8.55. Magnetic moment (THF, 0.05 M): 2.7 B.M.

Cyclic Voltammetry

Cyclic voltammograms were measured using a BASi-Epsilon potentiostat on dichloromethane solutions of the analytes (0.01 M) containing 0.1 M Bu_4NPF_6 as electrolyte. A platinum disc (1-mm diameter) and a platinum wire were used as working and auxiliary electrodes, respectively. A silver wire coated with AgCl was used as reference electrode. All potentials were calibrated vs. the Fc^+/Fc redox couple. Half-wave potential ($E_{1/2}$) was estimated as the average of anodic (E_{pa}) and cathodic peak (E_{pc}) potentials.

Computational Details

Geometry optimizations were carried out at the B3LYP^{129–132} hybrid level of theory with the LANL2DZ basis set using Gaussian 09,¹³³ with GaussView 03¹³⁴ for molecular visualization. These calculations were performed on the Shared Hierarchical Academic Research Computing Network (SHARCNET: www.sharcnet.ca). The starting geometries were based X-ray structures but further optimized in the gas phase. Energy calculations were performed at the same functional using triple-zeta valence polarized basis set (def-TZVP).¹³⁵ Composition of molecular orbitals as combinations of atomic orbitals were determined based on data generated by Gaussian 09 using AOMix software.^{126,127}

X-ray Crystallography

Crystallographic data were collected at the University of Toronto on a Bruker Kappa APEX-DUO diffractometer using a monochromated Mo-K α radiation (Bruker Triumph; $\lambda = 0.71073 \text{ \AA}$) at 150 K. Data were measured using a combination of ϕ scans and ω scans, and were processed using APEX2 and SAINT.¹³⁶ Absorption corrections were carried out using SADABS.¹³⁶ Structures were solved with WinGX¹³⁷ or OLEX2¹³⁸ as the graphical user interface using either SHELXL or SHELXT with SHELXS-97 for full-matrix least-squares refinement that was based on F^2 .^{139–141} All H atoms were included

in calculated positions, except for the hydroxy hydrogen atom in **4**, and allowed to refine in riding-motion approximation with U_{iso} tied to the carrier atom.

References

- [1] Younus, H. A.; Ahmad, N.; Su, W.; Verpoort, F. *Coord. Chem. Rev.* **2014**, *276*, 112–152.
- [2] Moulton, C. J.; Shaw, B. L. *J. Chem. Soc., Dalton Trans.* **1976**, *0*, 1020–1024.
- [3] van Koten, G.; Timmer, K.; Noltes, J. G.; Spek, A. L. *J. Chem. Soc., Chem. Commun.* **1978**, 250–252.
- [4] Szabó, K. J. In *Organometallic Pincer Chemistry*; van Koten, G., Milstein, D., Eds.; Springer, 2013.
- [5] Cruz, C. A.; Emslie, D. J. H.; Harrington, L. E.; Britten, J. F.; Robertson, C. M. *Organometallics* **2007**, *26*, 692–701.
- [6] Summerscales, O. T.; Stull, J. A.; Scott, B. L.; Gordon, J. C. *Inorg. Chem.* **2015**, *54*, 6885–90.
- [7] Tay, B. Y.; Wang, C.; Chia, S. C.; Stubbs, L. P.; Wong, P. K.; Van Meurs, M. *Organometallics* **2011**, *30*, 6028–6033.
- [8] Guérin, F.; McConville, D. H.; Vittal, J. J. *Organometallics* **1996**, *7333*, 5586–5590.
- [9] Guérin, F.; McConville, D. H.; Payne, N. C. *Organometallics* **1996**, *15*, 5085–5089.
- [10] Guérin, F.; McConville, D. H.; Vittal, J. J. *Organometallics* **1995**, *14*, 3154–3156.
- [11] Guérin, F.; McConville, D. H.; Vittal, J. J. *Organometallics* **1997**, *16*, 1491–1496.
- [12] Guérin, F.; McConville, D. H.; Vittal, J. J.; Yap, G. a. P. *Organometallics* **1998**, *17*, 5172–5177.
- [13] Estler, F.; Eickerling, G.; Herdtweck, E.; Anwander, R. *Organometallics* **2003**, *22*, 1212–1222.
- [14] Cruz, C. A.; Emslie, D. J. H.; Jenkins, H. A.; Britten, J. F. *Dalton Trans.* **2010**, *39*, 6626–6628.
- [15] Jie, S.; Diaconescu, P. L. *Organometallics* **2010**, *29*, 1222–1230.
- [16] Smeltz, J. L.; Lilly, C. P.; Boyle, P. D.; Ison, E. A. *J. Am. Chem. Soc.* **2013**, *135*, 9433–9441.

- [17] Lilly, C. P.; Boyle, P. D.; Ison, E. A. *Dalton Trans.* **2011**, *40*, 11815–11821.
- [18] Reardon, D.; Conan, F.; Gambarotta, S.; Yap, G.; Wang, Q. *J. Am. Chem. Soc.* **1999**, *121*, 9318–9325.
- [19] Calderazzo, F.; Englert, U.; Pampaloni, G.; Santi, R.; Sommazzi, A.; Zinna, M. *Dalton Trans.* **2005**, *67*, 914–922.
- [20] Blackmore, I. J.; Gibson, V. C.; Hitchcock, P. B.; Rees, C. W.; Williams, D. J.; White, A. J. P. *J. Am. Chem. Soc.* **2005**, *127*, 6012–6020.
- [21] Bruce, M.; Gibson, V.; Redshaw, C.; Solan, G.; White, A.; Williams, D. *Chem. Commun.* **1998**, *990*, 2523–2524.
- [22] Zimmermann, M.; Törnroos, K. W.; Anwander, R. *Angew. Chem., Int. Ed.* **2007**, *46*, 3126–3130.
- [23] Astruc, D. *New J. Chem.* **2005**, *29*, 42.
- [24] Herisson, P. J.-L.; Chauvin, Y. *Die Makromolekulare Chemie* **1970**, *141*, 161–176.
- [25] Grubbs, R. H.; Chang, S. *Tetrahedron* **1998**, *54*, 4413–4450.
- [26] Mol, J. C. *Green Chem.* **2002**, *4*, 5–13.
- [27] Liu, X.; Basu, A. *J. Organomet. Chem.* **2006**, *691*, 5148–5154.
- [28] Schrock, R.; Rocklage, S.; Wengrovius, J.; Rupprecht, G.; Fellmann, J. *J. Mol. Catal.* **1980**, *8*, 73–83.
- [29] Bazan, G. C.; Oskam, J. H.; Cho, H.-n.; Park, L. Y.; Schrock, R. R. *J. Am. Chem. Soc.* **1991**, *113*, 6899–6907.
- [30] Schrock, R. R.; Murdzek, J. S.; Bazan, G. C.; Robbins, J.; DiMare, M.; O'Regan, M. *J. Am. Chem. Soc.* **1990**, *112*, 3875–3886.
- [31] Novak, B. M.; Grubbs, R. H. *J. Am. Chem. Soc.* **1988**, *110*, 7542–7543.
- [32] Nguyen, S. T.; Johnson, L. K.; Grubbs, R. H.; Ziller, J. W. *J. Am. Chem. Soc.* **1992**, *114*, 3974–3975.
- [33] Schwab, P.; Grubbs, R. H.; Ziller, J. W.; August, R. V. *J. Am. Chem. Soc.* **1996**, *118*, 100–110.
- [34] Fu, G. C.; Nguyen, S. T.; Grubbs, R. H. *J. Am. Chem. Soc.* **1993**, *115*, 9856–9857.
- [35] Huang, J.; Stevens, E. D.; Nolan, S. P.; Petersen, J. L.; Orleans, N.; Virginia, W.; Uni, V.; September, R. V. *J. Am. Chem. Soc.* **1999**, *121*, 2674–2678.
- [36] Scholl, M.; Trnka, T. M.; Morgan, J. P.; Grubbs, R. H. *Tetrahedron Lett.* **1999**, *40*, 2247–2250.

- [37] Kingsbury, J. S.; Harrity, J. P. A.; Bonitatebus, P. J.; Hoveyda, A. H.; Hill, C.; September, R. V. *J. Am. Chem. Soc.* **1999**, *121*, 791–799.
- [38] Monfette, S.; Marleau-Gillette, J.; Conrad, J. C.; McDonald, R.; Fogg, D. E. *Dalton Trans.* **2012**, *41*, 14476–9.
- [39] Monfette, S.; Fogg, D. E. *Organometallics* **2006**, *25*, 1940–1944.
- [40] Conrad, J. C.; Parnas, H. H.; Snelgrove, J. L.; Fogg, D. E. *J. Am. Chem. Soc.* **2005**, *127*, 11882–3.
- [41] Conrad, J. C.; Snelgrove, J.; Eelman, M.; Hall, S.; Fogg, D. E. *J. Mol. Catal. A: Chem.* **2006**, *254*, 105–110.
- [42] Buchmeiser, M. R.; Ahmad, I.; Gurram, V.; Kumar, P. S. *Macromolecules* **2011**, *44*, 4098–4106.
- [43] Halbach, T. S.; Mix, S.; Fischer, D.; Maechling, S.; Krause, J. O.; Sievers, C.; Blechert, S.; Nuyken, O.; Buchmeiser, M. R. *J. Org. Chem.* **2005**, *70*, 4687–4694.
- [44] Hong, S. H.; Wenzel, A. G.; Salguero, T. T.; Day, M. W.; Grubbs, R. H. *J. Am. Chem. Soc.* **2007**, *129*, 7961–7968.
- [45] Amoroso, D.; Yap, G. P. a.; Fogg, D. E. *Organometallics* **2002**, *21*, 3335–3343.
- [46] Hong, S. H.; Day, M. W.; Grubbs, R. H. *J. Am. Chem. Soc.* **2004**, *126*, 7414–7415.
- [47] Lummiss, J. A.; Ireland, B. J.; Sommers, J. M.; Fogg, D. E. *ChemCatChem* **2014**, *6*, 459–463.
- [48] Larocque, T. G.; Badaj, A. C.; Lavoie, G. G. *Dalton Trans.* **2013**, *42*, 14955–8.
- [49] Larocque, T. G.; Lavoie, G. G. *New J. Chem.* **2014**, *38*, 499.
- [50] Pump, E.; Fischer, R. C.; Slugovc, C. *Organometallics* **2012**, *31*, 6972–6979.
- [51] Falivene, L.; Poater, A.; Cazin, C. S. J.; Slugovc, C.; Cavallo, L. *Dalton Trans.* **2013**, *42*, 7312–7.
- [52] Sanford, M. S.; Love, J. a.; Grubbs, R. H. *J. Am. Chem. Soc.* **2001**, *123*, 6543–6554.
- [53] Buchowicz, W.; Ingold, F.; Mol, J. C.; Lutz, M.; Spek, A. L. *Chem. Eur. J.* **2001**, *7*, 2842–2847.
- [54] Monfette, S.; Camm, K. D.; Gorelsky, S. I.; Fogg, D. E. *Organometallics* **2009**, *28*, 944–946.
- [55] Anderson, E.; Buchmeiser, M. R. *Synlett* **2011**, *2012*, 185–207.
- [56] McKinty, A. M.; Lund, C.; Stephan, D. W. *Organometallics* **2013**, *32*, 4730–4732.

- [57] McKinty, A. M.; Stephan, D. W. *Dalton Trans.* **2016**, *45*, 3844–52.
- [58] Wasilke, J.-C.; Wu, G.; Bu, X.; Kehr, G.; Erker, G. *Organometallics* **2005**, *24*, 4289–4297.
- [59] Gandelman, M.; Naing, K. M.; Rybtchinski, B.; Poverenov, E.; Ben-david, Y.; Ashkenazi, N.; Gauvin, R. M.; Milstein, D.; Reho, V. *J. Am. Chem. Soc.* **2005**, *127*, 15265–15272.
- [60] Searles, K.; Pinter, B.; Chen, C.-H.; Mindiola, D. J. *Organometallics* **2014**, *33*, 4192–4199.
- [61] Poater, A.; Pump, E.; Vummaleti, S. V. C.; Cavallo, L. *J. Che. Theory Comput.* **2014**, *10*, 4442–4448.
- [62] Benitez, D.; Tkatchouk, E.; Goddard, W. A. *Organometallics* **2009**, *28*, 2643–2645.
- [63] Samouei, H.; Miloserdov, F. M.; Escudero-ada, E. C.; Grushin, V. V. *Organometallics* **2014**, *33*, 7229–7283.
- [64] Hoffman, P. R.; Caulton, K. G. *J. Am. Chem. Soc.* **1975**, *12*, 4221–4228.
- [65] Jayaprakash, K. N.; Gunnoe, T. B.; Boyle, P. D. *Inorg. Chem.* **2001**, *40*, 6481–6486.
- [66] Burrell, A. K.; Steedman, A. J. *Organometallics* **1997**, *16*, 1203–1208.
- [67] Holland, A. W.; Bergman, R. G. *J. Am. Chem. Soc.* **2002**, *124*, 14684–14695.
- [68] Takemoto, S.; Kawamura, H.; Yamada, Y.; Okada, T.; Ono, A.; Yoshikawa, E.; Mizobe, Y.; Hidai, M. *Organometallics* **2002**, *21*, 3897–3904.
- [69] Takemoto, S.; Oshio, S.; Kobayashi, T.; Matsuzaka, H.; Hoshi, M.; Okimura, H.; Yamashita, M.; Miyasaka, H.; Ishii, T.; Yamashita, M. *Organometallics* **2004**, *23*, 3587–3589.
- [70] Christian, G. J.; Stranger, R.; Yates, B. F. *Inorg. Chem.* **2006**, *45*, 6851–6859.
- [71] Nakajima, Y.; Shimada, S. *RSC Adv.* **2015**, *5*, 20603–20616.
- [72] Tang, H.; Richey, H. G. *Organometallics* **2001**, *20*, 1569–1574.
- [73] Viebrock, H.; Weiss, E. *J. Organomet. Chem.* **1994**, *464*, 121–126.
- [74] Hallman, P. S.; Stephenson, T. A.; Wilkison, G. *Inorg. Synth.* **1970**, *XII*, 237–240.
- [75] Batista, A. A.; Santiago, M. O.; Donnici, C. L.; Moreira, I. S.; Healy, P. C.; Berners-Price, S. J.; Queiroz, S. L. *Polyhedron* **2001**, *20*, 2123–2128.
- [76] Oakdale, J. S.; Sit, R. K.; Fokin, V. V. *Chem. Eur. J.* **2014**, *20*, 11101–10.
- [77] Watson, S. C.; Eastham, J. F. *J. Organomet. Chem.* **1967**, *9*, 165–168.

- [78] Blackman, A. G. In *Encyclopedia of Inorganic Chemistry*; King, R. B., Ed.; Wiley: New York, 2006.
- [79] Bahrmann, H.; Bach, H.; Frey, G. D. In *Ullmann's Encyclopedia of Industrial Chemistry*; Elvers, B., Ed.; Wiley, 2013.
- [80] Deutschmann, O.; Knozinger, H.; Kochloeff, K.; Turek, T. In *Ullmann's Encyclopedia of Industrial Chemistry*; Elvers, B., Ed.; Wiley, 2011.
- [81] Debuigne, A.; Poli, R.; Jérôme, C.; Jérôme, R.; Detrembleur, C. *Prog. Polym. Sci.* **2009**, *34*, 211–239.
- [82] Jeremic, D. In *Ullmann's Encyclopedia of Industrial Chemistry*; Elvers, B., Ed.; Wiley, 2014.
- [83] Gahleiter, M.; Paulik, C. In *Ullmann's Encyclopedia of Industrial Chemistry*; Elvers, B., Ed.; Wiley, 2014.
- [84] Keim, W. *Angew. Chem., Int. Ed.* **2013**, *52*, 12492–12496.
- [85] Takeuchi, D. In *Organometallic Reactions and Polymerization*, volume 85 ed.; Osaka, K., Ed.; Springer Berlin Heidelberg, 2014; pp 119–167.
- [86] Gibson, V. C.; Redshaw, C.; Solan, G. A. *Chem. Rev.* **2007**, *107*, 1745–1776.
- [87] Liu, Z.; Somsook, E.; White, C. B.; Rosaaen, K. A.; Landis, C. R. *J. Am. Chem. Soc.* **2001**, *123*, 11193–11207.
- [88] Resconi, L.; Piemontesi, F.; Camurati, I.; Sudmeijer, O.; Nifant'ev, I. E.; Ivchenko, P. V.; Kuz'mina, L. G. *J. Am. Chem. Soc.* **1998**, *120*, 2308–2321.
- [89] Gibson, V. C.; Humphries, M. J.; Tellmann, K. P.; Wass, D. F.; White, A. J. P.; Williams, D. J. *Chem. Commun.* **2001**, *120*, 2252–2253.
- [90] Kooistra, T. M.; Knijnenburg, Q.; Smits, J. M. M.; Horton, A. D.; Budzelaar, P. H. M.; Gal, A. W. *Angew. Chem., Int. Ed.* **2001**, *113*, 4719–4722.
- [91] Britovsek, G. J. P.; Gibson, V. C.; McTavish, S. J.; Solan, G. A.; White, A. J. P.; Williams, D. J.; Britovsek, G. J. P.; Kimberley, B. S.; Maddox, P. J. *Chem. Commun.* **1998**, *34*, 849–850.
- [92] Humphries, M. J.; Tellmann, K. P.; Gibson, V. C.; White, A. J. P.; Williams, D. J. *Organometallics* **2005**, *24*, 2039–2050.
- [93] Daugulis, O.; Brookhart, M.; White, P. S. *Organometallics* **2003**, *22*, 4699–4704.
- [94] Noyori, R. *Angew. Chem., Int. Ed.* **2002**, *41*, 2008–2022.
- [95] Morris, R. H. *Acc. Chem. Res.* **2015**, *48*, 1494–1502.

- [96] Jeon, J. Y.; Lee, J. J.; Varghese, J. K.; Na, S. J.; Sujith, S.; Go, M. J.; Lee, J.; Ok, M.; Lee, B. Y. *Dalton Trans.* **2013**, *42*, 9245–9254.
- [97] Stolzenberg, A. M.; Cao, Y. *J. Am. Chem. Soc.* **2001**, *123*, 9078–9090.
- [98] Omar, H. A. A.; Moore, P.; Alcock, N. W. *J. Chem. Soc., Dalton Trans.* **1994**, 2631.
- [99] Maria, S.; Kaneyoshi, H.; Matyjaszewski, K.; Poli, R. *Chem. Eur. J.* **2007**, *13*, 2480–2492.
- [100] Fryzuk, M. D.; Leznoff, D. B.; Thompson, R. C.; Rettig, S. J. *J. Am. Chem. Soc.* **1998**, *120*, 10126–10135.
- [101] Setsune, J.-i.; Ishimaru, Y.; Moriyama, T.; Kitao, T. *J. Chem. Soc., Chem. Commun.* **1991**, 555.
- [102] Ram, M. S.; Riordan, C. G.; Yap, G. P. A.; Liable-Sands, L.; Rheingold, A. L.; Marchaj, A.; Norton, J. R. *J. Am. Chem. Soc.* **1997**, *119*, 1648–1655.
- [103] Sokolowski, A.; Bothe, E.; Bill, E.; Weyhermüller, T.; Wieghardt, K.; Strate-meier, H.; Reinen, D.; Knowles, P. F. *Chem. Commun.* **1996**, *28*, 1671–1672.
- [104] Adam, B.; Bill, E.; Bothe, E.; Goerdts, B.; Haselhorst, G.; Hildenbrand, K.; Sokolowski, A.; Steenzen, S.; Weyhermüller, T.; Wieghardt, K. *Chem. Eur. J.* **1997**, *3*, 308–319.
- [105] Roy, A. S.; Muresan, N.; Tuononen, H. M.; Rath, S. P.; Ghosh, P. *Dalton Trans.* **2008**, 3438.
- [106] Kochem, A.; Kanso, H.; Baptiste, B.; Arora, H.; Philouze, C.; Jarjayes, O.; Vezin, H.; Luneau, D.; Orio, M.; Thomas, F. *Inorg. Chem.* **2012**, *51*, 10557–10571.
- [107] Sokolowski, A.; Adam, B.; Weyhermüller, T.; Kikuchi, A.; Hildenbrand, K.; Schnepf, R.; Hildebrandt, P.; Bill, E.; Wieghardt, K. *Inorg. Chem.* **1997**, *36*, 3702–3710.
- [108] Benisvy, L.; Bill, E.; Blake, A. J.; Collison, D.; Davies, E. S.; Garner, C. D.; Guindy, C. I.; McInnes, E. J. L.; McArdle, G.; McMaster, J.; Wilson, C.; Wolowska, J. *Dalton Trans.* **2004**, *83*, 3647.
- [109] Lagaditis, P. O.; Schluschaß, B.; Demeshko, S.; Würtele, C.; Schneider, S. *Inorg. Chem.* **2016**, *55*, 4529–4536.
- [110] García-Monforte, M. A.; Ara, I.; Martín, A.; Menjón, B.; Tomás, M.; Alonso, P. J.; Arauzo, A. B.; Martínez, J. I.; Rillo, C. *Inorg. Chem.* **2014**, *53*, 12384–12395.
- [111] McKenzie, E.; M. Worthington, J. *Inorg. Chim. Acta* **1976**, *16*, 9–15.
- [112] Yang, L.; Powell, D. R.; Houser, R. P. *Dalton Trans.* **2007**, *96*, 955–964.

- [113] Penkert, F. N.; Weyhermüller, T.; Bill, E.; Hildebrandt, P.; Lecomte, S.; Wieghardt, K. *J. Am. Chem. Soc.* **2000**, *122*, 9663–9673.
- [114] Cowley, R. E.; Bontchev, R. P.; Sorrell, J.; Sarracino, O.; Feng, Y.; Wang, H.; Smith, J. M. *J. Am. Chem. Soc.* **2007**, *129*, 2424–2425.
- [115] Fortier, S.; Le Roy, J. J.; Chen, C. H.; Vieru, V.; Murugesu, M.; Chibotaru, L. F.; Mindiola, D. J.; Caulton, K. G. *J. Am. Chem. Soc.* **2013**, *135*, 14670–14678.
- [116] Lin, C. Y.; Fettinger, J. C.; Grandjean, F.; Long, G. J.; Power, P. P. *Inorg. Chem.* **2014**, *53*, 9400–9406.
- [117] Ingleson, M. J.; Pink, M.; Fan, H.; Caulton, K. G. *Inorg. Chem.* **2007**, *46*, 10321–10334.
- [118] Du, J.; Wang, L.; Xie, M.; Deng, L. *Angew. Chem., Int. Ed.* **2015**, *54*, 12640–12644.
- [119] Zhang, L.; Liu, Y.; Deng, L. *J. Am. Chem. Soc.* **2014**, *136*, 1–26.
- [120] Yao, X.-N.; Du, J.-Z.; Zhang, Y.-Q.; Leng, X.-B.; Yang, M.-W.; Jiang, S.-D.; Wang, Z.-X.; Ouyang, Z.-W.; Deng, L.; Wang, B.-W.; Gao, S. *J. Am. Chem. Soc.* **2017**, *139*, 373–380.
- [121] Hu, X.; Meyer, K. *J. Am. Chem. Soc.* **2004**, *126*, 16322–16323.
- [122] Verani, C. N.; Gallert, S.; Bill, E.; Weyhermüller, T.; Wieghardt, K.; Chaudhuri, P. *Chem. Commun.* **1999**, *38*, 1747–1748.
- [123] Zats, G. M.; Arora, H.; Lavi, R.; Yufit, D.; Benisvy, L. *Dalton Trans.* **2011**, *40*, 10889–10896.
- [124] Bergquist, C.; Fillebeen, T.; Morlok, M. M.; Parkin, G. *J. Am. Chem. Soc.* **2003**, *125*, 6189–6199.
- [125] Chiang, L.; Allan, L. E. N.; Alcantara, J.; Wang, M. C. P.; Storr, T.; Shaver, M. P. *Dalton Trans.* **2014**, *43*, 4295–4304.
- [126] Gorelsky, S. I.; Lever, A. B. P. *J. Organomet. Chem.* **2001**, *635*, 187–196.
- [127] Gorelsky, S. I. AOMix: Program for Molecular Orbital Analysis. 2013; <http://www.sg-chem.net/>.
- [128] Zhu, D.; Janssen, F. F. B. J.; Budzelaar, P. H. M. *Organometallics* **2010**, *29*, 1897–1908.
- [129] Stephens, P. J.; Devlin, F. J.; Chabalowski, C. F.; Frisch, M. J. *J. Phys. Chem.* **1994**, *98*, 11623–11627.
- [130] Vosko, S. H.; Wilk, L.; Nusair, M. *Can. J. Phys.* **1980**, *58*, 1200–1211.

- [131] Lee, C.; Yang, W.; Parr, R. G. *Phys. Rev. B: Condens. Matter Mater. Phys.* **1988**, *37*, 785–789.
- [132] Becke, A. D. *J. Chem. Phys.* **1993**, *98*, 5648–5652.
- [133] Frisch, M. J.; Trucks, G. W.; Schlegel, H. B.; Scuseria, G. E.; Robb, M. A.; Cheeseman, J. R.; Scalmani, G.; Barone, V.; Mennucci, B.; Petersson, G. A.; Nakatsuji, H.; Caricato, M.; Li, X.; Hratchian, H. P.; Izmaylov, A. F.; Bloino, J.; Zheng, G.; Sonnenberg, J. L.; Hada, M.; Ehara, M.; Toyota, K.; Fukuda, R.; Hasegawa, J.; Ishida, M.; Nakajima, T.; Honda, Y.; Kitao, O.; Nakai, H.; Vreven, T.; Montgomery, J. A., Jr.; Peralta, J. E.; Ogliaro, F.; Bearpark, M.; Heyd, J. J.; Brothers, E.; Kudin, K. N.; Staroverov, V. N.; Kobayashi, R.; Normand, J.; Raghavachari, K.; Rendell, A.; Burant, J. C.; Iyengar, S. S.; Tomasi, J.; Cossi, M.; Rega, N.; Millam, J. M.; Klene, M.; Knox, J. E.; Cross, J. B.; Bakken, V.; Adamo, C.; Jaramillo, J.; Gomperts, R.; Stratmann, R. E.; Yazyev, O.; Austin, A. J.; Cammi, R.; Pomelli, C.; Ochterski, J. W.; Martin, R. L.; Morokuma, K.; Zakrzewski, V. G.; Voth, G. A.; Salvador, P.; Dannenberg, J. J.; Dapprich, S.; Daniels, A. D.; Farkas, Ö.; Foresman, J. B.; Ortiz, J. V.; Cioslowski, J.; Fox, D. J. *Gaussian 09, Revision D.01*; Gaussian, Inc.: Wallingford CT, 2013.
- [134] Ik, R. D.; Keith, T.; Millam, J.; Eppinnett, K.; Hovell, I. W.; Gilliland, R. *GaussView 3*; Gaussian, Inc.: Carnegie, PA, 2003.
- [135] Weigend, F.; Ahlrichs, R. *Phys. Chem. Chem. Phys.* **2005**, *7*, 3297.
- [136] Bruker, *APEX2, SAINT, SADABS*; Bruker AXS Inc.: Madison, WI, 2007.
- [137] Farrugia, L. J. *J. Appl. Cryst.* **2012**, *45*, 849–854.
- [138] Dolomanov, O. V.; Bourhis, L. J.; Gildea, R. J.; Howard, J. A. K.; Puschmann, H. *J. Appl. Cryst.* **2009**, *42*, 339–341.
- [139] Sheldrick, G. M. *Acta Crystallogr., Sect. A: Found. Crystallogr.* **1990**, *A46*, 467–473.
- [140] Sheldrick, G. M. *Acta Crystallogr., Sect. C: Struct. Chem.* **2015**, *C71*, 3–8.
- [141] Sheldrick, G. M. *Acta Crystallogr. Sect. A: Found. Crystallogr.* **2008**, *A64*, 112–122.

Appendix

NMR spectra of 2

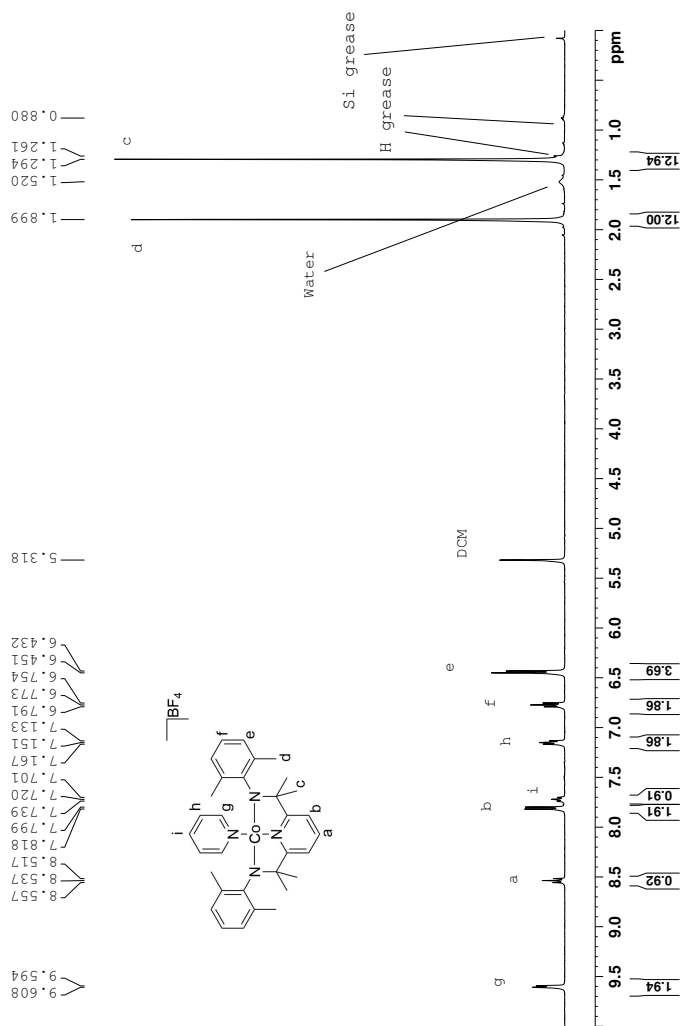


Figure 3.9: ^1H NMR (400 MHz; CD_2Cl_2) spectrum of Complex 2.

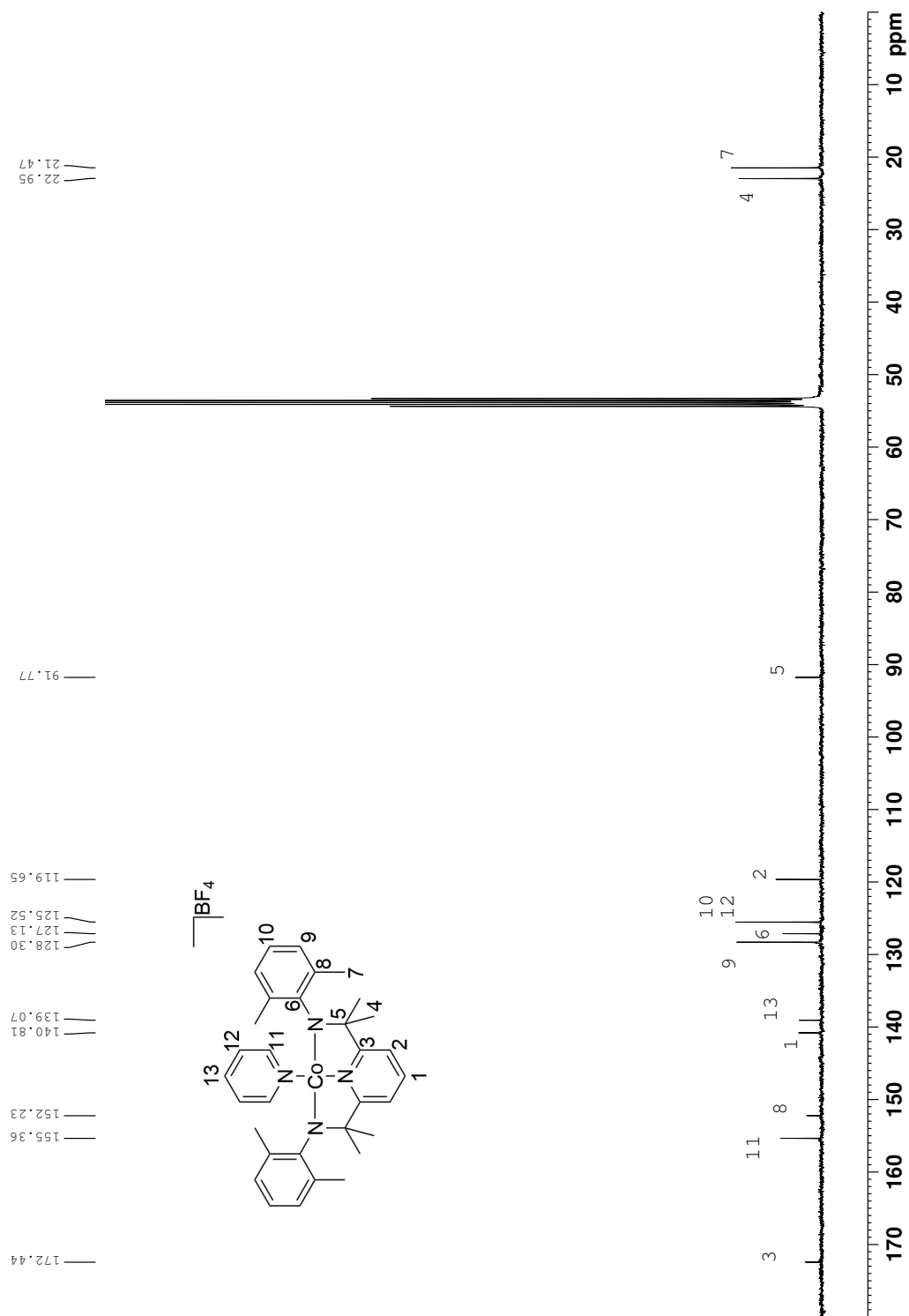


Figure 3.10: ^{13}C NMR (400 MHz; CD_2Cl_2) spectrum of **2**.

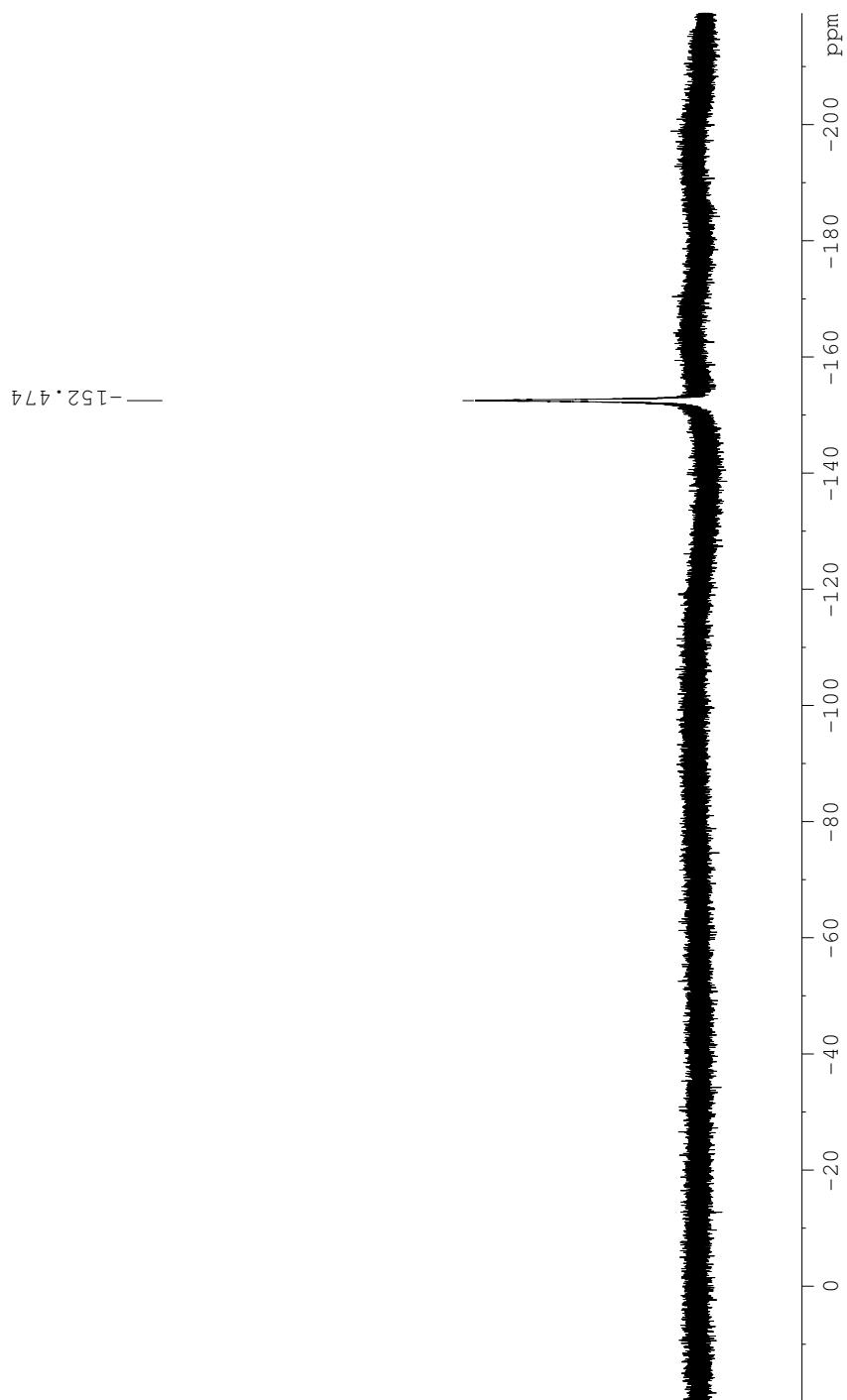


Figure 3.11: ^{19}F NMR (400 MHz; CD_2Cl_2) spectrum of **2**.

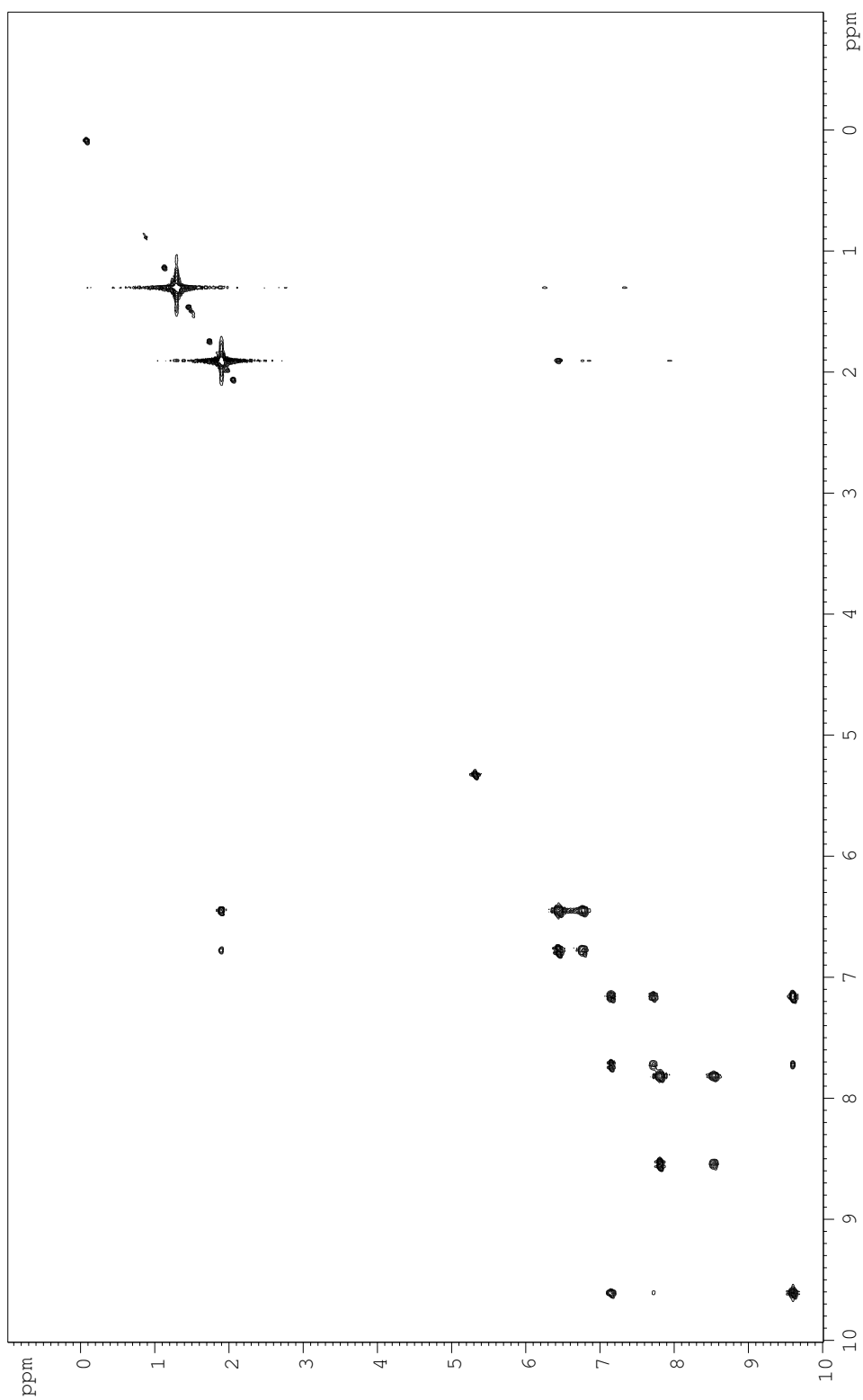


Figure 3.12: ^1H - ^1H COSY (400 MHz; CD_2Cl_2) spectrum of **2**.

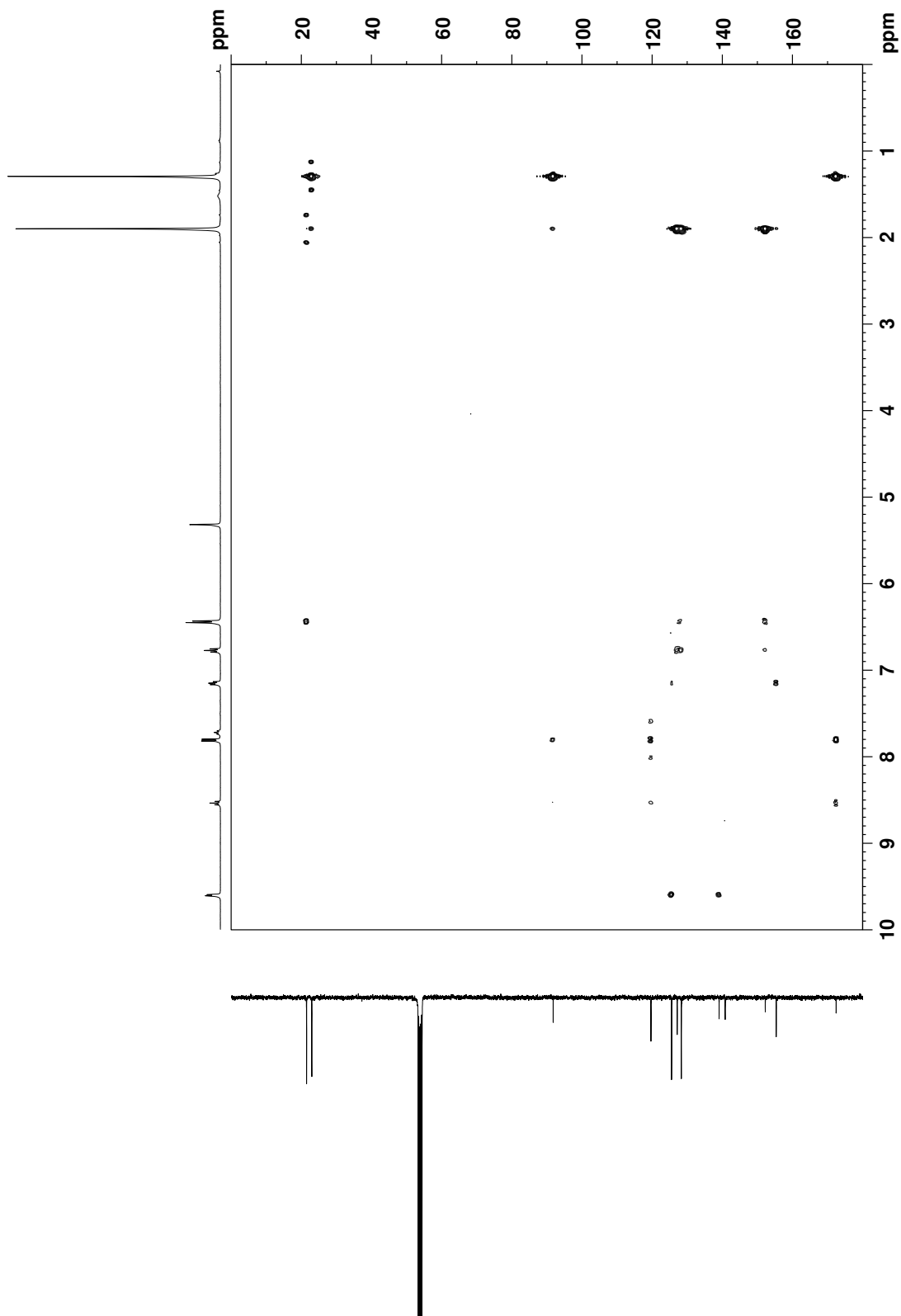


Figure 3.13: ^1H - ^{13}C HMBC (400 MHz; CD_2Cl_2) spectrum of **2**.

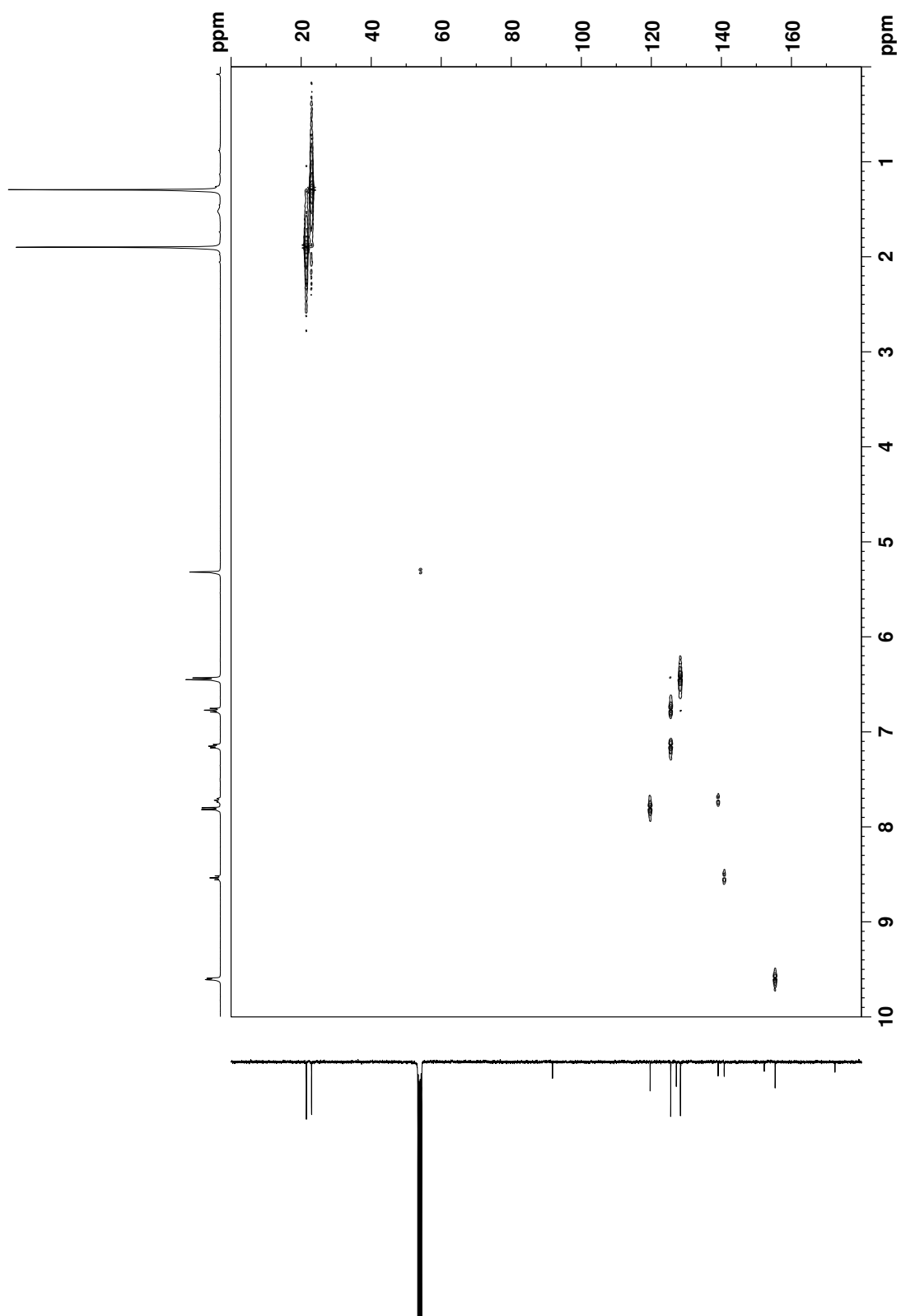


Figure 3.14: ^1H - ^{13}C HSQC (400 MHz; CD_2Cl_2) spectrum of **2**.

X-ray crystallography data of **2**

Table 3.2: Crystal data and structure refinement for complex **2**

Identification code	d16121
Empirical formula	$\text{C}_{32}\text{H}_{38}\text{BCoF}_4\text{N}_4$
Formula weight	624.40
Temperature/K	147.14
Crystal system	monoclinic
Space group	$C2/c$
$a/\text{\AA}$	27.9885(16)
$b/\text{\AA}$	11.9621(8)
$c/\text{\AA}$	19.1699(13)
$\alpha/^\circ$	90
$\beta/^\circ$	105.597(2)
$\gamma/^\circ$	90
Volume/ \AA^3	6181.8(7)
Z	8

ρ_{calc} g/cm ³	1.342
μ /mm ⁻¹	0.607
F(000)	2608.0
Crystal size/mm ³	0.15 × 0.06 × 0.05
Radiation	MoK α (λ = 0.71073)
2 θ range for data collection/°	3.022 to 50.8
Index ranges	-33 ≤ h ≤ 33, -14 ≤ k ≤ 14, -23 ≤ l ≤ 23
Reflections collected	41569
Independent reflections	5689 [R_{int} = 0.0634, R_{sigma} = 0.0449]
Data/restraints/parameters	5689/29/432
Goodness-of-fit on F^2	1.011
Final R indexes [$I \geq 2\sigma(I)$]	R_1 = 0.0492, wR_2 = 0.1094
Final R indexes [all data]	R_1 = 0.0887, wR_2 = 0.1297
Largest diff. peak/hole / e Å ⁻³	0.60/-0.48

Table 3.3: Fractional Atomic Coordinates ($\times 10^4$) and Equivalent Isotropic Displacement Parameters ($\text{\AA}^2 \times 10^3$) for complex **2**. U_{eq} is defined as 1/3 of the trace of the orthogonalised U_{IJ} tensor.

Atom	x	y	z	$U(eq)$
Co1	8758.7(2)	1752.6(4)	7822.8(2)	36.72(15)
N2	8280.9(10)	1960(3)	7001.3(15)	47.1(8)
N1	8808.7(9)	354(2)	7463.9(14)	38.7(7)
N3	9252.8(9)	1298(2)	8577.2(13)	29.9(6)
N4	8699.6(10)	3215(3)	8226.3(16)	44.0(7)
C1	8498.1(12)	69(3)	6823.4(18)	45.5(9)
C2	8513.0(14)	-1003(4)	6554(2)	55.3(11)
C3	8850.1(14)	-1753(4)	6953(2)	56.7(10)
C4	9170.9(14)	-1443(3)	7611(2)	50.2(10)
C5	9139.7(12)	-372(3)	7861.5(17)	38.3(8)
C6	8165.6(13)	1007(4)	6466.4(19)	53(1)
C7	8273.9(17)	1298(4)	5741(2)	75.6(14)
C8	7622.8(14)	628(4)	6317(3)	76.1(15)
C9	9445.8(11)	127(3)	8562.6(17)	35.0(8)

C10	9376.4(13)	-586(3)	9196.3(18)	44.3(9)
C11	9995.9(12)	106(3)	8574.5(19)	48.1(10)
C12	7975.6(13)	2936(4)	6793(2)	58.1(12)
C13	8117.5(17)	3777(4)	6379(2)	75.8(14)
C14	7801(2)	4680(5)	6154(3)	100(2)
C15	7363(3)	4758(6)	6336(3)	122(3)
C16	7240.8(18)	3977(6)	6775(3)	104(2)
C17	7542.7(15)	3046(4)	7022(2)	71.2(14)
C18	8606.3(18)	3788(4)	6190(3)	85.0(15)
C19	7397.9(16)	2244(5)	7534(3)	83.7(17)
C20	9505.2(10)	1977(3)	9182.1(15)	29.7(7)
C21	9336.8(12)	2009(3)	9812.9(17)	37.7(8)
C22	9576.0(17)	2741(3)	10366(2)	61.3(12)
C23	9955(2)	3423(4)	10303(3)	76.7(16)
C24	10099.9(15)	3405(3)	9683(3)	68.8(14)
C25	9885.3(12)	2699(3)	9112(2)	45.3(9)
C26	8905.0(14)	1348(3)	9905(2)	55.2(11)
C27	10045.3(14)	2778(4)	8425(2)	70.8(14)

C28	8455.2(13)	3334(3)	8741(2)	50.7(10)
C29	8454.5(16)	4331(4)	9102(2)	70.1(14)
C30	8697.3(19)	5241(4)	8919(3)	90(2)
C31	8929.3(18)	5135(4)	8379(3)	84.3(17)
C32	8930.3(14)	4116(4)	8057(3)	64.8(12)
F1	9706(4)	4863(6)	12155(7)	197(7)
F2	9738(3)	3670(7)	13027(4)	148(4)
F3	10429(3)	4345(7)	12853(5)	114(3)
F4	9962(2)	3167(5)	12068(3)	97(2)
B1	9946(12)	4013(6)	12560(20)	36(5)
F5	7776.7(15)	1669(4)	9844(2)	54.6(11)
F6	7409.7(15)	2306(4)	10675(2)	56.5(11)
F7	7444(2)	3421(4)	9752(3)	68.3(16)
F8	8063.0(12)	3070(3)	10480(2)	49.8(10)
B2	7599(4)	2672(11)	10051(7)	32(2)

Table 3.4: Anisotropic Displacement Parameters ($\text{\AA}^2 \times 10^3$) for complex **2**. The Anisotropic displacement factor exponent takes the form: $-2\pi^2[h^2a^{*2}U_{11}+2hka^*b^*U_{12}+]$.

Atom	U11	U22	U33	U23	U13	U12
Co1	25.3(2)	47.6(3)	30.3(2)	-3.1(2)	-4.52(17)	6.4(2)
N2	30.1(15)	67(2)	35.3(16)	-4.4(15)	-7.2(12)	8.5(14)
N1	28.5(14)	56.5(18)	29.4(15)	-9.4(13)	5.1(11)	4.2(13)
N3	22.6(13)	40.9(15)	24.8(13)	-0.1(12)	4.1(10)	2.6(11)
N4	30.7(15)	44.0(17)	44.2(17)	-1.4(15)	-12.4(13)	7.7(14)
C1	28.9(18)	72(3)	33.4(19)	-12.5(18)	4.6(15)	3.1(17)
C2	42(2)	82(3)	41(2)	-29(2)	9.6(17)	-3(2)
C3	57(2)	64(3)	53(2)	-23(2)	20(2)	1(2)
C4	47(2)	56(2)	48(2)	-13.4(18)	12.8(18)	7.7(18)
C5	31.6(17)	51(2)	32.0(18)	-4.5(16)	7.6(14)	6.8(16)
C6	34.2(19)	80(3)	35(2)	-17(2)	-7.7(15)	5.4(19)
C7	76(3)	108(4)	34(2)	-4(2)	-1(2)	20(3)
C8	35(2)	102(4)	75(3)	-38(3)	-12(2)	8(2)
C9	29.5(17)	43.1(19)	31.7(17)	-2.8(15)	7.3(14)	10.0(14)
C10	50(2)	42(2)	38(2)	2.7(16)	8.9(16)	10.8(17)

C11	29.7(18)	76(3)	36(2)	-5.5(19)	4.6(15)	13.6(18)
C12	35(2)	82(3)	41(2)	-4(2)	-16.5(17)	25(2)
C13	64(3)	89(3)	58(3)	10(3)	-11(2)	38(3)
C14	98(4)	111(4)	72(3)	22(3)	-9(3)	60(4)
C15	109(5)	151(6)	76(4)	-8(4)	-30(4)	95(5)
C16	53(3)	170(6)	66(3)	-37(4)	-25(3)	59(4)
C17	36(2)	112(4)	50(2)	-26(3)	-16.3(19)	25(2)
C18	74(3)	91(4)	83(4)	26(3)	9(3)	18(3)
C19	44(3)	137(5)	64(3)	-45(3)	5(2)	-2(3)
C20	22.0(15)	38.2(19)	24.1(16)	3.3(13)	-2.1(12)	4.4(13)
C21	44(2)	38.2(19)	27.8(17)	4.8(14)	4.9(15)	16.1(15)
C22	90(3)	50(2)	31(2)	-5.4(18)	-5(2)	32(2)
C23	92(4)	38(2)	64(3)	-12(2)	-39(3)	11(2)
C24	49(2)	45(3)	85(4)	12(2)	-28(2)	-8.8(19)
C25	27.0(18)	49(2)	51(2)	15.0(18)	-4.5(16)	-3.4(16)
C26	60(2)	65(3)	55(2)	14(2)	39(2)	22(2)
C27	37(2)	89(3)	87(3)	41(3)	18(2)	-6(2)
C28	43(2)	50(2)	44(2)	-9.3(19)	-12.7(17)	15.1(18)

C29	65(3)	65(3)	60(3)	-26(2)	-20(2)	30(2)
C30	73(3)	48(3)	110(5)	-36(3)	-41(3)	23(3)
C31	64(3)	47(3)	115(5)	-11(3)	-23(3)	6(2)
C32	42(2)	55(3)	80(3)	3(2)	-13(2)	4(2)
F1	215(14)	86(6)	235(12)	107(7)	-35(9)	9(6)
F2	159(8)	199(9)	118(6)	-85(6)	95(6)	-65(7)
F3	55(4)	148(8)	144(7)	-63(6)	38(4)	-34(5)
F4	103(5)	109(5)	67(4)	-55(4)	3(3)	37(4)
B1	39(13)	35(4)	46(11)	0(6)	30(7)	-1(5)
F5	40(2)	72(3)	51(3)	-13(3)	11(2)	4(2)
F6	72(3)	65(3)	37(2)	9(2)	24(2)	17(2)
F7	85(4)	48(3)	51(3)	24(3)	-18(3)	-23(3)
F8	33(2)	41(2)	71(3)	-15(2)	8(2)	-0.7(17)
B2	27(8)	44(8)	22(5)	-7(5)	2(6)	7(5)

Table 3.5: Bond Lengths for complex **2**.

Atom	Atom	Length/Å	Atom	Atom	Length/Å
Co1	N2	1.788(3)	C13	C18	1.507(7)
Co1	N1	1.829(3)	C14	C15	1.364(9)
Co1	N3	1.796(2)	C15	C16	1.360(9)
Co1	N4	1.938(3)	C16	C17	1.401(7)
N2	C6	1.510(5)	C17	C19	1.505(7)
N2	C12	1.439(5)	C20	C21	1.412(4)
N1	C1	1.344(4)	C20	C25	1.404(4)
N1	C5	1.346(4)	C21	C22	1.399(5)
N3	C9	1.505(4)	C21	C26	1.493(5)
N3	C20	1.437(4)	C22	C23	1.369(7)
N4	C28	1.351(5)	C23	C24	1.356(7)
N4	C32	1.340(5)	C24	C25	1.384(6)
C1	C2	1.387(5)	C25	C27	1.505(6)
C1	C6	1.500(5)	C28	C29	1.380(5)
C2	C3	1.376(6)	C29	C30	1.377(7)

C3	C4	1.387(5)	C30	C31	1.368(8)
C4	C5	1.380(5)	C31	C32	1.366(6)
C5	C9	1.509(4)	F1	B1	1.34(3)
C6	C7	1.541(6)	F2	B1	1.26(2)
C6	C8	1.537(5)	F3	B1	1.38(3)
C9	C10	1.539(5)	F4	B1	1.39(2)
C9	C11	1.534(4)	F5	B2	1.397(14)
C12	C13	1.403(7)	F6	B2	1.498(14)
C12	C17	1.401(6)	F7	B2	1.090(14)
C13	C14	1.390(6)	F8	B2	1.420(8)

Table 3.6: Bond Angles for complex **2**.

Atom	Atom	Atom	Angle/ °	Atom	Atom	Atom	Angle/ °
N2	Co1	N1	84.86(13)	C17	C12	N2	119.2(4)
N2	Co1	N3	169.42(13)	C17	C12	C13	120.7(4)
N2	Co1	N4	95.87(12)	C12	C13	C18	123.7(4)
N1	Co1	N4	178.33(13)	C14	C13	C12	118.6(5)
N3	Co1	N1	84.58(12)	C14	C13	C18	117.6(5)
N3	Co1	N4	94.70(11)	C15	C14	C13	121.0(6)
C6	N2	Co1	117.8(2)	C16	C15	C14	120.2(5)
C12	N2	Co1	127.2(2)	C15	C16	C17	121.7(6)
C12	N2	C6	115.0(3)	C12	C17	C16	117.5(5)
C1	N1	Co1	118.7(2)	C12	C17	C19	123.5(4)
C1	N1	C5	122.1(3)	C16	C17	C19	118.9(5)
C5	N1	Co1	119.2(2)	C21	C20	N3	120.1(3)
C9	N3	Co1	118.01(19)	C25	C20	N3	119.5(3)
C20	N3	Co1	125.7(2)	C25	C20	C21	120.1(3)
C20	N3	C9	116.2(2)	C20	C21	C26	123.7(3)

C28	N4	Co1	120.0(3)	C22	C21	C20	117.7(3)
C32	N4	Co1	122.1(3)	C22	C21	C26	118.6(3)
C32	N4	C28	117.7(4)	C23	C22	C21	122.0(4)
N1	C1	C2	119.8(3)	C24	C23	C22	119.3(4)
N1	C1	C6	113.4(3)	C23	C24	C25	122.3(4)
C2	C1	C6	126.8(3)	C20	C25	C27	122.2(3)
C3	C2	C1	118.8(3)	C24	C25	C20	118.6(4)
C2	C3	C4	120.7(4)	C24	C25	C27	119.0(4)
C5	C4	C3	118.6(4)	N4	C28	C29	121.8(4)
N1	C5	C4	120.0(3)	C30	C29	C28	119.2(5)
N1	C5	C9	112.9(3)	C31	C30	C29	119.1(5)
C4	C5	C9	127.1(3)	C32	C31	C30	119.0(5)
N2	C6	C7	112.6(4)	N4	C32	C31	123.2(5)
N2	C6	C8	111.7(3)	F1	B1	F3	107.5(10)
C1	C6	N2	105.2(3)	F1	B1	F4	105(3)
C1	C6	C7	109.4(3)	F2	B1	F1	113.7(18)
C1	C6	C8	109.0(4)	F2	B1	F3	113(3)
C8	C6	C7	108.8(3)	F2	B1	F4	110.5(10)

N3	C9	C5	105.3(2)	F3	B1	F4	106.2(15)
N3	C9	C10	112.3(2)	F5	B2	F6	101.9(9)
N3	C9	C11	112.2(3)	F5	B2	F8	96.4(8)
C5	C9	C10	108.8(3)	F7	B2	F5	132.7(12)
C5	C9	C11	109.5(3)	F7	B2	F6	119.0(11)
C11	C9	C10	108.6(3)	F7	B2	F8	101.6(7)
C13	C12	N2	120.1(4)	F8	B2	F6	95.8(8)

NMR spectra of 3a

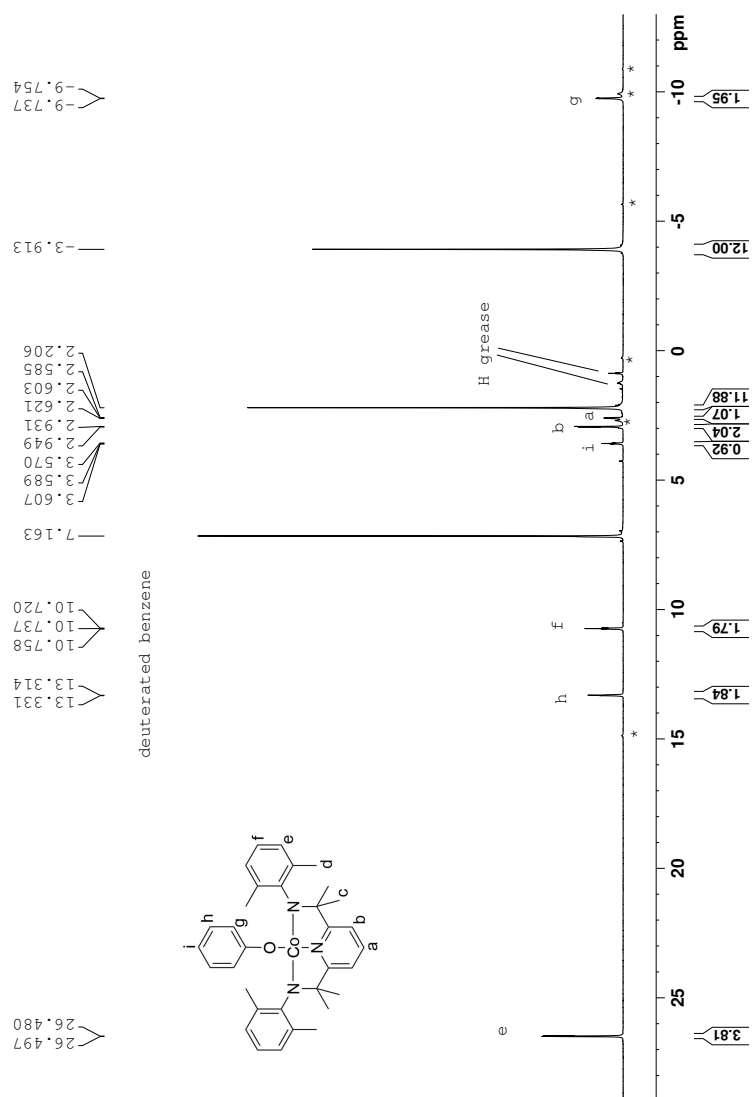


Figure 3.15: ^1H NMR (400 MHz; C_6D_6) spectrum of Complex 3a.

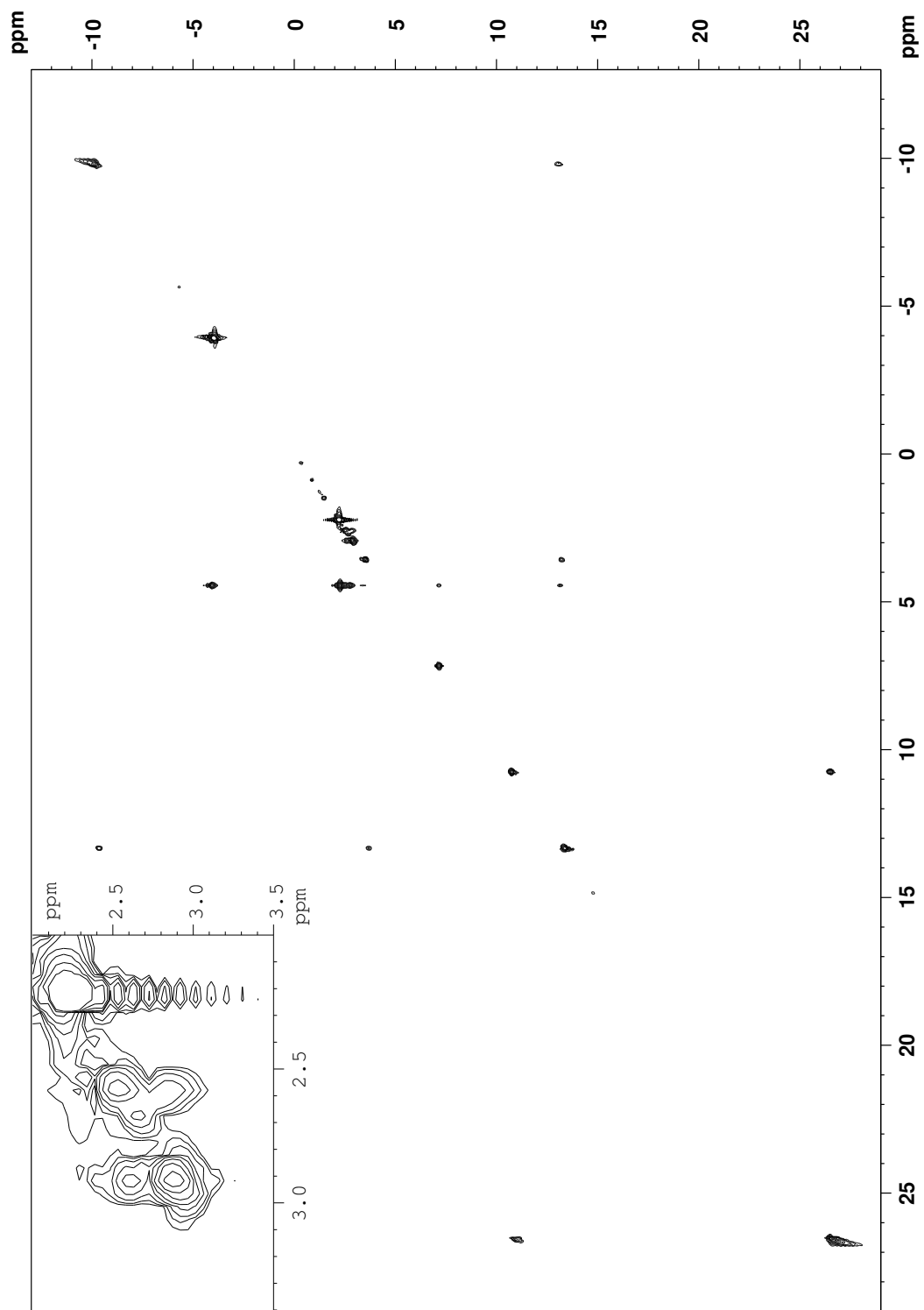


Figure 3.16: ^1H - ^1H COSY (400 MHz; C_6D_6) spectrum of **3a**.

X-ray crystallography of **3a**

Table 3.7: Crystal data and structure refinement for complex **3a**.

Identification code	d1741_sq
Empirical formula	C ₃₄ H ₄₀ Cl ₂ CoN ₃ O
Formula weight	636.52
Temperature/K	150(2)
Crystal system	monoclinic
Space group	P2 ₁ / <i>n</i>
<i>a</i> /Å	12.7562(8)
<i>b</i> /Å	18.4663(14)
<i>c</i> /Å	14.9532(10)
α /°	90
β /°	98.221(2)
γ /°	90
Volume/Å ³	3486.2(4)
<i>Z</i>	4

ρ_{calc} g/cm ³	1.213
μ /mm ⁻¹	0.674
F(000)	1336.0
Crystal size/mm ³	0.270 × 0.260 × 0.250
Radiation	MoK α (λ = 0.71073)
2 θ range for data collection/°	3.526 to 55.058
Index ranges	-14 ≤ h ≤ 16, -24 ≤ k ≤ 24, -19 ≤ l ≤ 18
Reflections collected	44730
Independent reflections	8029 [R_{int} = 0.0615, R_{sigma} = 0.0560]
Data/restraints/parameters	8029/0/379
Goodness-of-fit on F^2	1.025
Final R indexes [$I \geq 2\sigma(I)$]	R_1 = 0.0497, wR_2 = 0.1254
Final R indexes [all data]	R_1 = 0.0883, wR_2 = 0.1446
Largest diff. peak/hole / e Å ⁻³	0.60/-0.95

Table 3.8: Fractional Atomic Coordinates ($\times 10^4$) and Equivalent Isotropic Displacement Parameters ($\text{\AA}^2 \times 10^3$) for complex **3a**. U_{eq} is defined as 1/3 of the trace of the orthogonalised U_{IJ} tensor.

Atom	x	y	z	$U(eq)$
Co1	2560.9(3)	3068.5(2)	2994.5(2)	19.11(11)
O1	1628.2(14)	3447.4(10)	2001.7(12)	22.2(4)
N1	3476.8(17)	2665.7(12)	3912.8(14)	21.6(5)
N2	3716.4(17)	3201.7(11)	2462.1(14)	21.1(5)
N3	1550.9(17)	2788.9(12)	3643.1(14)	22.8(5)
C1	4517(2)	2675.1(14)	3854.1(18)	23.3(6)
C2	5231(2)	2409.0(16)	4567.2(19)	29.4(6)
C3	4853(2)	2121.8(16)	5317.4(19)	30.1(7)
C4	3769(2)	2089.2(15)	5336.3(18)	28.9(6)
C5	3091(2)	2368.9(15)	4615.5(17)	25.1(6)
C6	4768(2)	2961.4(15)	2962.7(18)	24.2(6)
C7	5252(2)	2341.5(16)	2475(2)	30.5(6)
C8	5564(2)	3582.9(17)	3128(2)	36.1(7)
C9	1893(2)	2361.6(17)	4494.8(18)	29.9(6)

C10	1531(3)	1567.6(19)	4391(3)	48.4(10)
C11	1498(3)	2689(3)	5328(2)	58.1(12)
C12	3729(2)	3430.4(15)	1540.4(18)	24.3(6)
C13	3454(2)	2935.1(16)	836.1(19)	29.5(6)
C14	3475(3)	3160.3(19)	-55(2)	41.0(8)
C15	3738(3)	3861(2)	-245(2)	50.4(10)
C16	3952(3)	4350.3(19)	441(2)	44.9(9)
C17	3937(2)	4151.3(16)	1342(2)	32.5(7)
C18	3092(3)	2172.4(17)	991(2)	39.3(8)
C19	4076(3)	4746.3(17)	2046(3)	44.5(8)
C20	431(2)	2818.6(15)	3352.0(18)	24.4(6)
C21	-38(2)	2310.3(15)	2717.7(19)	29.0(6)
C22	-1135(2)	2336.5(19)	2457(2)	37.9(8)
C23	-1739(2)	2869(2)	2767(2)	42.7(9)
C24	-1273(2)	3386(2)	3352(2)	40.0(8)
C25	-190(2)	3375.4(16)	3660(2)	30.1(6)
C26	589(3)	1761.5(16)	2273(2)	38.8(8)
C27	250(3)	3968.9(19)	4290(2)	44.6(8)

C28	1503(2)	4157.5(15)	1889.4(18)	24.0(6)
C29	1577(3)	4643.5(16)	2609(2)	35.1(7)
C30	1430(3)	5387.6(18)	2459(2)	46.0(9)
C31	1206(3)	5657.6(18)	1602(2)	45.2(9)
C32	1134(3)	5185.4(18)	879(2)	41.2(8)
C33	1282(2)	4449.4(17)	1014(2)	33.7(7)
Cl1S	2440.8(11)	420.3(6)	6575.4(9)	79.8(4)
Cl2S	3482.2(13)	-592.8(7)	7883.0(11)	98.1(5)
C1S	3601(4)	-60(3)	6930(4)	87.4(16)

Table 3.9: Anisotropic Displacement Parameters ($\text{\AA}^2 \times 10^3$) for complex **3a**. The Anisotropic displacement factor exponent takes the form: $-2\pi^2[h^2a^{*2}U_{11}+2hka^*b^*U_{12}+]$.

Co1	15.34(18)	24.84(19)	17.06(19)	0.33(14)	2.04(13)	0.48(14)
O1	20.3(9)	24.7(10)	20.7(10)	1.2(7)	-0.1(7)	-0.8(8)
N1	18.6(11)	28.1(12)	17.9(11)	-2.0(9)	2.3(9)	1.5(9)
N2	17.9(11)	24.7(12)	20.3(11)	-2.2(9)	1.0(9)	-1.2(9)
N3	17.8(11)	31.4(12)	19.4(11)	2.4(9)	3.1(9)	3.6(9)
C1	18.2(13)	25.7(14)	24.7(14)	-6.6(11)	-1.1(10)	1.5(11)
C2	19.5(14)	36.2(16)	30.4(16)	-7.5(12)	-3.1(11)	2.7(12)
C3	28.4(15)	37.5(16)	21.2(15)	-5.0(12)	-7.6(11)	10.8(13)
C4	33.0(16)	34.7(16)	18.3(14)	1.4(11)	1.6(11)	7.2(13)
C5	23.1(14)	34.2(15)	17.6(13)	-1.0(11)	1.5(11)	3.0(12)
C6	15.6(13)	30.3(15)	26.9(15)	-3.0(11)	3.7(10)	-0.2(11)
C7	24.5(15)	39.5(17)	29.2(16)	-2.8(12)	9.6(12)	4.3(13)
C8	21.1(15)	38.7(17)	47.5(19)	-2.7(14)	1.4(13)	-5.8(13)
C9	22.6(14)	46.8(18)	20.8(14)	12.3(12)	4.3(11)	7.3(13)
C10	32.1(18)	55(2)	55(2)	35.2(18)	-5.6(15)	-5.3(16)
C11	36.3(19)	115(4)	24.8(18)	13.0(19)	11.5(14)	33(2)

C12	20.3(14)	28.1(14)	26.1(14)	2.2(11)	9.0(11)	2.1(11)
C13	35.7(16)	32.8(16)	20.5(14)	1.5(11)	5.9(12)	10.1(13)
C14	47(2)	53(2)	24.1(16)	2.0(14)	11.8(14)	19.7(16)
C15	55(2)	66(2)	37(2)	22.8(18)	28.4(17)	28.9(19)
C16	44(2)	41.2(19)	56(2)	24.1(17)	28.4(17)	10.7(16)
C17	26.4(15)	30.2(15)	43.6(18)	5.3(13)	14.7(13)	2.9(12)
C18	49(2)	36.7(17)	30.6(17)	-10.2(13)	-1.2(14)	-2.0(15)
C19	37.7(19)	26.0(16)	72(2)	-1.7(15)	14.0(17)	-4.3(14)
C20	17.8(13)	29.2(14)	26.7(15)	10.3(11)	5.1(11)	-0.2(11)
C21	27.4(15)	30.7(15)	28.4(16)	12.5(12)	2.5(12)	-4.1(12)
C22	32.4(17)	52(2)	28.2(16)	10.8(14)	-1.1(13)	-13.5(15)
C23	18.9(15)	74(2)	35.4(18)	18.2(17)	4.9(13)	-2.0(16)
C24	27.5(17)	55(2)	39.8(19)	15.6(16)	11.9(14)	13.0(15)
C25	23.4(15)	37.5(16)	31.0(16)	10.3(13)	9.6(12)	3.3(13)
C26	47(2)	30.4(16)	37.0(18)	0.6(13)	-0.5(15)	-2.2(14)
C27	45(2)	46(2)	46(2)	-4.2(16)	17.1(16)	4.6(16)
C28	18.0(13)	26.2(14)	27.4(15)	3.0(11)	1.4(11)	0.8(11)
C29	44.3(19)	32.8(16)	28.9(16)	0.3(12)	7.5(14)	3.9(14)

C30	58(2)	35.5(18)	46(2)	-6.1(15)	15.6(17)	7.1(16)
C31	52(2)	27.1(16)	59(2)	10.5(15)	17.5(17)	10.2(15)
C32	42.9(19)	38.7(18)	41.1(19)	16.1(15)	3.2(15)	1.6(15)
C33	33.6(17)	36.6(17)	29.8(16)	4.3(13)	0.5(13)	-2.4(13)
Cl1S	95.0(9)	60.3(7)	75.8(8)	-11.0(6)	-16.8(6)	-0.8(6)
Cl2S	114.8(12)	71.4(8)	114.8(12)	28.4(8)	39.6(9)	13.8(8)
C1S	78(3)	103(4)	91(4)	13(3)	43(3)	15(3)

Table 3.10: Bond Lengths for complex**3a**.

Atom	Atom	Length/Å	Atom	Atom	Length/Å
Co1	N2	1.790(2)	C13	C14	1.400(4)
Co1	N3	1.796(2)	C13	C18	1.510(4)
Co1	N1	1.829(2)	C14	C15	1.376(5)
Co1	O1	1.8984(17)	C15	C16	1.365(5)
O1	C28	1.329(3)	C16	C17	1.400(4)
N1	C5	1.339(3)	C17	C19	1.515(5)
N1	C1	1.342(3)	C20	C21	1.406(4)
N2	C12	1.444(3)	C20	C25	1.414(4)
N2	C6	1.506(3)	C21	C22	1.398(4)
N3	C20	1.434(3)	C21	C26	1.504(4)
N3	C9	1.509(3)	C22	C23	1.370(5)
C1	C2	1.389(4)	C23	C24	1.373(5)
C1	C6	1.510(4)	C24	C25	1.393(4)
C2	C3	1.388(4)	C25	C27	1.500(5)
C3	C4	1.387(4)	C28	C29	1.394(4)

C4	C5	1.382(4)	C28	C33	1.406(4)
C5	C9	1.513(4)	C29	C30	1.401(4)
C6	C8	1.529(4)	C30	C31	1.366(5)
C6	C7	1.533(4)	C31	C32	1.382(5)
C9	C11	1.533(4)	C32	C33	1.383(4)
C9	C10	1.538(5)	C11S	C1S	1.741(5)
C12	C17	1.398(4)	C12S	C1S	1.757(5)
C12	C13	1.401(4)			

Table 3.11: Bond Angles for complex **3a**.

Atom	Atom	Atom	Angle/ °	Atom	Atom	Atom	Angle/ °
N2	Co1	N3	168.52(10)	C5	C9	C10	107.7(2)
N2	Co1	N1	84.93(10)	C11	C9	C10	109.2(3)
N3	Co1	N1	84.73(10)	C17	C12	C13	119.8(3)
N2	Co1	O1	93.75(9)	C17	C12	N2	120.6(2)
N3	Co1	O1	96.35(9)	C13	C12	N2	119.4(2)
N1	Co1	O1	177.03(9)	C12	C13	C14	119.0(3)
C28	O1	Co1	120.86(16)	C12	C13	C18	122.9(3)
C5	N1	C1	122.3(2)	C14	C13	C18	118.1(3)
C5	N1	Co1	119.26(18)	C15	C14	C13	120.9(3)
C1	N1	Co1	118.48(18)	C16	C15	C14	119.8(3)
C12	N2	C6	115.5(2)	C15	C16	C17	121.4(3)
C12	N2	Co1	125.95(17)	C12	C17	C16	118.9(3)
C6	N2	Co1	118.03(16)	C12	C17	C19	123.4(3)
C20	N3	C9	115.6(2)	C16	C17	C19	117.6(3)
C20	N3	Co1	125.86(17)	C21	C20	C25	120.1(3)

C9	N3	Co1	117.59(17)	C21	C20	N3	119.3(2)
N1	C1	C2	119.4(3)	C25	C20	N3	120.6(3)
N1	C1	C6	113.5(2)	C22	C21	C20	118.5(3)
C2	C1	C6	127.1(2)	C22	C21	C26	118.3(3)
C3	C2	C1	119.3(3)	C20	C21	C26	123.1(3)
C4	C3	C2	119.7(3)	C23	C22	C21	121.3(3)
C5	C4	C3	118.8(3)	C22	C23	C24	120.2(3)
N1	C5	C4	120.4(3)	C23	C24	C25	121.3(3)
N1	C5	C9	112.8(2)	C24	C25	C20	118.5(3)
C4	C5	C9	126.8(3)	C24	C25	C27	117.4(3)
N2	C6	C1	104.8(2)	C20	C25	C27	124.0(3)
N2	C6	C8	112.5(2)	O1	C28	C29	123.0(2)
C1	C6	C8	109.9(2)	O1	C28	C33	120.0(2)
N2	C6	C7	112.0(2)	C29	C28	C33	117.0(3)
C1	C6	C7	108.0(2)	C28	C29	C30	121.0(3)
C8	C6	C7	109.5(2)	C31	C30	C29	120.9(3)
N3	C9	C5	105.1(2)	C30	C31	C32	119.0(3)
N3	C9	C11	113.0(2)	C31	C32	C33	120.9(3)

C5	C9	C11	110.1(3)	C32	C33	C28	121.2(3)
----	----	-----	----------	-----	-----	-----	----------

N3	C9	C10	111.5(2)	Cl1S	C1S	Cl2S	111.3(3)
----	----	-----	----------	------	-----	------	----------

NMR spectrum of 3b

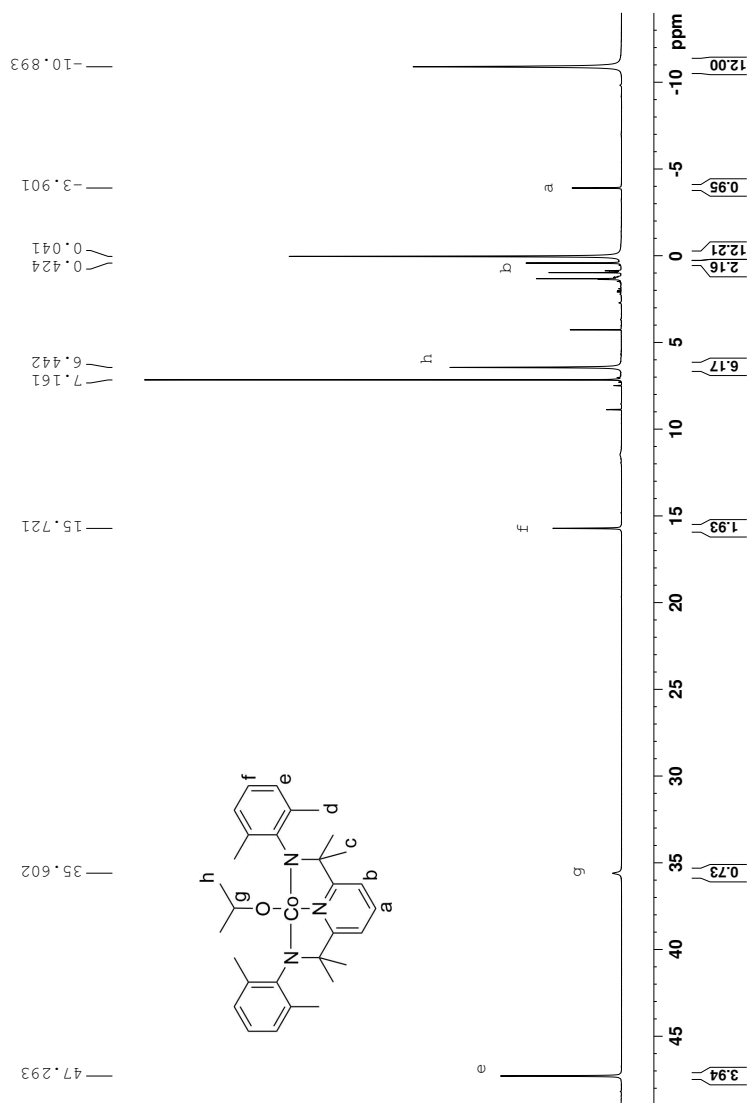


Figure 3.17: ¹H NMR (400 MHz; C₆D₆) spectrum of Complex 3b.

NMR spectrum of 4

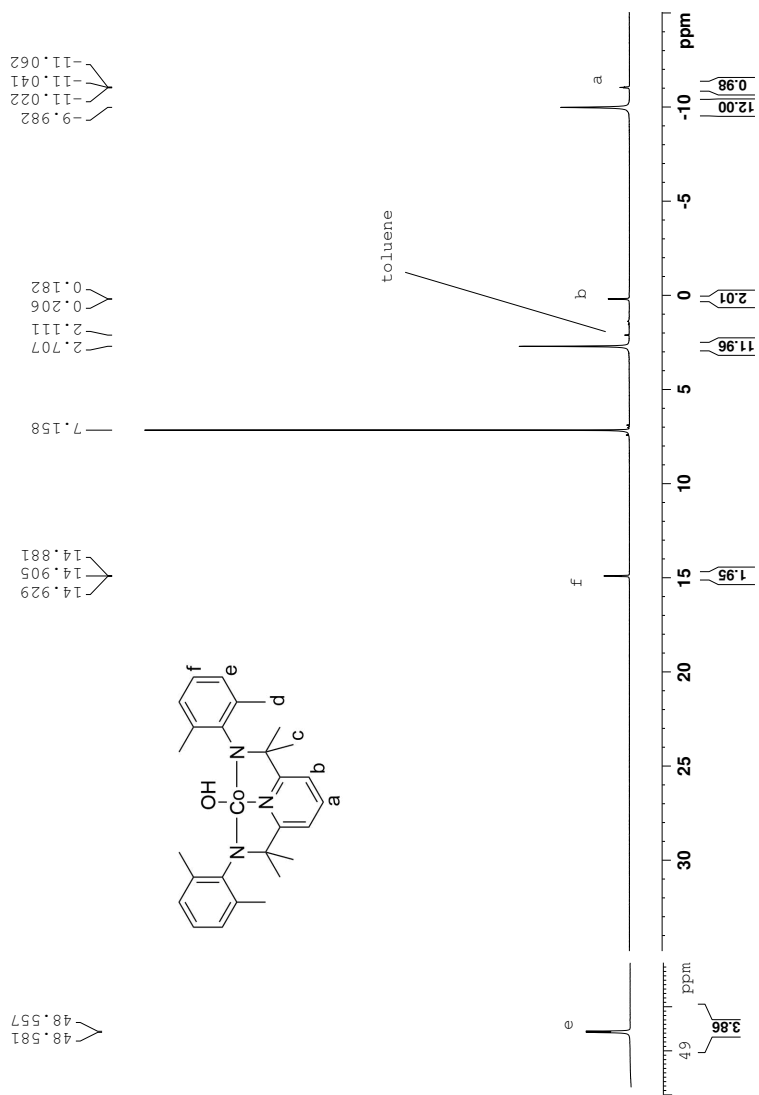


Figure 3.18: ^1H NMR (400 MHz; C_6D_6) spectrum of Complex 4.

X-ray crystallography data of 4

Table 3.12: Crystal data and structure refinement for complex 4.

Identification code	d1785
Empirical formula	$\text{C}_{28}\text{H}_{36}\text{Cl}_2\text{CoN}_3\text{O}$
Formula weight	560.43
Temperature/K	99.6
Crystal system	monoclinic
Space group	$\text{P}2_1/n$
$a/\text{\AA}$	8.6720(5)
$b/\text{\AA}$	14.1009(8)
$c/\text{\AA}$	22.5819(15)
$\alpha/^\circ$	90
$\beta/^\circ$	98.143(2)
$\gamma/^\circ$	90
Volume/ \AA^3	2745.5(3)
Z	4

ρ_{calc} g/cm ³	1.256
μ /mm ⁻¹	0.845
F(000)	1176.0
Crystal size/mm ³	0.2 × 0.18 × 0.08
Radiation	MoK α (λ = 0.71073)
2 θ range for data collection/°	3.41 to 55.058
Index ranges	-10 ≤ h ≤ 11, -18 ≤ k ≤ 18, -29 ≤ l ≤ 29
Reflections collected	40793
Independent reflections	6331 [R_{int} = 0.04463, R_{sigma} = 0.0343]
Data/restraints/parameters	6331/0/328
Goodness-of-fit on F^2	1.021
Final R indexes [$I \geq 2\sigma(I)$]	R_1 = 0.0363, wR_2 = 0.0789
Final R indexes [all data]	R_1 = 0.0544, wR_2 = 0.0872
Largest diff. peak/hole / e Å ⁻³	0.88/-0.74

Table 3.13: Fractional Atomic Coordinates ($\times 10^4$) and Equivalent Isotropic Displacement Parameters ($\text{\AA}^2 \times 10^3$) for complex **3a**. U_{eq} is defined as 1/3 of the trace of the orthogonalised U_{IJ} tensor.

Atom	x	y	z	$U(eq)$
Co1	5445.8(3)	7795.0(2)	647.6(2)	9.96(7)
O1	3475.1(17)	7433.3(12)	685.9(7)	19.7(3)
N2	5379.1(18)	7883.0(11)	-166.0(7)	11.1(3)
N1	7515.4(18)	8127.3(11)	638.0(7)	11.3(3)
N3	5934.4(18)	7809.0(12)	1460.5(7)	11.9(3)
C6	6878(2)	8053.4(14)	-420.1(9)	12.9(4)
C5	8059(2)	8258.3(13)	106.8(9)	12.5(4)
C4	9581(2)	8538.6(15)	87.2(9)	16.8(4)
C3	10511(2)	8676.7(15)	620.6(10)	18.4(4)
C2	9925(2)	8527.4(15)	1161.2(9)	17.5(4)
C1	8396(2)	8247.3(14)	1160.3(9)	13.2(4)
C9	7552(2)	8051.4(14)	1699.7(9)	13.8(4)
C8	6795(2)	8902.2(15)	-848.1(9)	16.0(4)
C7	7420(2)	7175.2(15)	-745.7(9)	17.8(4)

C10	8382(2)	7235.7(17)	2058.5(10)	22.1(5)
C11	7636(2)	8940.7(16)	2098.9(9)	20.9(5)
C12	4051(2)	7707.3(14)	-582.8(8)	11.7(4)
C17	3097(2)	8463.3(14)	-805.5(9)	12.8(4)
C16	1849(2)	8285.2(15)	-1235.9(9)	15.8(4)
C15	1490(2)	7370.9(16)	-1428.4(9)	18.6(4)
C14	2347(2)	6623.3(15)	-1173.2(9)	19.2(4)
C13	3616(2)	6768.2(14)	-748.5(9)	15.4(4)
C18	3325(2)	9461.7(14)	-569.9(10)	16.6(4)
C19	4425(3)	5911.8(15)	-460.3(10)	22.8(5)
C20	4872(2)	7563.6(14)	1874.4(8)	12.5(4)
C25	4688(2)	6606.3(15)	2040.1(9)	16.3(4)
C24	3638(3)	6388.0(16)	2445.6(9)	20.7(5)
C23	2730(2)	7075.5(17)	2670.0(9)	20.8(5)
C22	2846(2)	8004.7(16)	2481.3(9)	18.0(4)
C21	3896(2)	8261.1(15)	2081.2(8)	14.0(4)
C26	5521(3)	5803.0(16)	1770.5(11)	24.3(5)
C27	3897(2)	9271.1(15)	1863.4(10)	19.1(4)

C11S	1213.2(8)	4863.9(4)	1500.7(3)	38.04(17)
C12S	-231.0(13)	6042.6(6)	551.2(4)	75.0(3)
C1S	1318(4)	5929(2)	1112.5(17)	55.9(9)

Table 3.14: Anisotropic Displacement Parameters ($\text{\AA}^2 \times 10^3$) for complex **3a**. The Anisotropic displacement factor exponent takes the form: $-2\pi^2[h^2a^{*2}U_{11}+2hka^*b^*U_{12}+]$.

Atom	U11	U22	U33	U23	U13	U12
Co1	9.18(12)	12.60(13)	7.95(13)	0.73(10)	0.20(9)	-0.64(10)
O1	13.1(7)	35.9(9)	9.6(7)	2.4(6)	-1.0(6)	-5.4(6)
N2	11.4(8)	13.7(8)	8.1(8)	0.3(6)	1.4(6)	-0.4(6)
N1	11.8(8)	10.9(7)	11.1(8)	-0.2(6)	1.7(6)	1.3(6)
N3	11.0(8)	16.1(8)	8.4(8)	1.4(7)	0.4(6)	-2.1(7)
C6	13.3(9)	15.7(10)	10.2(9)	0.7(7)	3.5(7)	0.2(7)
C5	14.7(9)	10.5(9)	12.6(9)	-0.5(7)	2.8(8)	1.6(7)
C4	14.5(10)	20.2(10)	16.5(10)	0.6(8)	5.8(8)	-0.1(8)
C3	10.7(9)	21.1(10)	23.8(11)	0.4(9)	2.9(8)	-3.6(8)
C2	12.9(10)	21.2(11)	17.5(11)	-0.3(8)	-2.6(8)	-1.8(8)
C1	13.3(9)	12.8(9)	13.1(10)	0.1(8)	-0.5(7)	1.3(7)
C9	10.5(9)	19.6(10)	10.7(9)	1.1(8)	-1.5(7)	-2.6(7)
C8	17.5(10)	18.3(10)	12.6(10)	2.4(8)	2.9(8)	-0.9(8)
C7	19.8(10)	19.3(10)	14.8(10)	-3.4(8)	4.3(8)	1.3(9)
C10	15.7(10)	30.4(12)	19.2(11)	9.3(10)	-2.2(8)	-1.2(9)

C11	17.4(10)	30.5(12)	14.6(10)	-6.6(9)	1.3(8)	-5.9(9)
C12	12.8(9)	16(1)	6.4(8)	0.4(7)	2.1(7)	-1.1(8)
C17	13.8(9)	15.2(9)	9.7(9)	0.2(8)	3.2(7)	0.1(8)
C16	14.5(10)	20.8(10)	11.9(9)	3.8(8)	-0.2(8)	2.9(8)
C15	14.9(10)	29.7(12)	10.4(9)	-2.8(8)	-2.0(8)	-2.5(8)
C14	22.7(11)	16.4(10)	18.0(11)	-5.3(8)	0.1(9)	-5.2(8)
C13	19.2(10)	14.7(10)	12.2(10)	0.3(8)	1.5(8)	-0.2(8)
C18	15.9(10)	12.8(9)	21.0(11)	-1.1(8)	1.8(8)	2.1(8)
C19	28.8(12)	13(1)	25.4(12)	0.9(9)	-2.6(9)	-0.6(9)
C20	11.4(9)	18(1)	7.6(9)	1.0(7)	-2.0(7)	-2.6(7)
C25	18.5(10)	19.1(10)	10.3(9)	2.4(8)	-2.9(8)	-4.3(8)
C24	24.5(11)	23.3(11)	13.1(10)	5.5(8)	-3.2(8)	-10.3(9)
C23	17.5(10)	35.0(13)	9.7(9)	3.5(9)	0.6(8)	-10.0(9)
C22	12.6(10)	30.8(12)	10.2(9)	-1.5(8)	-0.9(8)	-0.6(8)
C21	13.6(9)	19.4(10)	8.4(9)	-0.4(8)	-1.1(7)	-1.6(8)
C26	29.7(12)	16.6(11)	26.4(12)	2.3(9)	2.4(10)	-1.5(9)
C27	18.7(11)	19.3(10)	20.0(11)	0.7(9)	4.7(8)	4.1(8)
C11S	45.0(4)	25.8(3)	40.2(4)	8.8(3)	-10.0(3)	-11.5(3)

C12S	117.0(8)	33.9(4)	60.4(6)	-4.3(4)	-53.5(5)	18.9(5)
C1S	38.7(17)	51.7(19)	74(2)	38.3(18)	-8.4(16)	-3.0(14)

Table 3.15: Bond Lengths for complex**3a**.

Atom	Atom	Length/Å	Atom	Atom	Length/Å
Co1	O1	1.7945(15)	C9	C11	1.542(3)
Co1	N2	1.8363(16)	C12	C17	1.409(3)
Co1	N1	1.8573(16)	C12	C13	1.416(3)
Co1	N3	1.8392(16)	C17	C16	1.398(3)
N2	C6	1.495(2)	C17	C18	1.511(3)
N2	C12	1.429(2)	C16	C15	1.385(3)
N1	C5	1.348(2)	C15	C14	1.380(3)
N1	C1	1.345(2)	C14	C13	1.396(3)
N3	C9	1.488(2)	C13	C19	1.509(3)
N3	C20	1.424(2)	C20	C25	1.414(3)
C6	C5	1.513(3)	C20	C21	1.409(3)
C6	C8	1.535(3)	C25	C24	1.394(3)
C6	C7	1.539(3)	C25	C26	1.506(3)
C5	C4	1.383(3)	C24	C23	1.379(3)
C4	C3	1.390(3)	C23	C22	1.385(3)

C3	C2	1.388(3)	C22	C21	1.397(3)
C2	C1	1.384(3)	C21	C27	1.507(3)
C1	C9	1.512(3)	C11S	C1S	1.746(3)
C9	C10	1.540(3)	C12S	C1S	1.753(3)

Table 3.16: Bond Angles for complex4.

Atom	Atom	Atom	Angle/ °	Atom	Atom	Atom	Angle/ °
O1	Co1	N2	98.01(7)	N3	C9	C10	112.88(16)
O1	Co1	N1	177.17(7)	N3	C9	C11	112.51(16)
O1	Co1	N3	94.23(7)	C1	C9	C10	108.73(17)
N2	Co1	N1	84.16(7)	C1	C9	C11	109.01(16)
N2	Co1	N3	167.71(7)	C10	C9	C11	108.04(17)
N3	Co1	N1	83.64(7)	C17	C12	N2	120.33(17)
C6	N2	Co1	117.34(12)	C17	C12	C13	118.93(17)
C12	N2	Co1	125.75(12)	C13	C12	N2	120.62(17)
C12	N2	C6	116.59(15)	C12	C17	C18	122.01(17)
C5	N1	Co1	118.41(13)	C16	C17	C12	119.58(18)
C1	N1	Co1	118.67(13)	C16	C17	C18	118.33(18)
C1	N1	C5	122.91(17)	C15	C16	C17	121.10(19)
C9	N3	Co1	118.19(12)	C14	C15	C16	119.16(19)
C20	N3	Co1	123.81(12)	C15	C14	C13	121.68(19)
C20	N3	C9	117.95(15)	C12	C13	C19	122.42(18)

N2	C6	C5	105.80(15)	C14	C13	C12	119.12(18)
N2	C6	C8	112.51(16)	C14	C13	C19	118.39(18)
N2	C6	C7	112.11(16)	C25	C20	N3	120.31(18)
C5	C6	C8	109.16(16)	C21	C20	N3	120.12(17)
C5	C6	C7	108.29(16)	C21	C20	C25	119.33(18)
C8	C6	C7	108.82(16)	C20	C25	C26	122.57(18)
N1	C5	C6	113.68(17)	C24	C25	C20	119.0(2)
N1	C5	C4	119.59(18)	C24	C25	C26	118.36(19)
C4	C5	C6	126.72(18)	C23	C24	C25	121.7(2)
C5	C4	C3	118.65(19)	C24	C23	C22	119.29(19)
C2	C3	C4	120.54(19)	C23	C22	C21	121.2(2)
C1	C2	C3	118.90(19)	C20	C21	C27	122.00(18)
N1	C1	C2	119.41(18)	C22	C21	C20	119.32(19)
N1	C1	C9	113.91(17)	C22	C21	C27	118.63(19)
C2	C1	C9	126.68(18)	C11S	C1S	C12S	111.42(18)
N3	C9	C1	105.55(15)				

DFT calculations

Table 3.17: Energy and composition of frontier molecular orbitals in terms of Co^{3+} , $[\text{NNN}]^{2-}$, and second donor fragments. Matching singly occupied α -, β -orbitals of complexes **2**, **3a** and **4** and resemblance factor q .^a

	MO		Energy (kcal/mol)		Co3+		[NNN]2-		Second donor		q
	α -	β -			α -	β -	α -	β -	α -	β -	
2	LUMO		68.5		52.5		47.5		0.1		
	HOMO		0		1.8		97.4		0.9		
	HOMO-1		-1.1		0		98.2		1.8		
	HOMO-2		-2		0		99.8		0.2		
	HOMO-3		-4.6		14.3		84.7		1		
	HOMO-4		-6.1		5.5		93.9		0.5		
3a	LSUMO+2	LSUMO	65	48.8	1.6	53.8	98.3	0.1	42.5	3.7	0.56
	HSOMO-1	HSOMO	-1.3	0	2.5	4.8	1.5	96	1.8	93.5	1
		HSOMO-2		-17.7		7.2			92.4	0.4	na
	HSOMO-3	LSUMO+1	-18.3	58.4	10.2	54.6	89.7	0.1	45.4	0	0.81
	HSOMO-5	HSOMO-4	-26	-24.9	3.5	3.5	94.2	2.3	94.7	1.8	0.91
	HSOMO-6	HSOMO-7	-27.9	-27.9	0	0	28.1	71.9	28.6	71.4	1
	HSOMO-9	HSOMO-8	-30.3	-30.3	0.1	0.1	99.6	0.4	99.6	0.3	0.99
	HSOMO-11	HSOMO-10	-30.8	-30.7	0.2	0.3	74	25.8	75.8	27	0.99
	HSOMO-15		-43.9		42.3		57.4		0.2	na	
4	LSUMO+1	LSUMO	80.8	68.5	1.5	34.8	98.4	57.9	0.1	7.3	0.67
	HSOMO	LSUMO+2	0	83.3	12.2	60.3	87.8	39.7	0	0	0.82
	HSOMO-3	HSOMO-2	-10.5	-10.1	3	4.9	96.8	95	0.2	0.1	0.99
	HSOMO-4	HSOMO-5	-13.7	-14	0.8	0	96.3	99.9	2.9	0.1	0.91
	HSOMO-6	HSOMO-1	-14.9	-1.8	3.9	8.1	86.9	91.4	9.3	0.5	0.79
	HSOMO-8	HSOMO-7	-22.1	-20.6	6.5	16.1	87.3	76.9	6.2	7.1	0.97
	HSOMO-10	HSOMO-9	-22.3	-22.2	0.1	0.1	99.8	99.6	0.1	0.3	1
	HSOMO-38	HSOMO-11	-91.9	-23.7	42.9	35.4	57.1	64.6	0	0	0.58

^aIn spin-unrestricted calculations as performed herein, the α - and β -spin molecular orbitals are not necessarily orthogonal. AOMix introduces the resemblance factor q to quantify the matching degree of the corresponding α - and β -spin orbital pairs, using the overlap integrals between the α - and β -spin molecular orbitals $\langle \phi_i^\alpha | \phi_j^\beta \rangle$ (sometimes referred to as the "mutual overlap matrix"). See <http://www.sg-chem.net/aomix/AOMix-manual.pdf> for further details.

Table 3.18: Optimized coordination for complex **2**.

Co	-0.00006	0.42176	-0.00013
N	-1.80173	0.57657	-0.00008
N	-0.0001	2.28392	-0.00007
N	1.80162	0.57661	-0.00003
C	-1.19327	2.92432	-0.00014
C	-1.2214	4.32644	-0.00016
H	-2.16504	4.86076	-0.0002
C	-0.00015	5.02745	-0.0001
H	-0.00018	6.11354	-0.0001
C	1.22111	4.3265	-0.00003
H	2.16475	4.86084	0.00001
C	1.19304	2.92437	-0.00002
C	-2.39057	1.98835	-0.00017
C	-3.25883	2.26549	1.26175
H	-4.11072	1.58034	1.2961
H	-3.65259	3.28758	1.21928

H	-2.67548	2.16043	2.18047
C	-3.2587	2.26539	-1.26217
H	-2.67536	2.16007	-2.18087
H	-3.65231	3.28755	-1.21991
H	-4.11072	1.58039	-1.29643
C	2.3904	1.98847	0.00007
C	3.25869	2.26568	-1.26179
H	4.11075	1.58074	-1.29598
H	3.6522	3.28787	-1.21938
H	2.67546	2.1604	-2.18056
C	3.25843	2.26561	1.26213
H	2.67504	2.16021	2.18078
H	3.65189	3.28783	1.21989
H	4.11053	1.58072	1.29643
C	-2.77521	-0.50584	0.00012
C	-3.23254	-1.05586	1.23563
C	-4.19408	-2.08779	1.21015
H	-4.54617	-2.49908	2.15408

C	-4.69227	-2.59315	0.00051
H	-5.43902	-3.38249	0.00065
C	-4.19436	-2.08796	-1.20932
H	-4.54668	-2.49941	-2.15311
C	-3.23282	-1.05605	-1.23518
C	-2.71553	-0.61219	2.59625
H	-1.79668	-0.02492	2.52075
H	-2.51949	-1.48762	3.22805
H	-3.45572	0.00018	3.12719
C	-2.71604	-0.61267	-2.59599
H	-3.45637	-0.00053	-3.12701
H	-2.51994	-1.48824	-3.22756
H	-1.79726	-0.02528	-2.52075
C	2.77523	-0.50569	0.00011
C	3.23296	-1.05574	-1.23523
C	4.19465	-2.08751	-1.20942
H	4.54707	-2.49882	-2.15322
C	4.6926	-2.59272	0.00039

H	5.43951	-3.38192	0.0005
C	4.19428	-2.08753	1.21005
H	4.5464	-2.49886	2.15395
C	3.23258	-1.05576	1.23558
C	2.71622	-0.61229	-2.59603
H	1.79747	-0.02483	-2.52078
H	2.52007	-1.48783	-3.22761
H	3.45659	-0.00019	-3.12704
C	2.71539	-0.61236	2.59623
H	3.45572	-0.00055	3.12762
H	2.51876	-1.48795	3.22762
H	1.79683	-0.02466	2.5207
N	-0.00004	-1.54952	-0.00032
C	0.00007	-2.24178	-1.17062
H	0.00004	-1.65506	-2.07974
C	0.00023	-3.64173	-1.21018
H	0.00029	-4.15093	-2.16816
C	0.00029	-4.35938	-0.00054

H 0.0004 -5.44537 -0.00063

C 0.00016 -3.64193 1.20923

H 0.00022 -4.15127 2.16713

C -0.00002 -2.24197 1.16988

H -0.00018 -1.65538 2.07909

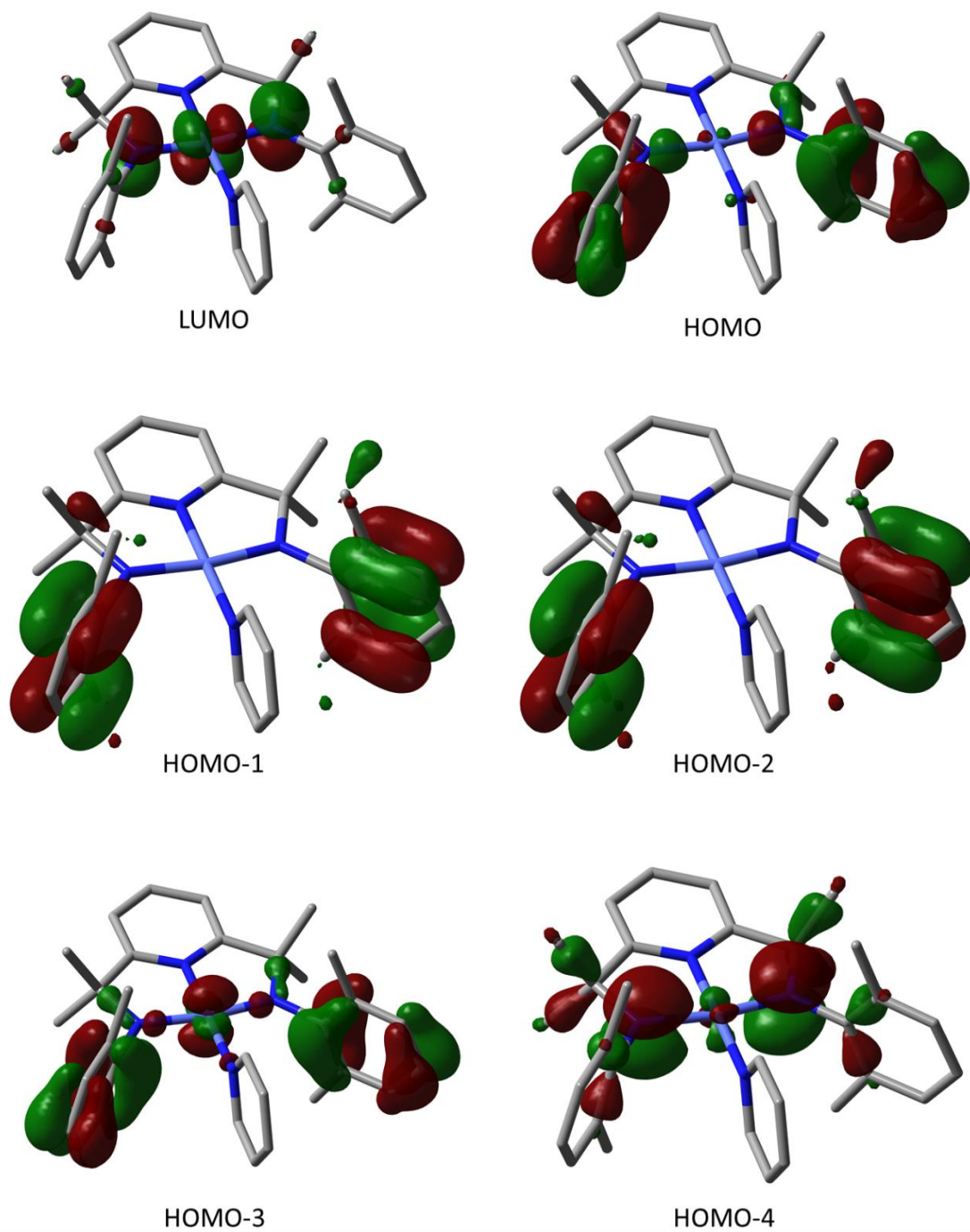


Figure 3.19: Selected MOs of complex 2.

Table 3.19: Optimized coordinates of complex **3a**.

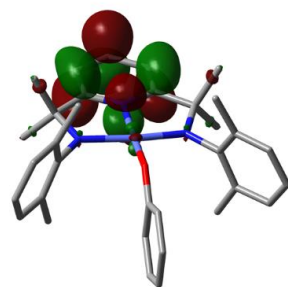
Co	0.00009	0.5717	0.1327
N	1.84935	0.75407	0.04146
N	0.00032	2.43859	-0.13372
N	-1.84913	0.75454	0.0415
C	1.19783	3.06904	-0.24655
C	1.22187	4.45306	-0.47666
H	2.16657	4.97724	-0.56846
C	0.00066	5.14477	-0.58855
H	0.00079	6.21674	-0.7669
C	-1.22073	4.45337	-0.47659
H	-2.1653	4.97779	-0.56834
C	-1.19703	3.06935	-0.24649
C	2.40481	2.15407	-0.09222
C	3.34092	2.32842	-1.32544
H	4.19179	1.64638	-1.23968
H	3.73143	3.35303	-1.36981

H	2.81196	2.11644	-2.25854
C	3.19852	2.60289	1.1768
H	2.54546	2.65135	2.05353
H	3.64332	3.59407	1.0214
H	4.00677	1.8917	1.37463
C	-2.40423	2.15469	-0.09207
C	-3.19766	2.60367	1.17708
H	-4.00612	1.89272	1.37494
H	-3.64217	3.595	1.0218
H	-2.54449	2.65185	2.05374
C	-3.34044	2.32935	-1.32516
H	-2.81167	2.11723	-2.25833
H	-3.73064	3.35408	-1.36946
H	-4.19151	1.64757	-1.23931
C	2.79631	-0.32583	0.21043
C	3.36698	-0.97348	-0.92419
C	4.32914	-1.98953	-0.73055
H	4.7569	-2.47944	-1.60377

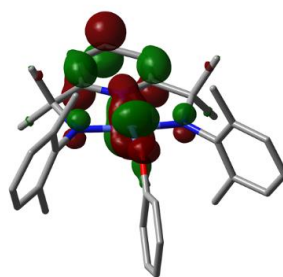
C	4.71022	-2.39553	0.55427
H	5.4522	-3.17943	0.68763
C	4.08243	-1.81533	1.66997
H	4.32437	-2.16949	2.67014
C	3.1162	-0.80114	1.52146
C	2.93822	-0.67612	-2.3524
H	2.02738	-0.07358	-2.37953
H	2.73865	-1.61788	-2.8778
H	3.71897	-0.1448	-2.91464
C	2.37734	-0.32052	2.75765
H	2.49456	0.75102	2.94435
H	2.73308	-0.85615	3.64578
H	1.30617	-0.52295	2.6424
C	-2.79636	-0.32513	0.21044
C	-3.11632	-0.80046	1.52145
C	-4.08279	-1.81444	1.66993
H	-4.32476	-2.16861	2.67008
C	-4.71075	-2.39442	0.55421

H	-5.4529	-3.17816	0.68755
C	-4.32962	-1.98842	-0.73059
H	-4.75753	-2.47817	-1.60383
C	-3.36723	-0.97258	-0.9242
C	-2.37733	-0.32007	2.75766
H	-1.30619	-0.52251	2.6423
H	-2.73302	-0.85585	3.64572
H	-2.49453	0.75143	2.94456
C	-2.93846	-0.67521	-2.35241
H	-3.71909	-0.1436	-2.91455
H	-2.73922	-1.61699	-2.87791
H	-2.02745	-0.07294	-2.37955
O	-0.00009	-1.21562	0.58832
C	-0.00034	-2.41912	-0.04249
C	-0.00043	-2.54265	-1.45537
C	-0.00049	-3.60301	0.74229
C	-0.00067	-3.81119	-2.06084
H	-0.00032	-1.63979	-2.0612

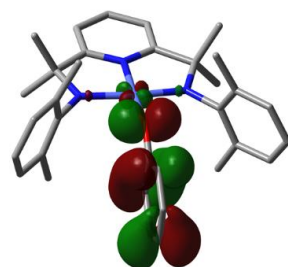
C	-0.00072	-4.86402	0.12636
H	-0.00041	-3.50581	1.82489
C	-0.00082	-4.98375	-1.27986
H	-0.00074	-3.88286	-3.14773
H	-0.00083	-5.75891	0.74676
H	-0.001	-5.96351	-1.75141



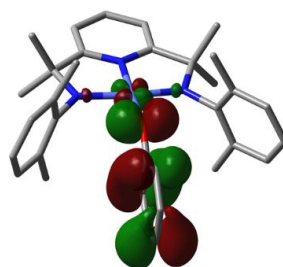
LSUMO+2



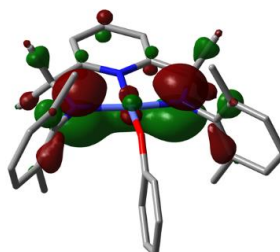
LSUMO



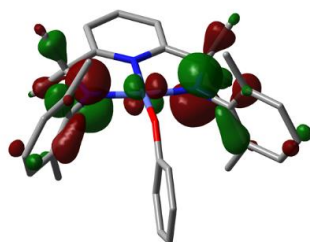
HSOMO-1



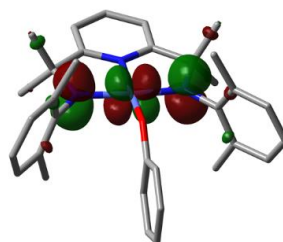
HSOMO



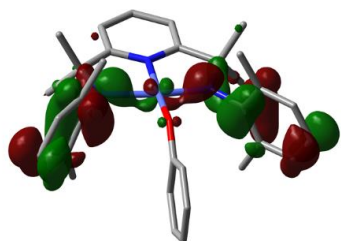
HSOMO-2



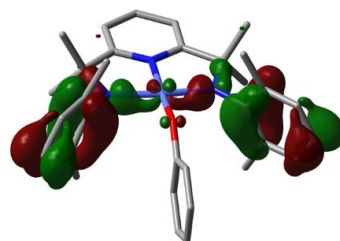
HSOMO-3



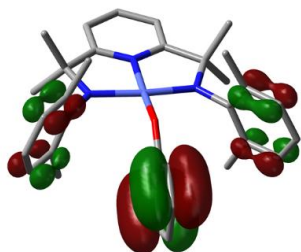
LSUMO+1



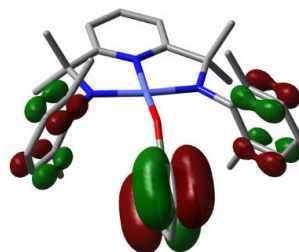
HSOMO-5



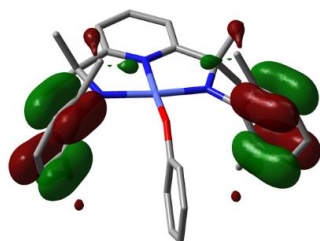
HSOMO-4



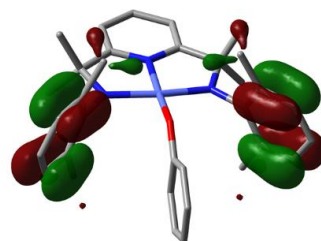
HSOMO-6



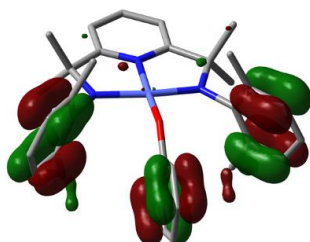
HSOMO-7



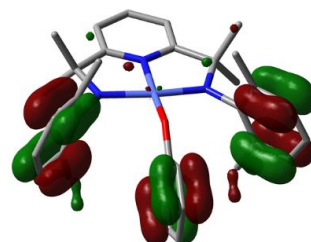
HSOMO-9



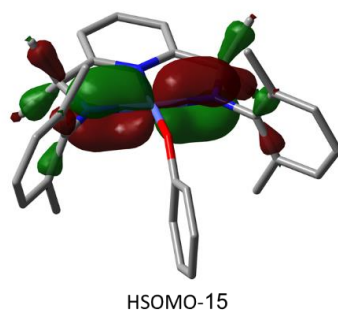
HSOMO-8



HSOMO-11



HSOMO-10



HOMO-15

Figure 3.20: Selected MOs of complex **3a**.

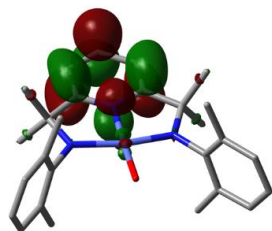
Table 3.20: Optimized coordinates of complex 4.

Co	0.00479	-0.02249	-0.00006
N	-1.84474	0.17172	0.00003
N	0.01015	1.8658	-0.00006
N	1.84944	0.16462	-0.00006
C	-1.18734	2.50461	-0.00004
C	-1.20892	3.90805	-0.00006
H	-2.15153	4.44462	-0.00005
C	0.01549	4.60493	-0.00009
H	0.01744	5.69177	-0.0001
C	1.23696	3.90342	-0.0001
H	2.18192	4.43574	-0.00012
C	1.21007	2.49997	-0.00008
C	-2.39692	1.57372	0
C	-3.26023	1.87778	1.26319
H	-4.11183	1.19052	1.30201
H	-3.65212	2.90252	1.22902

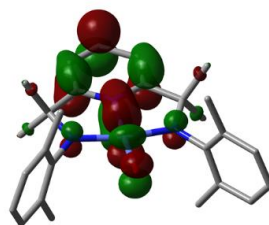
H	-2.67031	1.75909	2.17688
C	-3.26025	1.87771	-1.26319
H	-2.67035	1.75899	-2.17689
H	-3.65217	2.90244	-1.22906
H	-4.11184	1.19044	-1.30197
C	2.41212	1.56088	-0.00009
C	3.27751	1.85779	-1.26385
H	4.12186	1.16205	-1.30185
H	3.67768	2.87941	-1.22948
H	2.68658	1.74269	-2.17739
C	3.27755	1.85784	1.26363
H	2.68666	1.74275	2.1772
H	3.6777	2.87947	1.22922
H	4.12192	1.16211	1.30163
C	-2.77764	-0.92623	0.00011
C	-3.21259	-1.50969	1.23355
C	-4.14499	-2.56903	1.21073
H	-4.47064	-3.00286	2.15475

C	-4.63423	-3.08381	0.00029
H	-5.35332	-3.89973	0.00036
C	-4.14516	-2.56908	-1.21024
H	-4.47096	-3.00294	-2.1542
C	-3.21277	-1.50973	-1.23323
C	-2.65985	-1.07039	2.57968
H	-1.70586	-0.55088	2.46212
H	-2.50356	-1.94343	3.22522
H	-3.35047	-0.39607	3.10472
C	-2.66024	-1.07048	-2.57946
H	-3.35097	-0.39624	-3.10446
H	-2.50396	-1.94355	-3.22497
H	-1.70627	-0.55089	-2.46206
C	2.77411	-0.94071	-0.00004
C	3.20143	-1.52347	-1.23097
C	4.13886	-2.57728	-1.2101
H	4.46135	-3.01365	-2.15436
C	4.63242	-3.08868	-0.00001

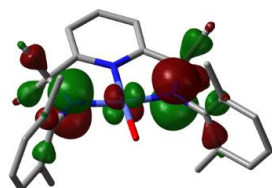
H	5.35549	-3.90152	0
C	4.13885	-2.57725	1.21007
H	4.46133	-3.01361	2.15435
C	3.20142	-1.52345	1.23091
C	2.62849	-1.09788	-2.57258
H	1.65071	-0.62665	-2.44421
H	2.50683	-1.97477	-3.22033
H	3.28331	-0.39001	-3.10032
C	2.62846	-1.09786	2.57251
H	3.28338	-0.39017	3.10037
H	2.50657	-1.97478	3.22017
H	1.65078	-0.62642	2.44412
H	-0.80297	-2.25943	-0.00017
O	0.07485	-1.81811	-0.00017



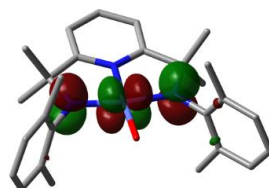
LSUMO+1



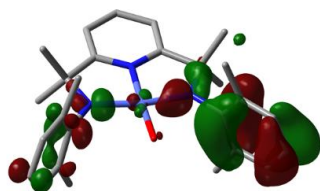
LSUMO



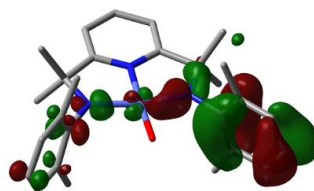
HSOMO



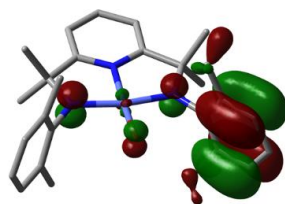
LSUMO+2



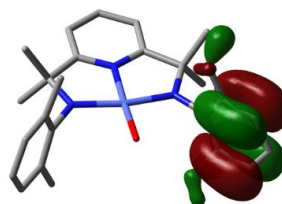
HSOMO-3



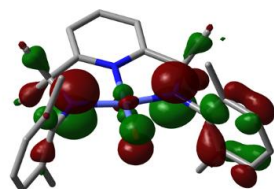
HSOMO-2



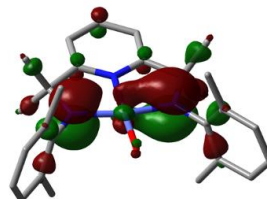
HSOMO-4



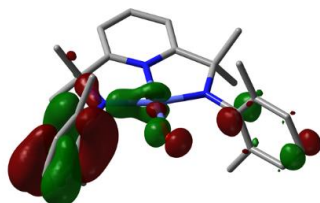
HSOMO-5



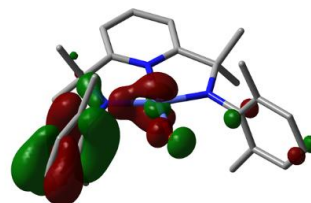
HSOMO-6



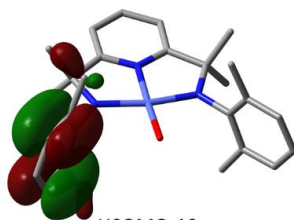
HSOMO-1



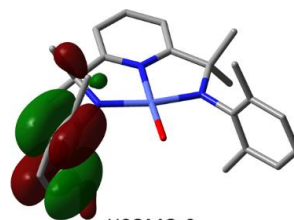
HSOMO-8



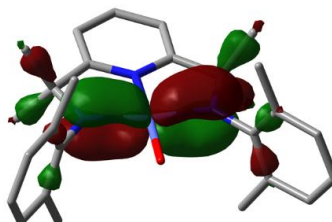
HSOMO-7



HSOMO-10



HSOMO-9



HSOMO-11

Figure 3.21: Selected MOs of complex 4.